Davies, P. J., McKenzie, J. A., Palmer-Julson, A., et al., 1991
Proceedings of the Ocean Drilling Program, Initial Reports, Vol. 133

15. SITE 822[1]

Shipboard Scientific Party[2]

HOLE 822A

Date occupied: 17 September 1990

Date departed: 20 September 1990

Time on hole: 3 days, 8 hr, 21 min

Position: 16°25.379'S, 146°12.904'E

Bottom felt (rig floor; m, drill-pipe measurement): 966.6

Distance between rig floor and sea level (m): 11.41

Water depth (drill-pipe measurement from sea level, m): 955.2

Total depth (rig floor; m): 1400.5

Penetration (m): 433.9

Number of cores (including cores with no recovery): 47

Total length of cored section (m): 433.9

Total core recovered (m): 387.5

Core recovery (%): 89.3

Oldest sediment recovered:
Depth (mbsf): 433.9
Nature: lithified nannofossil mixed sediment
Age: late Pliocene

Principal results: Site 822 occurs in 955.12 m of water, on the foot of slope east of the Great Barrier Reef offshore of Cairns. The location is northeast of the transect across the upper slope in Grafton Passage. Drilling was aimed at determining the age and facies of a lower-slope fan in front of the present-day Great Barrier Reef. An additional objective was to define lower-slope fan processes and to understand the sea-level signatures preserved in the lower-slope facies. Hole 822A was APC-drilled to 95.9 mbsf, continued with the XCB to 433.9 mbsf, and had an excellent recovery rate of 98.3%. Site 822 is composed of a Holocene to upper Pliocene (>2.6 Ma) section of hemipelagic sediments having a hiatus between 275,000 and 465,000 yr. Benthic foraminifers indicate that the sediments were wholly deposited within middle bathyal depths. Sedimentation rates are highly variable, with extremely high rates ranging from 36 to 42 cm/k.y., which occurred between 0.93 Ma and 1.48 Ma. Relatively high rates of 16 cm/k.y. occurred between 1.88 and 2.6 Ma. The lowest rates of 4.0 cm/k.y. were found at the base of the section, whereas relatively low rates of 8 to 12 cm/k.y. occurred before 930,000 yr. High sedimentation rates may have been coincident with periods of high global sea level.

Sediments recovered at Site 822 are mainly muds that contain varying amounts of carbonate ooze and terrigenous clays, with lesser bioclastic and terrigenous (mostly quartz) sand and silt. However, the sequence is distinctly cyclical, as seen in color and compositional variations that are related to the proportions of carbonate and terrigenous sediments. Two principal lithologic units were identified. Unit I is dominated by clayey calcareous muds; Unit II is similar to Unit I, except that it is darker in color and contains more terrigenous sediment; the unit also contains abundant quartz silt and sand.

Unit I: depth, 0–52.9 mbsf; age, 0–<0.93 Ma, Pleistocene. The unit is composed of bioclastic ooze with nannofossils and micrite. Deformation of soft sediments characterizes Subunits IA and IB, although a hiatus of 190,000 yr separates them.

Subunit IA: depth, 0–27.4 mbsf; age, <0.275 Ma, late Pleistocene. The subunit is composed of clayey bioclastic calcareous and bioturbated ooze/mud with nannofossils, micrite, and scattered pteropods, and is finely laminated in the lower part of the section. Intervals of clayey calcareous mixed sediments (mud) that contain terrigenous clay and silt also occur, as do lenses of bioclastic packstones. Carbonate contents range from 53.3% to 70.0%.

Subunit IB: depth, 27.4–52.9 mbsf; age, 0.465-0.93 Ma, Pleistocene. The subunit is composed of greenish-white to greenish-gray, bioturbated clayey nannofossil ooze with bioclasts. Carbonate contents of 59.5% to 79.3% were the highest recorded for Site 822. Rare interbeds of fine- to medium-grained bioclastic packstones, scattered shell fragments, and burrow infills occur throughout the subunit. The subunit gradationally overlies Subunit IIA.

Unit II: depth, 52.9–433.9 mbsf; age, 0.465–>2.6 Ma, Pliocene to Pleistocene. The unit is a dark greenish-gray clayey calcareous mixed sediment that contains terrigenous clay interbedded with clayey nannofossil ooze. Claystones dominate the middle part of the unit, whereas bioclastic sediments become more important downward.

Subunit IIA: depth, 52.9–202.5 mbsf; age, 0.465–< 1.27 Ma, Pleistocene. While gradationally underlying Subunit IB, this subunit is more clay-rich and darker colored and consists of silty calcareous mixed sediment that is interbedded with clayey nannofossil ooze in the upper part. Quartz silt and very fine sand occur in the middle part of the subunit and increase downward to 32%. Intervals of silty, calcareous claystone become more common downward, particularly below 150 mbsf. Dolomite was identified in Core 133-822A-14X (125 mbsf). Fine to very fine bioclasts occur in burrows and, less commonly, as thin beds of graded bioclastic to foraminiferal packstones. High sedimentation rates characterize the subunit, suggesting that the downward increase in siliciclastics results from greater terrigenous influx.

The physical properties of Subunits IA and IB and the upper half of Subunit IIA are consistent with normal compaction trends; porosity values vary from 60% to 50%, with water content from 54% to 35%.

Subunit IIB: depth, 202.5–332.5 mbsf; age, late Pliocene to Pleistocene. Dark greenish-gray, well-compacted and partially lithified calcareous claystones (carbonate contents <50%) are interrupted between 260 and 308 mbsf by intervals of lighter greenish-gray, more calcareous (carbonate contents 40%–61%) chalky clayey mudstone. Bioclastic and quartzose turbidites occur in Core 133-822A-31X.

Subunit IIC: depth, 332.5–433.9 mbsf; age, late Pliocene. The subunit is composed of well-compacted and semilithified alternating nannofossil mixed sediments and dark greenish-gray calcareous claystone. Bioclasts are common in the mixed sediments. Quartz and fine sand increase downward and reach as high as 17% in the lower part of the hole. Intervals of foraminiferal bioclastic packstone represent turbidites.

Whereas physical property values of the lower half of Subunits IIA, IIB, and IIC remain relatively constant with depth, both porosity and water content values exhibit large variations that generally correlate with alternating intervals of claystone and chalk.

[1] Davies, P. J., McKenzie, J. A., Palmer-Julson, A., et al., 1991. *Proc. ODP, Init. Repts.*, 133: College Station, TX (Ocean Drilling Program).

[2] Shipboard Scientific Party is as given in list of participants preceding the contents.

X-ray diffraction studies at Site 822 indicate that sediments are composed of calcite (9.5%–61.3%), aragonite (18.7%–83.1%), clay, and detrital quartz; these proportions remain relatively constant, except for high concentrations of quartz between 75 and 175 mbsf. High-Mg calcite (up to 30%) occurs in the top 300 mbsf, whereas dolomite (up to 18.2%) only occurs in the top 157.2 mbsf. Clay increases downward and alternates with carbonate to form distinct cycles.

Throughout Site 822, high-frequency cyclical variations in sediment character record changes in fluxes of terrigenous and carbonate sediments, possibly related to changes in glacioeustatic sea levels and/or climate changes.

Interstitial-water sampling has shown that Ca^{2+}, Mg^{2+}, and K^{2+} decreased in concentration with increasing sub-bottom depth. These decreases are thought to indicate the formation of authigenic calcite and dolomite and clay mineral diagenesis. Strontium values indicate an increase to a depth of 17.8 mbsf–the depth at which sulfate disappears–and thereafter decreases to the bottom of the hole. The small changes in Sr^{2+} at Site 822 suggest that the degree of carbonate recrystallization is low compared with that at other slope sites. WSTP samples were contaminated with seawater and did not reflect variations in interstitial water chemistry accurately.

Concentrations of organic carbon at Site 822 did not exceed 0.65% and were highest in the clay-rich sediments. The TOC/nitrogen ratio in the organic material is thought to indicate a marine origin. Concentrations of up to 77,000 ppm methane and 4 ppm ethane were recorded at 55 mbsf, but these values represented no safety or pollution problem.

Seismic-stratigraphic logs, geochemical logs, and the FMS were run at Site 822. As at almost all other sites off northeastern Australia, changes in velocity generally followed a compaction profile, which points to the importance of mechanical compaction for controlling porosity. Whereas the cores indicated that stratigraphy was controlled largely by variations in clay and carbonate contents, all elements of the geochemical logs (potassium, aluminum, silicon, and calcium) correlate positively, indicating that an artifact (e.g., hole size) may be overprinting the log response. Four log-based units were identified on the basis of resistivity and velocity responses. Zones of dolomitization were identified and upward-coarsening and upward-fining sequences were defined between 263 and 323 mbsf.

Paleomagnetic studies at Site 822 indicate that the cored section spans the Pleistocene and late Pliocene. The Brunhes/Matuyama boundary was placed at 165 mbsf, the Matuyama/Gauss boundary at 396 mbsf. Within the Matuyama reversed chron, we identified five polarity zones, but at this time, their correlation to subchrons within the Matuyama is uncertain. Discrepancies with paleontological data, particularly over the depth of the Brunhes/Matuyama boundary, are probably related to a moderate magnetic overprinting or to early remagnetization and should be addressed in post-cruise studies. Volume susceptibility at Site 822 shows several major peaks that correlate inversely with the percentage of carbonate, suggesting that the magnetic signals reflect terrigenous influxes.

BACKGROUND AND SCIENTIFIC OBJECTIVES

Site 822 lies in approximately 960 m of water on the lower slope of the Great Barrier Reef, about 26 km north-northwest of Grafton Passage and Sites 819 through 821. This site is one of the western holes in the Queensland Trough transect and is a mixed carbonate/siliciclastic site that complements the pure carbonate Site 824. Drilling in this hole sampled a lower-slope fan to provide facies data in a more distal position than those of the proximal upper-slope Sites 819 through 821. The pre-drilling prognosis for this site is shown in Figure 1.

Scientific objectives at this site were as follows:

1. To determine the age and facies of lower-slope sediments in front of today's Great Barrier Reef.
2. To determine the sea-level signatures preserved in the lower-slope facies by comparing those at this site with those from Sites 819 to 821.
3. To examine fan processes on the lower slope in a mixed siliciclastic/carbonate depositional system.

OPERATIONS

Transit to Site 822

A departing seismic survey was conducted over Sites 819, 820, and 821 and continued during the 14-nmi transit to Site 822 (proposed Site NEA-4). The survey covered a total of 31 nmi in 6.5 hr at an average speed of 4.8 kt. A Datasonics commandable recall beacon was dropped at 1324L (all times are given in local time, or L) 17 September, but the connection to its weights broke upon deployment. The beacon was retrieved and the weights securely reattached, and it was redeployed at 1344L.

Hole 822A

Hole 822A was located at 16°25.379′S, 146°12.904′E; the precision depth recorder (PDR) predicted a water depth of 952.3 m from sea level. We lowered the bit to a water depth of 946.6 m from sea level for the first shot. Hole 822A was spudded at 1647L, 17 September. From Core 133-822A-1H, we recovered 0.93 m of sediment, indicating that the mud line occurs at a water depth of 955.2 m from sea level. Continuous APC cores (Cores 133-822A-1H through -11H were taken from 0 to 95.5 mbsf, with 95.5 m cored and 101.5 m recovered (106.3% recovery; excessive recovery rates result from gas expansion of the sediment).

Cores 133-822A-12X through -43X were taken from 95.5 to 400.0 mbsf, with 304.5 m cored and 244.4 m recovered (80.3% recovery). Gas concentrations (determined by headspace analysis) averaged 50,000 ppm C_1, 3 ppm C_2, and no C_3. The C_1/C_2 ratio started a normal logarithmic decline (20,000–2,500) down to 260 mbsf, at which point concentrations of C_2 and C_3 began to increase. The Claypool graph of thermal maturity was in the normal range; this indicates that hydrocarbons were generated *in-situ*, had not migrated into the sediment from deeper in the section, and thus presented no safety problems. Temperature data from the Leg 133 Pollution Prevention and Safety Panel (PPSP) review and the WSTP data from Hole 822A indicate a 5.5°C/100 m gradient.

A short trip (up to 103.6 mbsf and back to the bottom of the hole) detected obstructions. A bridge was tagged at 373.4 mbsf, and the hole was washed and reamed to its bottom at 400.0 mbsf. We obtained approval from shore to continue coring for an additional 50 m after logging; our intention was to reach a seismic horizon we thought represented 2.4 Ma, which evidently lay deeper than the 400 mbsf penetration originally planned for this hole. The go-devil normally dropped to open the lockable flapper valve was not run, but rather a special go-devil was adapted to run on the bottom of the logging tools for use with each logging string. We pulled the bit up to 103.2 mbsf for logging, but encountered no drag. Logs were run as follows:

1. The induction/density/sonic/caliper/gamma-ray (DITE/HLDT/SDT/MCDG/ NGT) logging tool string was run into the hole at 2310L, 19 September; this string was able to reach to only 333.3 mbsf, 66.7 m off the bottom. The tool was back out of the hole at 0130L, 20 September.
2. The geochemical/aluminum clay/gamma-ray (GST/ACT/CNTG/NGT/TCC) logging tool string was placed in the hole at 0320L; this string reached to only 324.8 mbsf, 75.2 m off the bottom. The tool was brought out of the hole at 0715L.
3. The formation microscanner/gamma-ray/temperature (FMS/NGT/TCC) logging tool string was placed in the hole at

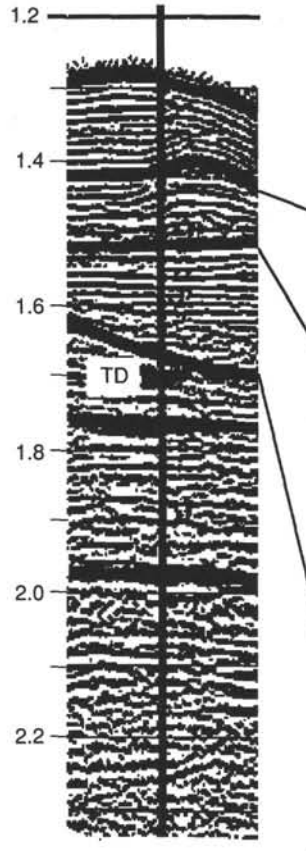

Depth (mbsf)	Age	Velocity (km/s)	Lithology	Paleoenvironment	Sed. rate (m/m.y.)	Comments
0	latest Pliocene to Quaternary	1.56	Carbonate mud draped over siliciclastic and carbonate sand to mud	Pelagic ooze over lower slope fan deposits	43	Both coarser channel deposits and fine-grained "levee" deposits should be represented.
100 H3	(113) Pliocene	1.56	Siliciclastic and carbonate sand to mud	Lower slope fan	35	
H5						
200	(183) Pliocene	1.86	Siliciclastic and carbonate sand to mud	Lower slope fan	35	
300 H8	(318) latest Miocene to Pliocene	1.86 / 2.23	Siliciclastic and carbonate sand to mud	Lower slope fan	30	
400	TD					
H10	(445)					
500						

Figure 1. Pre-drilling prognosis for Site 822.

0820L; the tool only reached 176.3 mbsf (223.7 m off the bottom). This string was back out of the hole at 0955L.

We ran the bit back to the bottom to continue coring another 50 m, or until the 2.4-Ma horizon was reached. Cores 133-822A-43X through -47X were taken from 400.0 to 433.9 mbsf, with 33.9 m cored and 38.6 m recovered (113.9% recovery).

Table 1 presents a coring summary for Site 822.

SITE GEOPHYSICS

JOIDES Resolution separated from the beacon at Hole 821B at 0355L (JD 259/1755UTC), 17 September 1990, and began the 6-hr-transit seismic line to Site 822 (proposed Site NEA-4) at 0318L (JD 250/1718UTC). We had decided to record a seismic tie-line that connected Sites 820 and 822; thus, a magnetometer and seismic equipment were deployed immediately after departure. Continuous bathymetric, magnetic, and seismic data were recorded during the Line 7 transit, heading about 325° along the upper-slope terrace just east of the Great Barrier Reef, in about 250 to 300 m of water. This transit line continued on to become the site-location survey for Site 822. The tie-line commenced at a position of 16°38.730′S and 146°19.160′E, about 1 nmi southeast of Site 820, at 0638L (JD 259/2038UTC), and the site-location survey component began at about 0937L (JD 259/2338UTC) at a position of 16°28.272′S and 146°09.118′E, about 4.6 nmi southwest of Site 822.

Site 822 lies in about 960 m of water on the lower slope adjacent to the Great Barrier Reef, on the western margin of Queensland Trough, about 72 km northeast of the town of Cairns (Fig. 2). It is about 14 km east of the nearest reef (Onyx Reef) and about 26 km north-northwest of Sites 819 through 821, and 64 km west-northwest of Site 823. The site forms part of a transect of Leg 133 drilling sites that extends east from the Great Barrier Reef across Queensland Trough to western Queensland Plateau, in the vicinity of Holmes Reef. The site was selected with the aim of defining and evaluating the relationship between the

Table 1. Coring summary for Site 822.

Core no.	Date (Sept. 1990)	Time (UTC)	Depth (mbsf)	Length cored (m)	Length recovered (m)	Recovery (%)
1H	17	0655	0–0.9	0.9	0.93	100.0
2H	17	0715	0.9–10.4	9.5	9.68	102.0
3H	17	0735	10.4–19.9	9.5	9.90	104.0
4H	17	0755	19.9–29.4	9.5	9.80	103.0
5H	17	0825	29.4–38.9	9.5	9.89	104.0
6H	17	0855	38.9–48.4	9.5	9.00	94.7
7H	17	0920	48.4–57.9	9.5	10.13	106.6
8H	17	0945	57.9–67.4	9.5	10.19	107.2
9H	17	1010	67.4–76.9	9.5	10.74	113.0
10H	17	1030	76.9–86.4	9.5	11.16	117.5
11H	17	1105	86.4–95.9	9.5	10.09	106.2
12X	17	1305	95.9–105.7	9.8	8.31	84.8
13X	17	1350	105.7–115.4	9.7	7.07	72.9
14X	17	1435	115.4–125.0	9.6	7.57	78.8
15X	17	1520	125.0–134.6	9.6	7.19	74.9
16X	17	1605	134.6–144.3	9.7	5.32	54.8
17X	17	1655	144.3–154.0	9.7	9.83	101.0
18X	17	1910	154.0–163.7	9.7	6.13	63.2
19X	17	2010	163.7–173.3	9.6	6.31	65.7
20X	17	2105	173.3–182.6	9.3	9.58	103.0
21X	17	2155	182.6–192.2	9.6	9.12	95.0
22X	17	2305	192.2–201.5	9.3	5.09	54.7
23X	18	0105	201.5–211.2	9.7	5.03	51.8
24X	18	0200	211.2–220.9	9.7	7.60	78.3
25X	18	0315	220.9–230.5	9.6	8.12	84.6
26X	18	0435	230.5–240.2	9.7	5.28	54.4
27X	18	0600	240.2–249.8	9.6	8.93	93.0
28X	18	0825	249.8–259.5	9.7	6.30	64.9
29X	18	0930	259.5–269.1	9.6	8.69	90.5
30X	18	1100	269.1–278.8	9.7	10.02	103.3
31X	18	1240	278.8–288.4	9.6	10.47	109.0
32X	18	1355	288.4–298.1	9.7	7.78	80.2
33X	18	1650	298.1–307.8	9.7	9.89	102.0
34X	18	1745	307.8–317.5	9.7	5.14	53.0
35X	18	1850	317.5–327.0	9.5	7.29	76.7
36X	18	1935	327.0–336.6	9.6	8.64	90.0
37X	18	2030	336.6–346.3	9.7	10.39	107.1
38X	18	2250	346.3–355.9	9.6	8.79	91.5
39X	19	0010	355.9–365.5	9.6	7.14	74.4
40X	19	0110	365.5–375.1	9.6	8.44	87.9
41X	19	0210	375.1–384.8	9.7	6.78	69.9
42X	19	0320	384.8–394.5	9.7	9.44	97.3
43X	19	0420	394.5–400.0	5.5	5.71	104.0
44X	20	0400	400.0–404.9	4.9	7.96	162.0
45X	20	0520	404.9–414.6	9.7	10.20	105.1
46X	20	0640	414.6–424.3	9.7	10.36	106.8
47X	20	0820	424.3–433.9	9.6	10.10	105.2
Coring totals				433.9	387.52	89.3

Note that times are given in Universal Time Coordinated (UTC), which is 10 hr later than local time (L).

lower-slope, mixed carbonate/siliciclastic facies and the more proximal, upper-slope facies at Sites 819 through 821. The area was first recognized as a potential ODP drilling target during a 1982 BMR sparker line that ran along the foot-of-the-slope (Line 41/064, Fig. 2). In 1987, the BMR vessel *Rig Seismic* conducted a site survey at this location (Symonds and Davies, 1988; Feary et al., 1990) and about 130 km of 24-channel, 80-in.^{3} water-gun seismic, magnetic, and bathymetric data were collected on a grid of northwest-southeast and northeast-southwest lines (BMR Lines 75/45, 75/46, and part of 75/47; Figs. 2 and 3). As proposed, the site lay at the intersection of two lines within this grid (Feary et al., 1990); the dip line was surveyed using our global positioning system (GPS), while the strike line was surveyed using a transit satellite/dead-reckoning (DR) system. The JOIDES PPSP recommended moving the site off this intersection, about 90 m southeast, away from the crest of a small, shallow, mounded feature seen in site-survey seismic data (Fig. 4).

An important requirement of Leg 133 site-location surveys was that seismic records obtained from the *JOIDES Resolution* resemble as much as possible those collected during the 1987 site surveys by the *Rig Seismic,* thus reducing ambiguity when defining the site or when comparing seismic stratigraphy between the two data sets. Accordingly, we modified the *JOIDES Resolution* seismic deployment systems.

The seismic transit line from the Site 820 to Site 822 area was designed to try to achieve a good, unambiguous, seismic tie that might allow us to compare the two areas. A previous attempt during the *Rig Seismic* site survey was thwarted by canyons that dissect the lower slope between the sites. In this case, ODP decided to attempt to tie along the upper-slope terrace just east of the Great Barrier Reef and then directly downslope to Site 822. Because Site 822 had been removed from the site-survey line intersection, the *JOIDES Resolution* survey was designed to record a new dip line across it, as well as to confirm its seismic character and position along the *Rig Seismic* strike line. Following the survey, we would relocate the site using confirmed GPS coordinates and the beacon dropped while maneuvering onto the location with the *Resolution's* dynamic positioning system. We expected that this method would allow us to position the vessel's moonpool accurately over the site–an important consideration for the small target area (less than 120 m wide) of Site 822.

Distribution of regional seismic data in the area around the site and the location of the *JOIDES Resolution* tie line are shown in Figure 2. Tracks of the original *Rig Seismic* site-survey and *JOIDES Resolution* site-location survey are shown in Figure 3. The *JOIDES Resolution*'s single-channel seismic profiling system was deployed soon after leaving Hole 821B at a heading of about 97°, while seismic recording began at JD 259/2038UTC, 16 September 1990, in calm seas (Beaufort Scale force 2), with swells of 1 to 2 m. The *JOIDES Resolution* sailed west-northwest across Site 820 and then northwest (about 325°) on the upper-slope tie line toward the Site 822 area, then on a heading of about 45° on the dip line across Site 822, on to a heading of about 145° on a strike line east of the site, and finally on a heading of about 330° back through the site, along the *Rig Seismic* strike line, to confirm its seismic character and position (Fig. 3). We stopped acquiring seismic data, and the equipment was retrieved at JD 260/0224UTC, 17 September 1990, after recording about 54 km of seismic and magnetic data. GPS navigation was used throughout the survey; we consider that the ship's track is accurately positioned. In general, our seismic equipment operated well, with the seismic cable streaming at about 10 m, and the two 80-in.^{3} water guns at a little over 3 m. The water guns developed problems with synchronization at the start of the dip line, across Site 822 (about JD 259/2345UTC), but these were remedied with the loss of less than 2 min of data. Good-quality analog monitor records were obtained (Fig. 5), while excellent correlation existed at the site between seismic profiles of the *Rig Seismic* and *JOIDES Resolution* (Fig. 4).

Following the survey, *JOIDES Resolution* returned to the confirmed GPS position of Site 822 at JD 260/0248UTC, 17 September 1990. Thrusters were lowered, and final positioning of the ship over the site was achieved using dynamic positioning. A beacon was dropped at JD 260/0344UTC; final coordinates of the Hole 822A are 16°25.379′S and 146°12.904′E, with a water depth of 955.2 m (drill-pipe measurement from sea level).

Basement is not clearly defined in either the *JOIDES Resolution* or *Rig Seismic* water-gun data across the site; however, for normal resolution air-gun data in an equivalent position south of the site (Shell Lines 1124 and 1125; Fig. 2), it may be about 4 s TWT below the seafloor. The site is

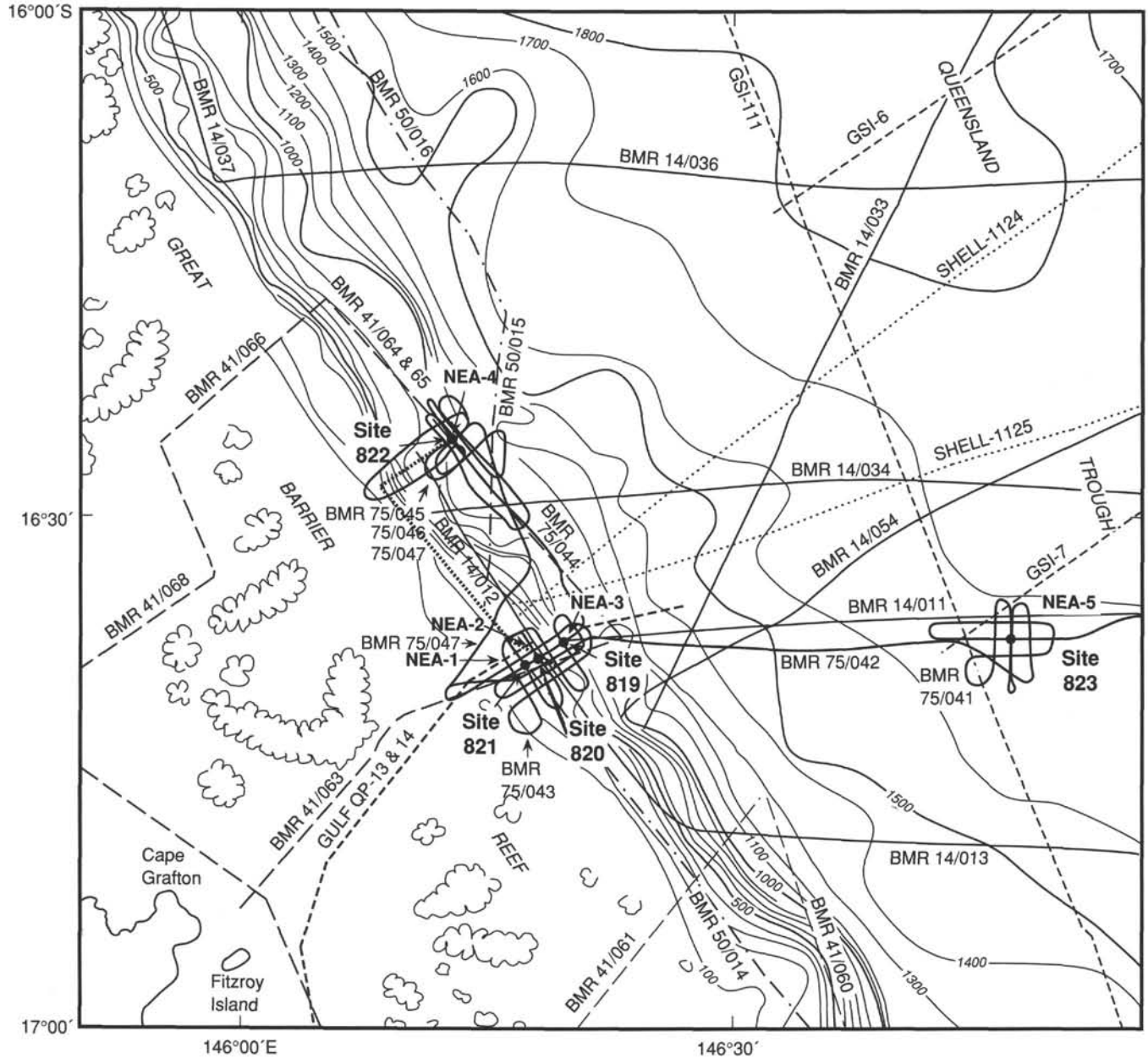

Figure 2. Track chart showing distribution of regional seismic data around Site 822 and location of *JOIDES Resolution* tie-line between Sites 821 and 822. Also shows locations of Sites 819, 820, 821, and 823 and simplified bathymetry in meters.

underlain by an upper, 0.23 s TWT (~178 m) thick, complex seismic unit that consists of channels, mounds, and drape facies (Fig. 4). These facies commonly are made up of high-amplitude, parallel reflector packages; however, some of these mounds, particularly near the base of the unit, contain low-amplitude, discontinuous reflectors. The underlying 0.14 s TWT (~125 m) thick drape and channel-fill unit is composed mainly of high-amplitude, parallel reflectors, but with a thin, reflection-free zone at its base. The next unit is 0.09 s TWT (~80 m) thick and forms the flank of a broad, eroded mound that extends south of the site. It consists of flat-lying, parallel, low-amplitude reflectors. The top of the underlying unit lies near TD and extends about 0.2 s TWT below it. This unit contains zones of high- and low-amplitude, subparallel reflectors and low-relief channels and mounds.

To provide us with predictive capability during drilling at Site 822, we estimated the TWT/depth relationship below the seafloor using stacking-derived interval velocities from the BMR site-survey seismic lines across the site. In Figure 6, we compare this relationship with similarly derived TWT/depth relationships for the Great Barrier Reef upper-slope sites (Sites 819–821) and with those for pure carbonate slope sites on the margins of Queensland Plateau (Sites 817 and 818).

LITHOSTRATIGRAPHY

Site 822 is located on the lower slope to foot-of-slope extending eastward from the Great Barrier Reef into Queensland Trough. The site is slightly northeast of a transect across the outer shelf and upper slope that is represented by Sites

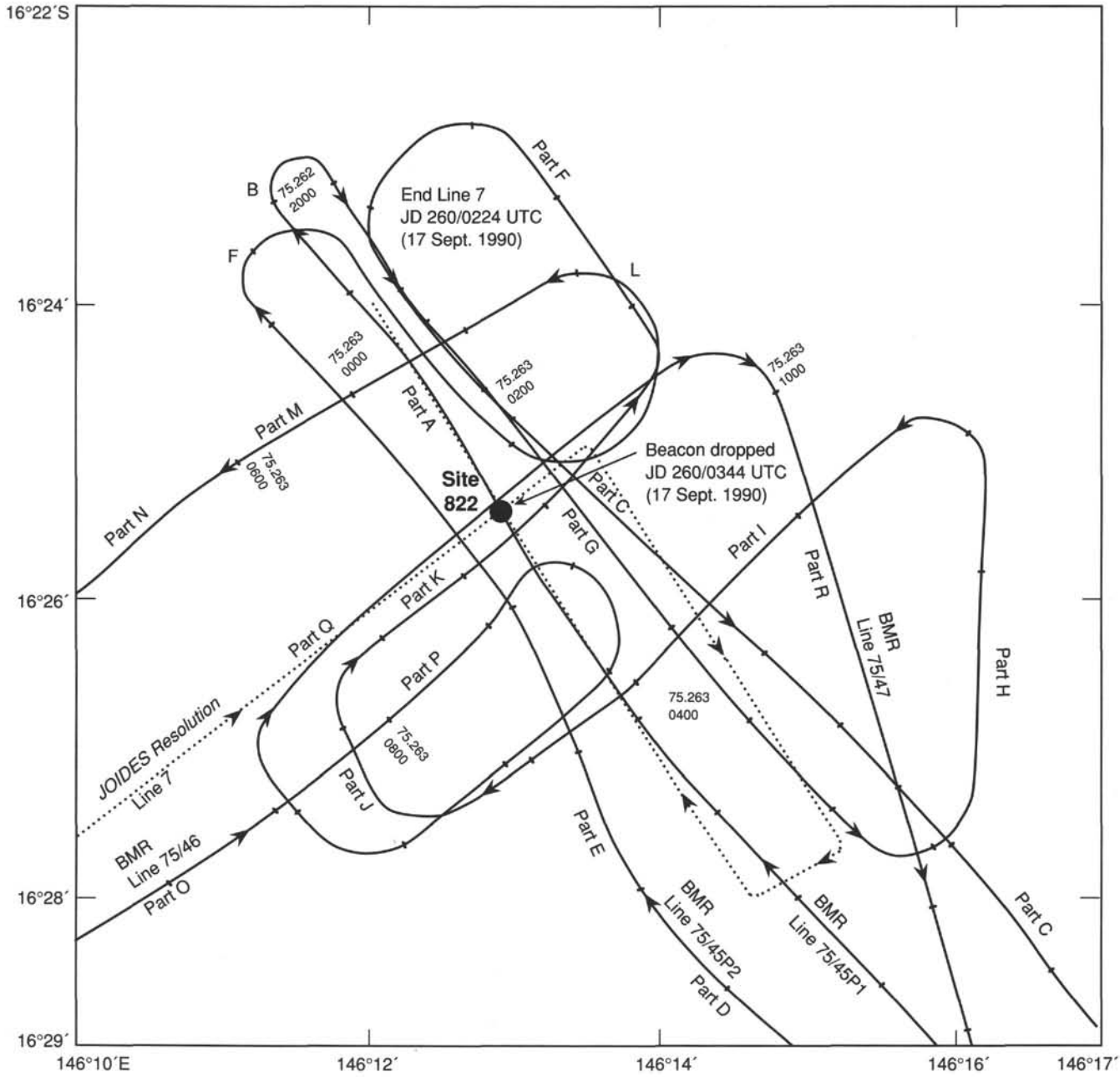

Figure 3. *JOIDES Resolution* Leg 133 site-location tracks (dotted line) and *Rig Seismic* 1987 site-survey tracks (solid line) around Site 822.

819, 820, and 821 (Fig. 7). It is west and upslope of Site 823, which is nearer the axis of the margin-parallel Queensland Trough.

A single hole (822A) was drilled at this site that penetrated the upper 95.9 mbsf using the APC and continuing to a total depth of 433.9 m with the XCB; recovery was very good (89.3%). Sediments recovered at Site 822 are predominantly mud that contains varying amounts of carbonate ooze and terrigenous clay with lesser bioclastic and terrigenous (mostly quartzose) sand and silt. A number of lithologic units can be distinguished by subtle variations in composition and by the presence of a possible unconformity at the top of the sequence. The sequence ranges in age from late Pliocene (CN12a, >2.6 Ma) to Pleistocene (CN15, <0.275 Ma). Unit I consists of mostly clayey calcareous mud (>60%) having soft sediment deformation (slump folds). Nannofossils indicate that a possible unconformity may exist between Subunits IA and IB, with a possible hiatus spanning the time between 0.275 and 0.465 Ma (Subzone CN14b apparently is missing). The rest of the section has no obvious lithostratigraphic or biostratigraphic breaks, but seismic data suggest that other unconformities may exist in the sequence (see "Seismic Stratigraphy" section, this chapter). Unit II is similar to Unit I, except that it is darker in color (dark greenish-gray) and contains more terrigenous clay. This unit consists of clayey calcareous mixed sediment (mud) interbedded with clayey nannofossil ooze in the upper part (Subunit IIA). Forming the middle part, Subunit IIB becomes increasingly clay-rich and includes calcareous claystone. Bioclastic sediment becomes more abundant in the lower part (Subunit IIC), resulting in a higher carbonate content. All the boundaries between the sub-

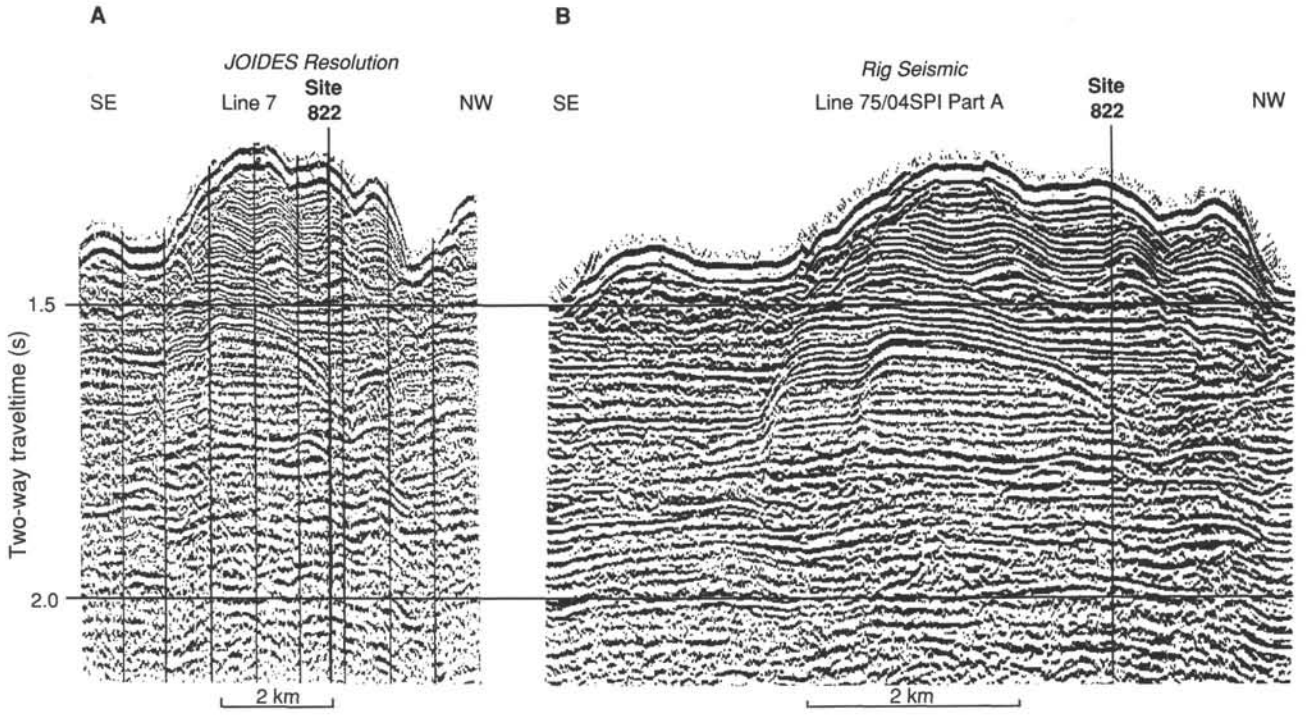

Figure 4. Comparison of *JOIDES Resolution* and *Rig Seismic* 80-in.^{3} water-gun seismic profiles across Site 822.

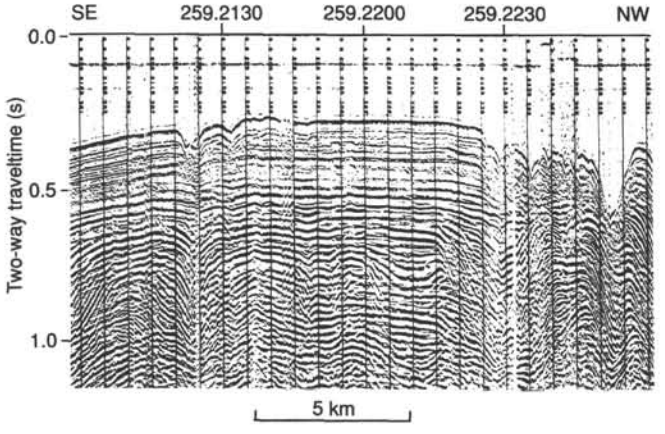

Figure 5. Part of the *JOIDES Resolution* shipboard analog single-channel seismic profile collected on tie-line between Sites 820 and 822 using two 80-in.^{3} water guns.

units of Unit II are gradational, but appear to be seismic sequence boundaries, with a possible erosional unconformity between Subunits IIB and IIC.

Lithologic Units

Unit I (Core 133-822A-1H to Section 133-822A-7H-3; depth, 0–52.9 mbsf; thickness, 52.9 m; age, Pleistocene [CN15 to CN14])

Unit I consists of mostly clayey calcareous mud (> 60% $CaCO_3$) and locally shows evidence of soft-sediment deformation (slump folds). Nannofossil markers indicate that a possible unconformity exists between Subunits IA and IB, with a possible hiatus spanning the time between 0.275 and 0.465 Ma (Subzone CN14b apparently is missing). Subunit IA is distinguished by its variegated light greenish-gray to white hue and its variable proportions of carbonate vs. clay, which range from

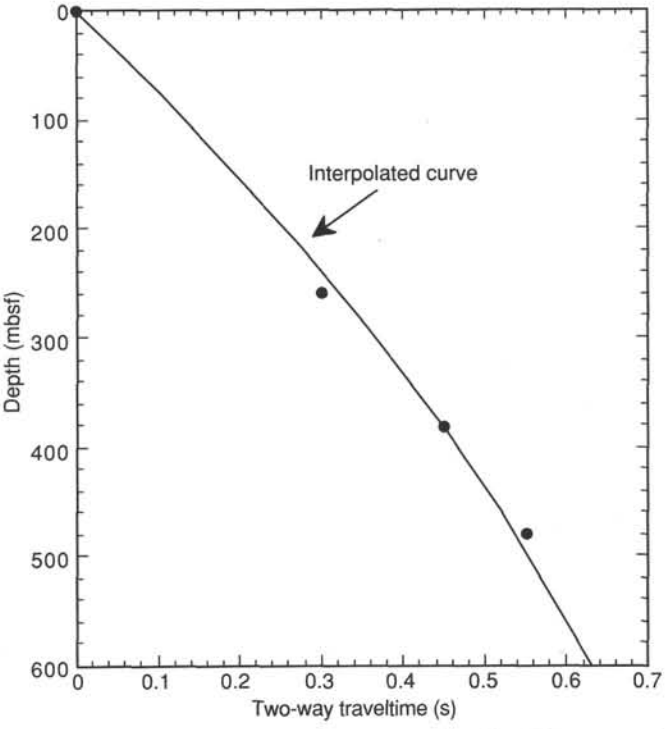

Figure 6. Reflection time (TWT)/depth curve for Site 822, computed using stackingderived interval velocities from *Rig Seismic* site-survey seismic data.

clayey bioclastic ooze to mixed sediment with nannofossils. Subunit IB consists entirely of clayey nannofossil ooze with bioclasts and is carbonate-rich. These subunits were differentiated because of the possible unconformity separating them and because of slight differences in lithology.

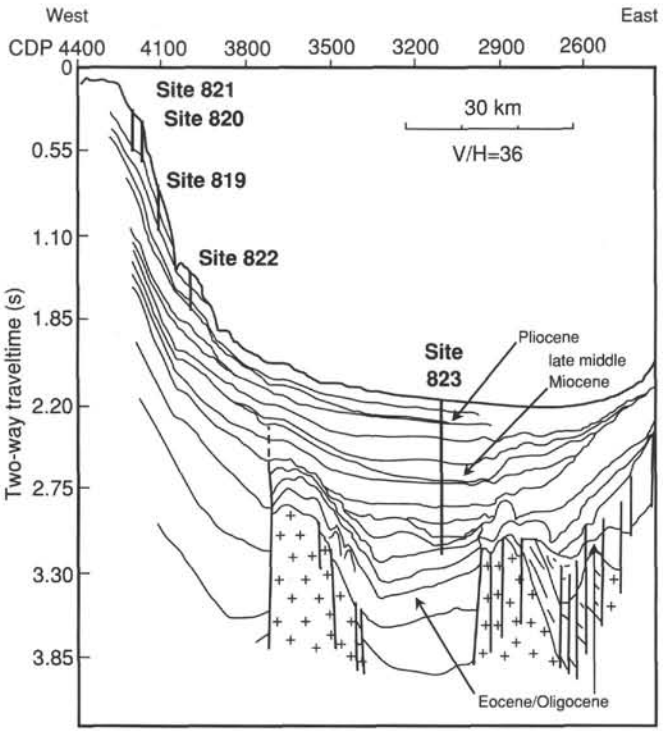

Figure 7. Idealized cross section across the western part of the Queensland Plateau transect (modified after Feary et al., 1990).

Subunit IA (Cores 133-822A-1H to Section 133-822A-4H-5; depth, 0–27.4 mbsf[?]; thickness, 27.4 m [?]; age, late Pleistocene [CN15, <0.275 Ma])

Subunit IA consists of mostly clayey bioclastic calcareous ooze with nannofossils, micrite, and scattered pteropods. Lesser intervals of clayey calcareous mixed sediment (mud) are similar to this ooze, but contain more terrigenous clay and silt. Carbonate contents (measured within a unit range of between 53.3% and 70.0%, see "Inorganic Geochemistry" section, this chapter) are (along with Subunit IB) among the highest carbonate values for Site 822. In the lower part, finely laminated clayey nannofossil ooze contains bioclasts and siliciclastic sediments. The unit is variegated with small-scale color changes (shades of light to medium greenish-gray) evident in banding, fine lamination, and mottling. The oozes are highly bioturbated, and locally, burrows are filled with sand-sized bioclasts and pteropods. Bioclastic packstone occurs as thin lenses in Section 133-822A-2H-6, 100–120 cm. Soft-sediment deformation in the lower part probably represents slump folds and may be related to the unconformity at the base of the unit (Fig. 8).

Subunit IA is late Pleistocene in age (CN15, <275 Ma). Nannofossil zonation indicates that a possible unconformity may exist between Subunits IA and IIB. Within the interval between 19.9 and 29.4 mbsf (core-catcher samples from Cores 133-822A-3H and -4H), a possible hiatus spans the time between 0.275 and 0.465 Ma (Subzone CN14b apparently is missing). The precise depth of the contact between Subunits IA and IB is uncertain, but may be at the base of Section 133-822A-4H-5, where the sedimentary character changes from the laminated ooze of Subunit IA to the more homogeneous ooze of Subunit IB. We hope that additional biostratigraphic analyses will better constrain the position and nature of this unconformable contact.

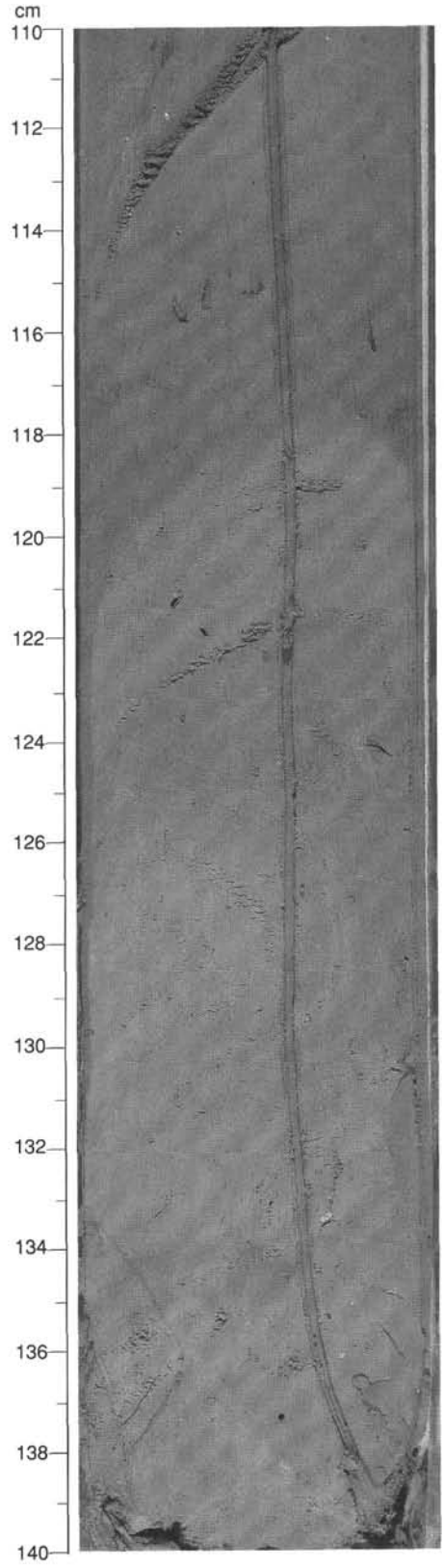

Figure 8. Deformation of soft sediments at the base of Unit I. Also note the color-banding and lamination that is characteristic of Unit I. Vertical furrow is an artifact of core splitting (interval 133-822-3H-4, 110–140 cm).

Subunit IB (Sections 133-822A-4H-6 to -7H-3; depth, 27.4[?] to 52.9 mbsf; thickness, 25.5 m; age, Pleistocene [CN14a])

Subunit IB consists entirely of clayey nannofossil ooze with bioclasts and consistently has the highest carbonate contents recorded for Site 822 (59.5%–79.3%). The unit is light-colored (ranging from greenish-white to greenish-gray) and is highly bioturbated and color-mottled. Rare bioclastic grains occur as very fine sand to silt (rare, very coarse sand) in interbeds and as burrow-fill deposits. Foraminiferal packstones are slightly coarser (fine- to medium-grained) sand and are commonly pyritized. Scattered shell fragments occur in Section 133-822A-6H-3. Possible soft-sediment deformation in Sections 133-822A-6H-3 and -7H-3 may indicate slumping. The subunit gradationally overlies Subunit IIA and becomes progressively darker and more clay-rich down the section. The contact has been arbitrarily placed at the bottom of Section 133-822A-7H-3, below the lowest part of the continuous interval of clayey nannofossil ooze comprising Subunit IB (64.8% $CaCO_3$) and above less calcareous clayey to silty mixed sediment of Subunit IIA. Subunit IB is entirely late Pleistocene in age (nannofossil Zone CN14a).

Unit II (Section 133-822A-7H-4 to Core 133-822A-47X; depth, 52.9–433.9 mbsf; thickness, 381.0 m; age, Pliocene to Pleistocene [CN12a–CN14a])

Unit II is similar to Unit I, except that it is a darker color (dark greenish-gray) and contains more terrigenous clay. The unit consists of clayey calcareous mixed sediment (mud) interbedded with clayey nannofossil ooze in the upper part (Subunit IIA). Forming the middle part, Subunit IIB becomes increasing clay-rich and includes calcareous claystone. Bioclastic sediment becomes more abundant in the lower part (Subunit IIC), resulting in a higher carbonate content. All the boundaries among the subunits of Unit II are gradational, but may be seismic sequence boundaries, with a possible erosional unconformity between Subunits IIB and IIC (see "Seismic Stratigraphy" section, this chapter).

Subunit IIA (Section 133-822A-7H-4 to Sample 133-822A-23X-1, 0–95 cm; depth, 52.9–202.5 mbsf; thickness, 149.6 m; age, Pleistocene [(CN13b–CN14a])

Subunit IIA is similar to Subunit IB, except that it is more clay-rich and generally darker colored. It consists of mostly clayey to silty calcareous mixed sediment (mud) interbedded with clayey nannofossil ooze in the upper part. The middle part of the subunit is unusual in that it contains abundant quartz silt and lesser very fine sand that increase downward to a maximum of 32% in Core 133-822A-17X. Clayey calcareous mixed sediments become partially lithified in the lower part of the subunit (Core 133-822A-14X and below). In Section 133-822A-14X-CC, an unusually well-lithified, dolomitized mudstone contains pyritized foraminifers and has moldic porosity. Intervals of silty calcareous claystone become thicker and more common down the section and are most abundant below Core 133-822A-17X. We arbitrarily placed the contact in Section 133-822A-23X-1 at 95 cm, where the last thick interval of calcareous clayey mixed sediment (silty mud) overlies smooth, dark-colored, calcareous claystone of Subunit IIB.

Bioturbation is common throughout Subunit IIA, although one cannot see it easily in XCB cores (Core 133-822A-12X and lower). Very fine to fine bioclasts most commonly occur as burrow fills or as grains or shells that have disseminated in the muddy sediments and locally are abundant enough to have a wackestone texture. Less commonly, very thin beds of bioclastic to foraminiferal packstone (turbidites) are usually very fine- to fine-grained sand or silt and locally exhibit size grading. Cyclical variations in color in the unit are related to variations in clay/carbonate contents (Fig. 9).

Subunit IIB (intervals 133-822A-23X-1, 95–150 cm, to -36X-2, 0–55 cm; depth, 202.5–332.5 mbsf; thickness, 130 m; age, late Pliocene to Pleistocene [CN13a or CN12d to CN13b])

Subunit IIB is dominated by calcareous claystone and has lesser clayey mixed sediments with nannofossils, bioclasts, and minor quartz. Carbonate contents measured in the unit generally are below 50%, typically between 20% and 40%, but with values as low as 16.6%. Quartz silt and very fine sand occur in most of the sediments, but generally are below 10% (quartz contents range between 2.4% and 12.7%; see "Inorganic Geochemistry" section, this chapter). Intervals of dark greenish-gray, calcareous claystone generally are well-compacted and partially lithified. Lighter greenish-gray, more calcareous (40%–61% carbonate), clayey mixed sediments occur as discrete intervals up to 5.6 m thick in Cores 133-822A-29X and -30X and 8 m in Core 133-822A-33X. The mixed sediments consist of chalky calcareous clayey mudstone to silty mudstone with scattered bioclasts and quartz grains. In Core 133-822A-31X, several very thin (<1–5 cm) interbeds of very fine- to fine-grained, bioclastic to quartzose sand are graded and may represent thin turbidites.

Subunit IIC (interval 133-822A-36X-2, 0–55 cm, to Core 133-822A-47X; depth, 332.5–433.9 mbsf; thickness, 101.4 m; age, late Pliocene [CN12a to CN12d or CN13a])

Subunit IIC is distinguished by its high-carbonate-content nannofossil clayey mixed sediment with bioclasts and quartz with silty to sandy mudstone and wackestone textures. Most of the subunit is well-compacted and semilithified. Intervals of dark greenish-gray calcareous claystone cyclically alternate with slightly lighter-colored mixed sediment. Bioclasts are most common in the mixed sediment and contribute to the high carbonate content. Quartz silt and very fine sand increase downward, while geochemical analyses indicate contents as high as 17% in the lower part of the hole. Nannofossils become more common in the silty claystone in the lower part of Subunit IIC.

In Core 133-822A-47X, very thin beds of foraminiferal bioclastic packstone with nannofossils and clay may represent turbidites. In Section 133-822A-47X-3, a relatively thick bed (23 cm) of bioclastic foraminiferal packstone was unlithified and soupy and had been disturbed by drilling. In Section 133-822A-45X-4, sandy bioclastic packstone has nearly vertically inclined bedding, which represents either a slumped interval or drilling disturbance. Foraminifers are not abundant, but locally, are concentrated in well-sorted sandy beds that may be turbidites (Sections 133-822A-42X-2 and -42X-6). Possible rock fragments (or fragments of *in-situ* lithified sediment) occur in Core 133-822A-38X. In the upper part of Core 133-822A-47X and in Section 133-822A-44X-5, we noted authigenic dolomite in silty bioclastic mixed sediment (mudstone).

Interpretations

Sediments recovered at Site 822 are predominantly mud that contains varying amounts of carbonate ooze and terrigenous clays with lesser bioclastic and terrigenous (mostly quartzose) sand and silt. The mud-dominated sequence is

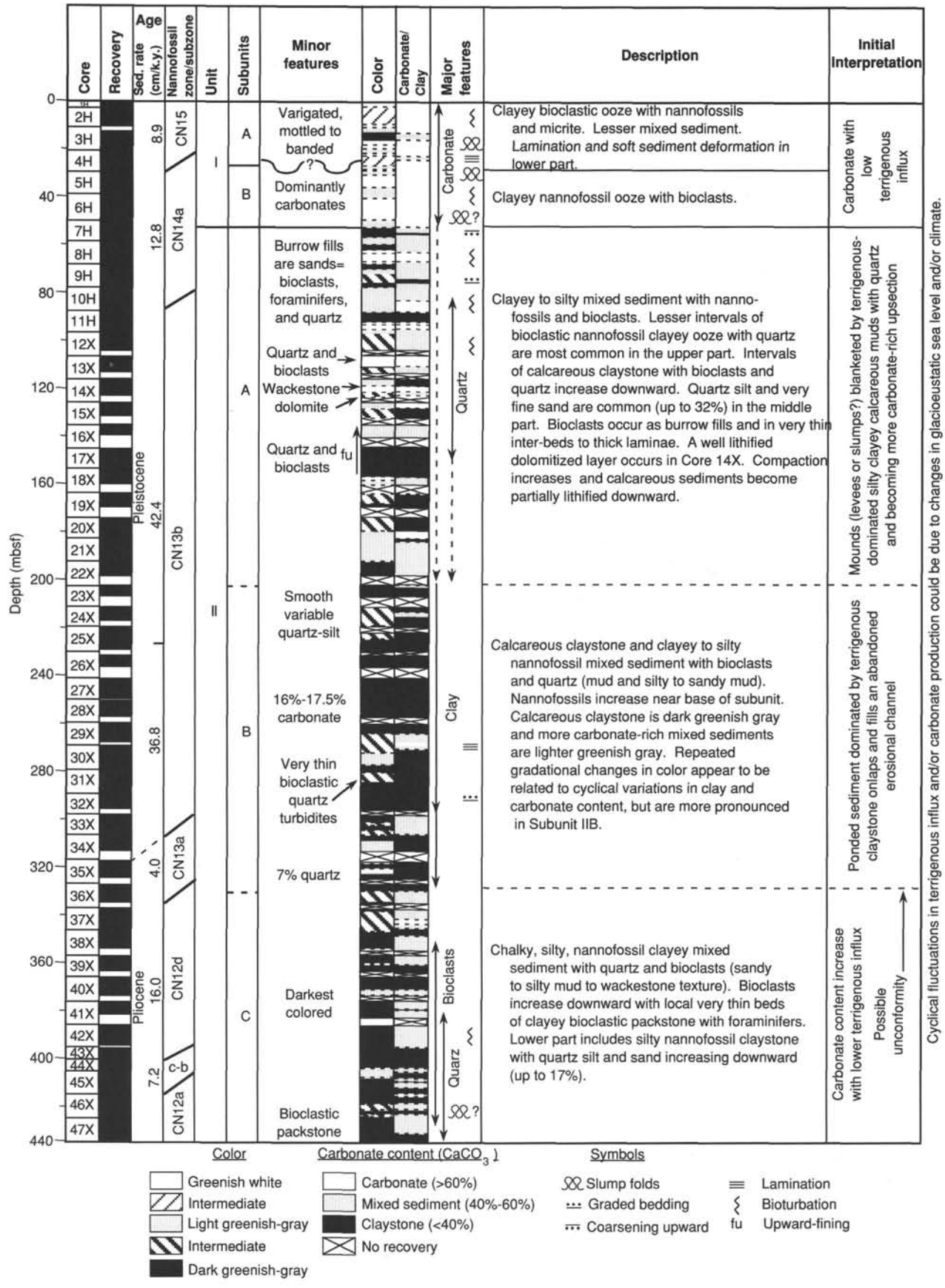

Figure 9. Generalized stratigraphic column for Site 822.

typical for a lower-slope depositional environment (Read, 1984). Most of the coarse-grained terrigenous and platform-derived sediment presumably bypassed the slope and was deposited on the floor of Queensland Trough, as seen at Site 823. Bathymetric profiles show that the slope is cut by a series of gullies and small canyons. Seismic profiles indicate that similar features probably cut the slope during much of Pleistocene and late Pliocene time (see "Seismic Stratigraphy" section, this chapter). The muddy sediments eroded from the walls of these canyons was transported into Queensland Trough as slumps and debris flows and, to a lesser extent, as turbidites and grain flows. These erosional depressions later were covered with muds that either draped the irregular surface or filled the ponded depressions and thinned or pinched out over highs between gullies.

In-situ benthic foraminifers indicate that Site 822 remained at or below the middle bathyal zone (>600 m, but less than 1000 m); depths thus were similar to those of today (963-m water depths) throughout deposition. Many of the benthic foraminiferal assemblages analyzed contain shallow-water contaminants that must have been transported down the slope and redeposited (see "Biostratigraphy" section, this chapter). Bioclasts, aragonite, and high-Mg calcite occur throughout the sequence, indicating that the sediment was partially derived from neritic carbonate sources, such as the Great Barrier Reef (see "Inorganic Geochemistry" section, this chapter). Because intense bioturbation and disruption from XCB drilling obliterated most sedimentary structures and homogenized the sediments, the mechanisms of redeposition of neritic-derived bioclastic silt to sand and terrigenous clastic sediments are unclear. A few thin beds of foraminiferal bioclastic packstone were transported by turbidity currents. Deformation of soft sediments indicates that slumping occurred at several horizons.

Although the sequence is monotonous lithologically and consists almost entirely of mud, it has distinct cyclical variations in color and composition related to fluctuations in proportion of terrigenous vs. carbonate sediments. Terrigenous clay and silt occur throughout the sequence, but variable amounts (21%–83%) suggest that variations in rate of terrigenous influx were important for determining composition of these sediments. In general, carbonate contents decrease from high proportions in Unit I (≤79%) downward to low proportions (≧17%) in Subunit IIB and increases slightly in Subunit IIC (≤61%). At higher frequencies, cyclical variations in carbonate and clay contents at Site 822 record changes in the flux of terrigenous vs. carbonate sediment through much of the Pleistocene and late Pliocene, possibly related to changes in glacioeustatic sea level and/or climate.

Unit I

The high contents of carbonate and aragonite (up to 79% $CaCO_3$) in Unit I indicate that the interval is predominantly periplatform ooze with lesser contributions of terrigenous clay and silt and pelagic nannofossils. Relatively low sedimentation rates (8.9–12.2 cm/k.y.) result from an upward reduction in terrigenous influx from that found in Unit II. A possible unconformity between Subunits IA and IB may correlate with the unconformity and slump horizon recognized on the upper slope at Site 819, suggesting that widespread erosion and slumping may have affected much of the slope during the time between 0.275 Ma and 0.465 Ma. This contrasts with Sites 820 and 821 on the outer shelf, where thick successions of sediment of that age are present, indicating that slumping did not affect the upper slope.

Subunit IIA

A progressive decrease in carbonate content downward in Subunit IIA may be the result of dilution by a major influx of terrigenous sediments. The sedimentation rate in Subunit IIA appears much higher than that for Subunit IB (42.4 cm/k.y. vs. 12.8 cm/k.y), suggesting that a downward increase in siliciclastic sediments results from a greater terrigenous influx (Fig. 9, also see "Sedimentation Rates" section, this chapter). Quartz silt and sand are more abundant at Site 822 (up to 32%) than at Sites 819 through 821, indicating that these relatively coarse siliciclastic sediments bypassed the shelf and were deposited on the lower slope (Fig. 10; "Inorganic Geochemistry" section, this chapter). Interestingly, if the quartz component were subtracted from total sediments, the remaining sediments at Site 822 become relatively carbonate-rich, similar to the trends evident in sediments of similar age at Sites 819 through 821 (Fig. 11; "Inorganic Geochemistry" section, this chapter). At a higher frequency, cyclical variations in contents of carbonate and clay at Site 822 record changes in the flux of terrigenous vs. carbonate sediments through much of the Pleistocene and late Pliocene, possibly related to changes in glacioeustatic sea level and/or climate (Fig. 12; "Inorganic Geochemistry" section, this chapter).

Estimates of velocity and seismic data indicate that Subunit IIA has a mounded character and irregular internal reflectors in the lower part, draped by high-amplitude reflectors that maintain the original mounded morphology (see "Seismic Stratigraphy" section, this chapter). Locally, downlapping and onlapping of basal reflectors in this seismic package suggest that the contact between Subunits IIA and IIB may be a sequence boundary. These mounds might be slumps, levees, or some other small localized buildups of redeposited sediments. These seismic characteristics differ from the seismic character of Subunit IIB (see below) and may be related to the coarse-grained nature of Subunit IIA.

Subunit IIB

Subunit IIB is dominated by terrigenous sediments, mostly clay with lesser amounts of quartz silt and carbonate sediments. The estimated sedimentation rates for this unit are variable and range from 7.2 cm/k.y. at its base, to 36.8 cm/k.y. in the middle, and 42.4 cm/k.y. in the upper part (averaged with Subunit IIA; see "Sedimentation Rates" section, this chapter). Thus, much of the unit has relatively high sedimentation rates, which suggests that terrigenous influx is a major influence. Most of the sediments are hemipelagic and were transported as suspended sediments, in contrast to the significant coarse fraction in Subunit IIA. Estimates of velocity and seismic data indicate that Subunit IIB may represent ponded fill that laps onto the side of an erosional channel and thins southward over an adjacent high (see "Seismic Stratigraphy" section, this chapter). The even, parallel, high-amplitude reflectors in this seismic package are compatible with the fine-grained, clay-rich nature of Subunit IIB. Beneath the unconformity, seismic reflectors clearly are truncated and provide evidence of erosion on the lower slope and a significant hiatus. However, biostratigraphic data do not indicate an unconformity, but contain all the nannofossil zones that represent the Pliocene/Pleistocene boundary, which occurs in the lower part of Subunit IIB. The duration of time missing across this unconformity is unknown, but might account for the low sedimentation rates (7.2 cm/k.y.) in the lower part of the unit.

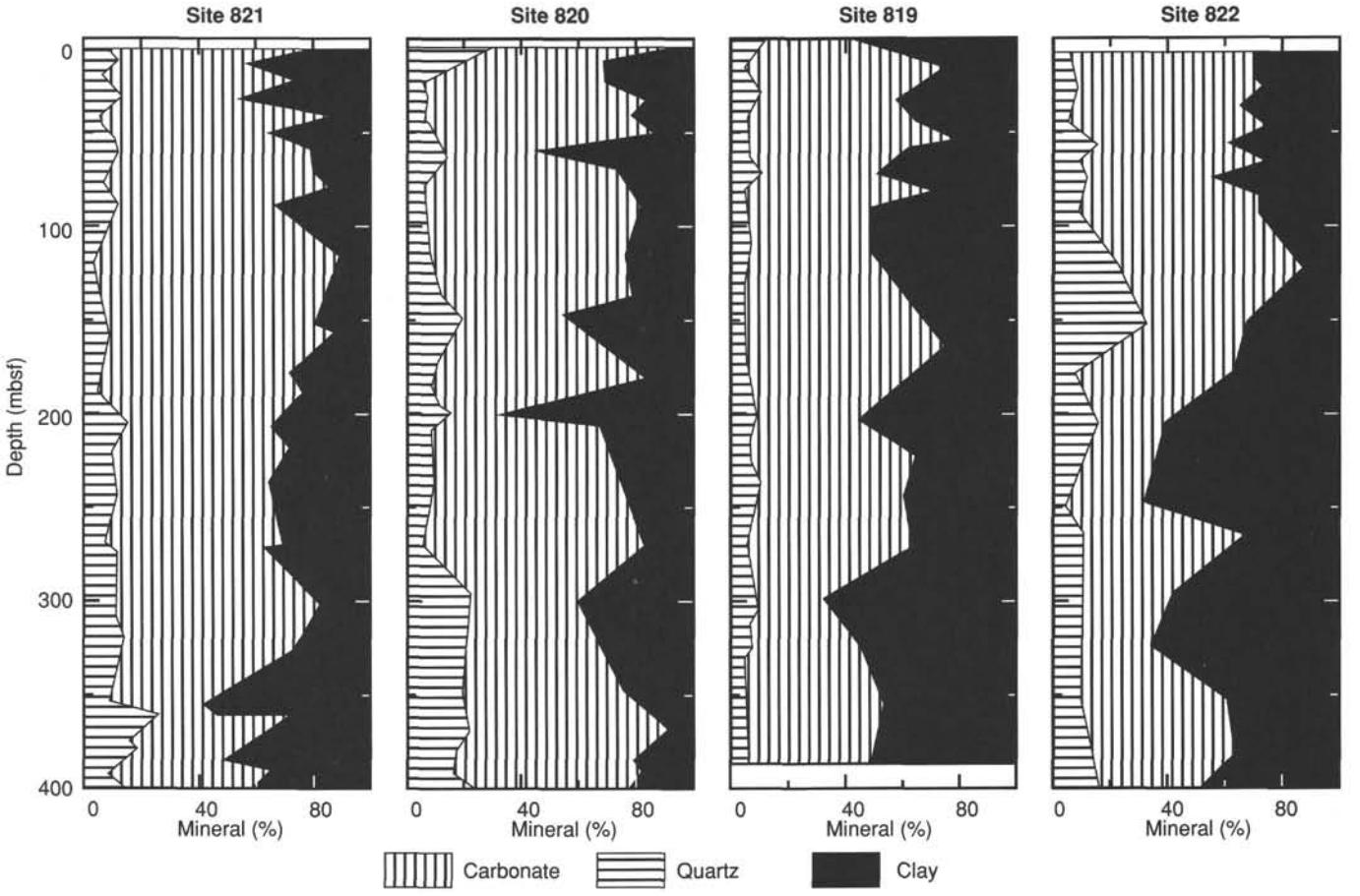

Figure 10. Summary of percentages of quartz, carbonate and "clay" fraction for Leg 133 four continental sites (Sites 819 through 822).

Subunit IIC

An increase in carbonate sediments downward in Subunit IIC may result from an accompanying decrease in the supply of terrigenous sediments, as indicated by increases in both platform-derived bioclasts and pelagic nannofossils. Sedimentation rates for Subunit IIC are considerably less (two to nine times lower) than those in Subunit IIB, with estimates for different parts of the section ranging from 4 to 16 cm/k.y (see "Sedimentation Rates" section, this chapter). Reduced influxes of terrigenous sediment are implied by lower sedimentation rates, while this diminished dilution may have resulted in a concomitant increase in carbonate contents in Subunit IIC. As noted in Subunit IIB, the top of Subunit IIC may represent a seismic sequence boundary and is truncated by an erosional unconformity. The character of the reflectors beneath this unconformity is different from that in Subunit IIB, with discontinuous low-amplitude reflectors that form a broad mound beneath the unconformity. Truncation of several reflectors indicates that much of the mound's paleotopography results from erosion, but the mound may be partially depositional in origin. Evidence of this hiatus may explain the anomalously low estimates of sedimentation rates for the uppermost part of the unit (7.2 cm/k.y.; see "Sedimentation Rates" section, this chapter). An increase in quartz silt toward the base of Subunit IIB precedes an increase in carbonate in the upper part of the subunit and may be similar to that seen in Subunit IIA.

Summary

The Pliocene to Pleistocene sequence at Site 822 records variations in flux of terrigenous and carbonate sediments along the slope that bounds the Great Barrier Reef and Queensland Trough. Overall, the upper part (Unit I) is carbonate-rich and a decrease downward in carbonate occurs in Subunits IIA and IIB, which is followed by an increase in carbonate in the Pliocene Subunit IIC. Superimposed on these overall variations, short-term cyclical variations in composition, texture, and color may be related to fluctuations in sea level, such as Milankovitch cycles.

Unit I formed during a time of rapid oscillations in sea level during the latest Pleistocene. The possible unconformity between Subunits IA and IB, with a hiatus between 0.275 and 0.465 Ma, might have resulted from failure of the slope associated with the fourth-order sequence boundary/lowstand at 0.4 Ma. However, the absence of slumping or erosion at Sites 820 and 821 on the outer shelf suggests that slumping probably was not induced by lowstand erosion of the shelf edge.

Most sediments of Subunits IIA and IIB formed between 0.93 to 1.48 Ma, during a postulated eustatic highstand in sea level. However, this interval is dominated by siliciclastic sediments, with quartz, silt, and very fine sand that increases in the middle of Subunit IIA and clays that dominate in Subunit IIB, suggesting that this eustatic highstand was overwhelmed by a huge influx of terrigenous sediments. The seismic sequence boundary between these subunits (age inter-

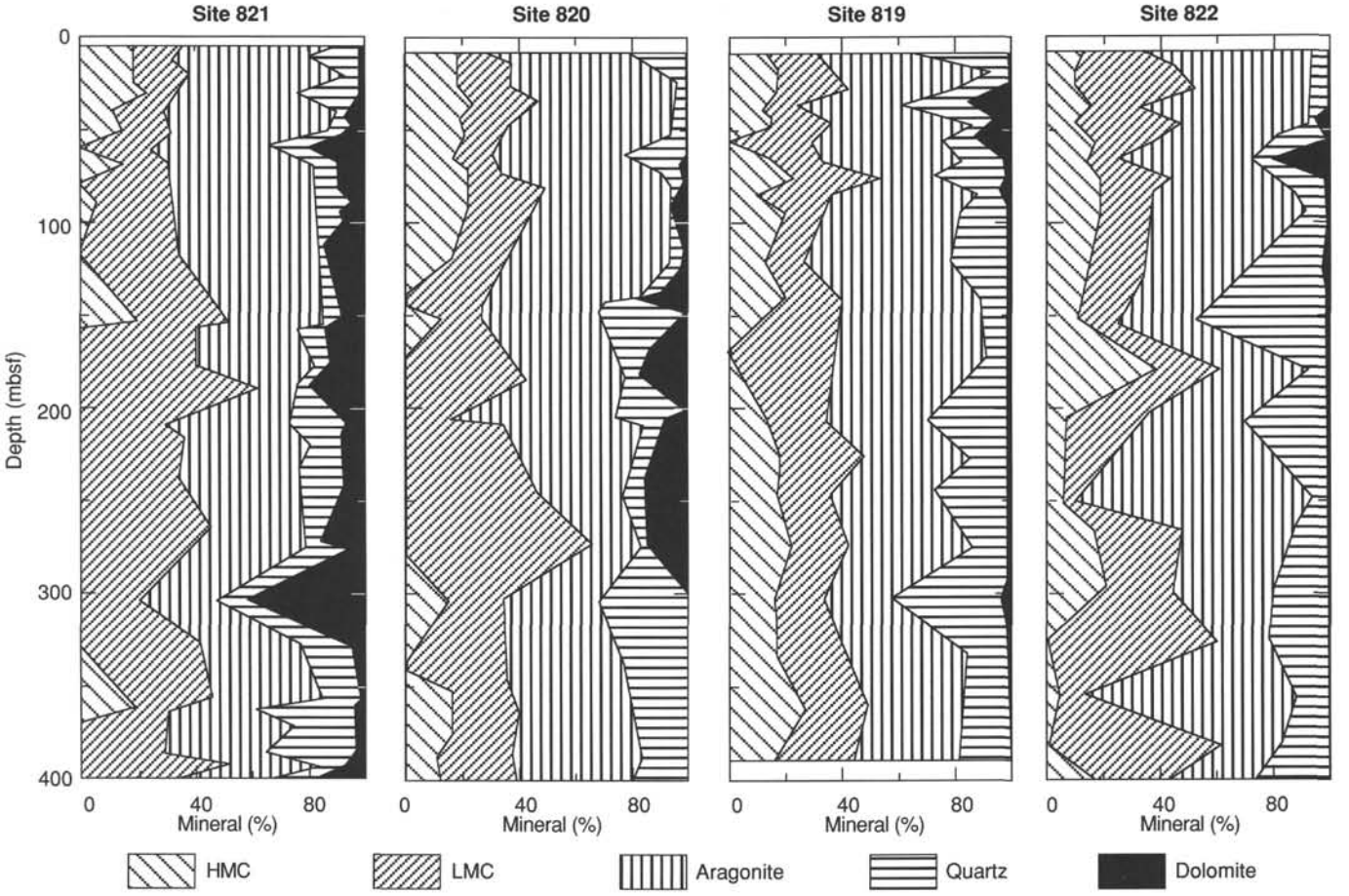

Figure 11. Summary of X-ray mineralogy for Sites 819 through 822. Note the increasing percentage of dolomite in sites nearest the continental margin.

polated as 1.21 Ma) may not be related to any eustatic change in sea level. Small-scale cyclicity in Subunits IIA and IIB has a much higher frequency than is shown on available eustatic curves, but might represent Milankovitch cycles.

The Subunit IIB/Subunit IIC boundary represents a seismic sequence boundary (erosional unconformity), and a condensed sequence of calcareous claystone at the base of Subunit IIB spans the time between 1.48 and 1.88 Ma–a time thought to have been a period of relative eustatic lowstands. Any coarse-grained terrigenous or carbonate sediments supplied during this time may have bypassed the slope, but may have caused significant amounts of erosion and gullying of the slope. Carbonate-rich sediments in the upper part of Subunit IIC were deposited between 1.88 and 2.29 Ma, during a postulated eustatic rise in sea level, which might explain the increase downward in bioclastic carbonates and/or reduction in terrigenous influxes. In the lower part of Subunit IIC, nannofossil claystone and clayey mixed sediments exhibit an increase in quartz silt downward that range in age from 2.29 to >2.6 Ma. A source of these bioclastic sediments presumably would be the adjacent northeastern Australian shelf. Shore-based studies of composition and origin of bioclastic sediments may provide insights about the nature of a shallow-marine source of Pliocene and other bioclastic sediments.

BIOSTRATIGRAPHY

Sediments at Site 822 yielded excellent recovery of calcareous nannofossils, planktonic foraminifers, and benthic foraminifers. The section contains a significant hiatus in the upper Pleistocene sediments, is greatly expanded in the lower Pleistocene, and terminates in the mid- to upper Pliocene. A middle bathyal depth prevailed during deposition of the entire section.

Calcareous Nannofossils

Site 822 was cored to 434 mbsf and yielded an expanded Holocene to upper Pliocene section of hemipelagic sediments. Contents of nannofossils vary from about 1% to as much as 25% or more. Preservation of nannofossils generally is very good, and in many samples coccoliths are in a near-pristine state. All important and conventionally used Pleistocene and upper Pliocene nannofossil biomarkers were recognized; however, the succession suggests a significant unconformity in Core 133-822A-4H. Other unconformities may exist, but are not readily apparent from our preliminary biostratigraphy. A graphic presentation of biostratigraphy is presented in Figure 13. A brief description of nannofossil biostratigraphy follows.

Emiliania huxleyi occurs as an abundant or common constituent in core-catcher samples of Cores 133-822A-1H through -3H; all three cores were assigned to the *Emiliania huxleyi* Zone (CN15) and are younger than 275 k.y. The next lower biohorizon, the highest occurrence of *Pseudoemiliania lacunosa* (0.465 Ma), is found in Sample 133-822A-4H-CC. This marker almost certainly occurs higher in the core than the core-catcher sample and as *Emiliania huxleyi* almost certainly also occurs within the upper part of Core 133-822A-4H, we think it likely that much–perhaps all–of the section

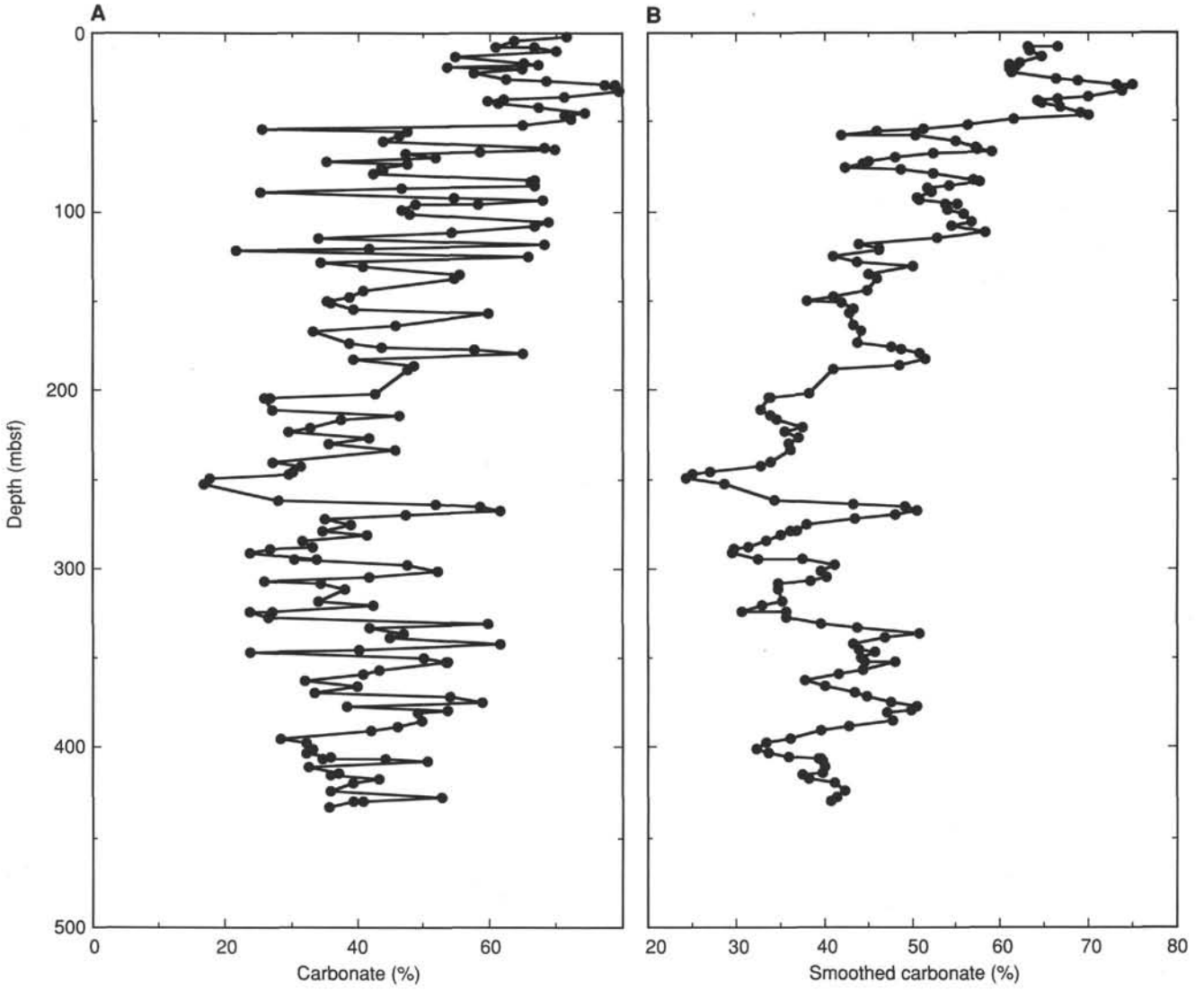

Figure 12. Carbonate data for Site 822 as a function of depth. **A.** Raw data. **B.** Smoothed data.

representing the time interval between these two biohorizons is missing.

The next biohorizon recognized was the top of the interval of dominance of small *Gephyrocapsa* (0.93 Ma) in Sample 133-822A-10H-CC, which was followed by the highest occurrence of *Helicosphaera sellii* (1.27 Ma) in Sample 133-822A-25X-CC. An unusually thick accumulation of sediments occurs between these last two biohorizons, as has been seen at nearly every site where this interval was recovered along the northeastern Australian margin.

The highest occurrence of *Calcidiscus tropicus* (1.48 Ma) is next below in Sample 133-822A-33X-CC, followed by the highest occurrence of *Discoaster brouweri* (1.88 Ma) in Sample 133-822A-36X-CC, then by the highest occurrence of*Discoaster pentaradiatus* (2.29 Ma) in Sample 133-822A-43X-CC. The oldest biohorizon encountered was the highest occurrence of *Discoaster tamalis* (2.6 Ma) in Sample 133-822A-45X-CC. This sample also marks the somewhat younger *Discoaster surculus* highest occurrence (2.42 Ma), but one can reasonably expect that the occurrence of this latter species extends higher upward in Core 133-822A-45X than does *Discoaster tamalis*. No other conventional biohorizons were recovered below this level.

Planktonic Foraminifers

An expanded upper Pliocene–Pleistocene section was drilled at Site 822. Planktonic foraminifers are abundant and well-preserved throughout the entire hole, except for Samples 133-822A-19X-CC, -25X-CC, -43X-CC, and -44X-CC, in which sparse, well-preserved specimens were found. Late Pleistocene markers are present in the top of the section, for example *Bolliella adamsi* (Sample 133-822A-1H-CC) and *Globigerinoides ruber* pink (Samples 133-822A-2H-CC and-3H-CC). The highest occurrence of *Globigerinoides fistulosus* (1.6 Ma) is found in Sample 133-822A-35X-CC. The highest occurrence of *Globigerinoides obliquus* (1.8 Ma) was recorded in the next lower sample, which delimits the lowest Pleistocene. *Globorotalia truncatulinoides* ranges throughout the hole, except for the two lowermost cores: Samples 133-822A-46XCC and -47X-CC. Thus, the boundary between Zones N22–N23 and N21 is found in Core 133-822A-46X, The lowest sample, 133-822A-47X-CC, did not yield *Globoquad-*

rina altispira, which constrains the age of the bottom of the hole to less than 2.9 Ma.

Benthic Foraminifers

Core-catcher samples from Hole 822A contain well-preserved, diverse benthic foraminiferal assemblages that indicate a middle bathyal paleodepth (600–1000 m) for this site. Benthic foraminiferal assemblages examined from Hole 822A contain shallow-water contaminants, such as *Amphistegina* spp., *Buliminella elegantissima, Elphidium* spp., frequent miliolids, and *Planorbulina* spp., indicating that downslope transport of benthic foraminifers took place. Approximately one of every five core-catcher samples was examined for contents of qualitative benthic foraminifers to estimate paleobathymetry.

Hole 822A benthic foraminiferal assemblages contain the typical bathyal species *Bulimina aculeata, Bulimina mexicana, Cibicidoides bradyi, Cibicidoides mundulus, Cibicidoides pachyderma, Eggerella bradyi, Globocassidulina subglobosa, Hanzawaia balthica, Hoeglundina elegans, Lenticulina peregrina, Nuttallides umbonifera*, rare *Planulina wuellerstorfi, Sigmoilopsis schlumbergeri, Sphaeroidina bulloides, Uvigerina hispida, Uvigerina peregrina, Uvigerina pigmaea*, and *Uvigerina proboscidea* (van Morkhoven et al., 1986). Several taxa place an estimated upper depth limit on Hole 822A of the middle bathyal zone or deeper (>600 m), including *Cibicidoides robertsonianus* and *Pyrgo murrhina*. *Hyalinea balthica* restricts the estimated lower depth limit for Hole 822A core-catcher samples to shallower than 1000 m (van Morkhoven et al., 1986).

PALEOMAGNETISM

Operating methods for acquiring paleomagnetism data at Site 822 were similar to those used at previous sites. All core sections were measured continuously in Hole 822A. On the whole, these measurements proved moderately useful for determining preliminary polarities based on inclination directions only. Natural remanent magnetization (NRM) intensity values obtained from pass-through measurements typically are in the range of 0.6 to 1.0 mA/m. However, several intervals (e.g., 3 to 8 mbsf) are characterized by higher intensity values up to 10 mA/m. After alternating field (AF) demagnetization at 15 mT, intensity values decrease to about 0.1 to 0.5 mA/m.

On the whole, inclination data for Hole 822A are of acceptable quality, although perhaps not completely free of magnetic overprinting and other disturbances. In addition, numerous inclination excursions occur as a result of drilling disturbances in XCB cores. Various gaps are present in the inclination record that were caused by discontinuous recovery and our inability to analyze XCB cores because of total drilling disturbance. We used 15-mT inclination directions for interpreting preliminary polarities, which will have to be confirmed and refined in shore-based analyses of about 500 discrete samples from the cored section.

We tentatively identified several major zones of magnetic polarity in Hole 822A (Fig. 14). After shipboard analysis, however, placement of chron and subchron boundaries was still uncertain. The scattered nature of inclination values after AF demagnetization at 15 mT made interpretation tenuous. The Brunhes/Matuyama boundary may be located at either (1) 70 mbsf at the first major inclination reversal, which agrees in general with biostratigraphic markers (see "Biostratigraphy" section, this chapter) or (2) at the base of the next lower normal section, between 95 and 100 mbsf, which disagrees with shipboard biostratigraphy. Alternatively, the normal polarity interval between about 77 and 98 mbsf may represent

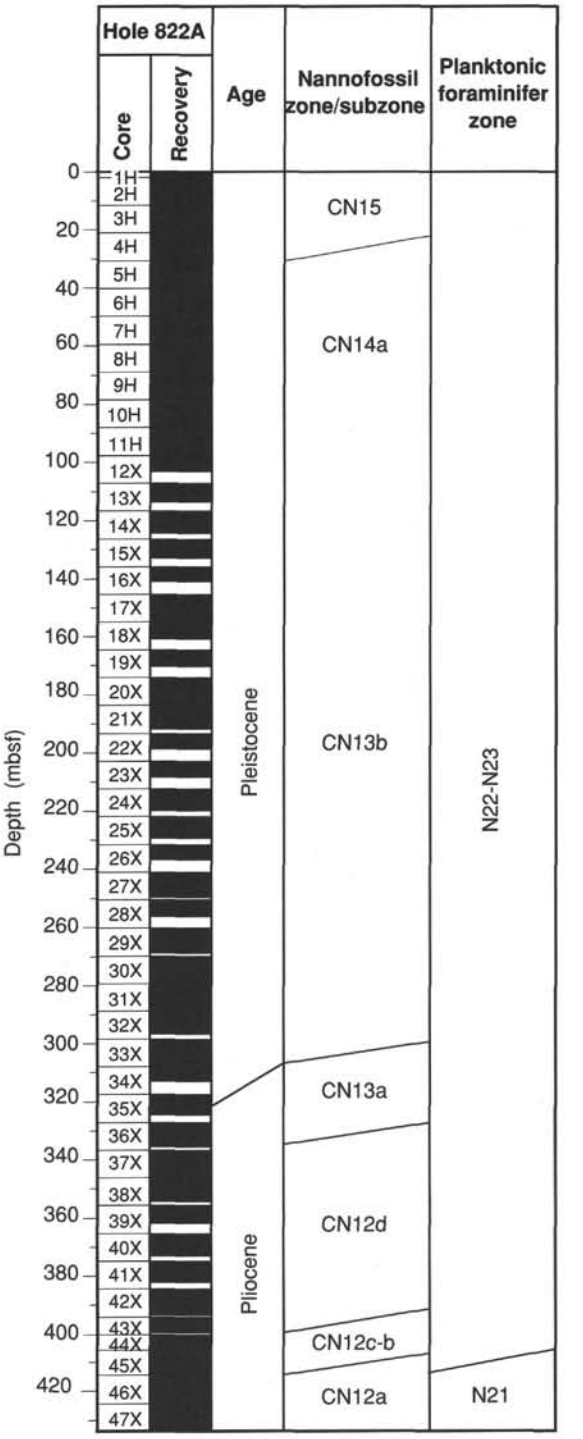

Figure 13. Biostratigraphic overview for Site 822.

the Jaramillo subchron and is consistent with biostratigraphic tie-points. Between about 100 and 145 mbsf, polarity is uncertain and consists of both normal and reversed intervals. A predominantly normal polarity(?) zone occurs from 148 to 159 mbsf, which may perhaps represent an expanded event between the Jaramillo and Olduvai chrons. From 160 to about 335 mbsf, a scattered inclination record indicates dominantly reversed polarity. This thick reversed zone has been tentatively correlated with the upper part of the Matuyama reversed chron.

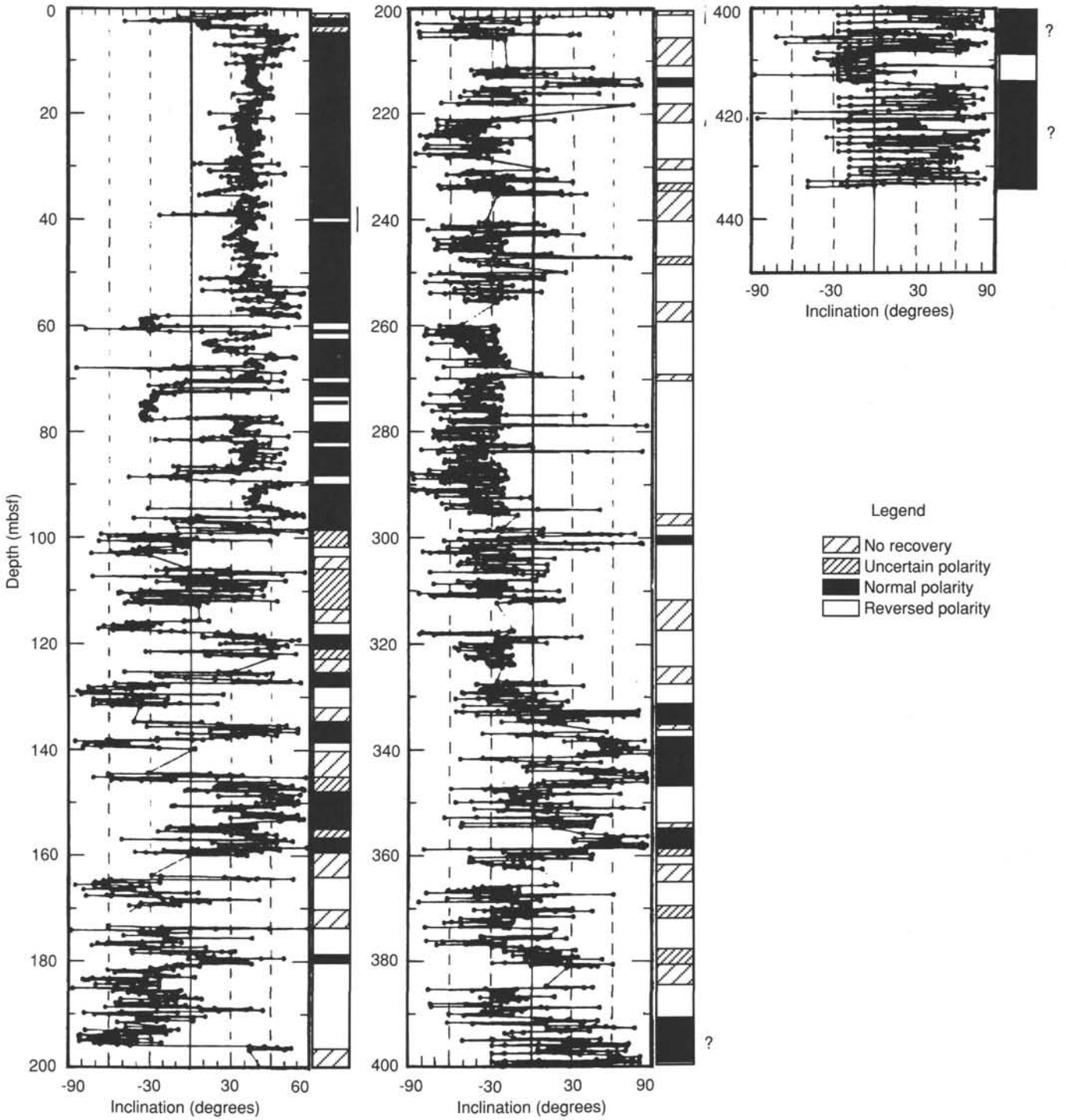

Figure 14. Inclination (after 15-mT AF demagnetization) and polarity zones as a function of depth, recorded in Hole 822A.

From about 330 to 359 mbsf, a normal polarity zone may represent part of the Olduvai normal subchron, which agrees in general with biostratigraphic markers. Below this, a zone of reversed polarity extends to about 390 mbsf, where a poorly defined polarity transition (reversed to normal) occurs. This scattered transition is confused somewhat by what probably is contamination of the sample boat. A zone of normal polarity(?) from 390 to 433 mbsf, interrupted by a reversed polarity interval between 409 and 415 mbsf, was measured near the base of the hole. This lower normal zone tentatively was correlated to the Gauss chron, which ranges in age from 2.48 to 3.48 Ma. Of course, this will have to be confirmed by shore-based analysis.

Whole-core volume magnetic susceptibilities were measured at 10-cm intervals throughout Hole 822A. These susceptibility values were slightly positive and usually range around $6.0 \cong 10^{-6}$ cgs. Values as high as $45 \cong 10^{-6}$ cgs also were observed (Fig. 15). As previously noted for Sites 820 and 821, susceptibility peaks correspond to more terrigenous contents of the sediments. A comparison of magnetic susceptibility vs. carbonate content

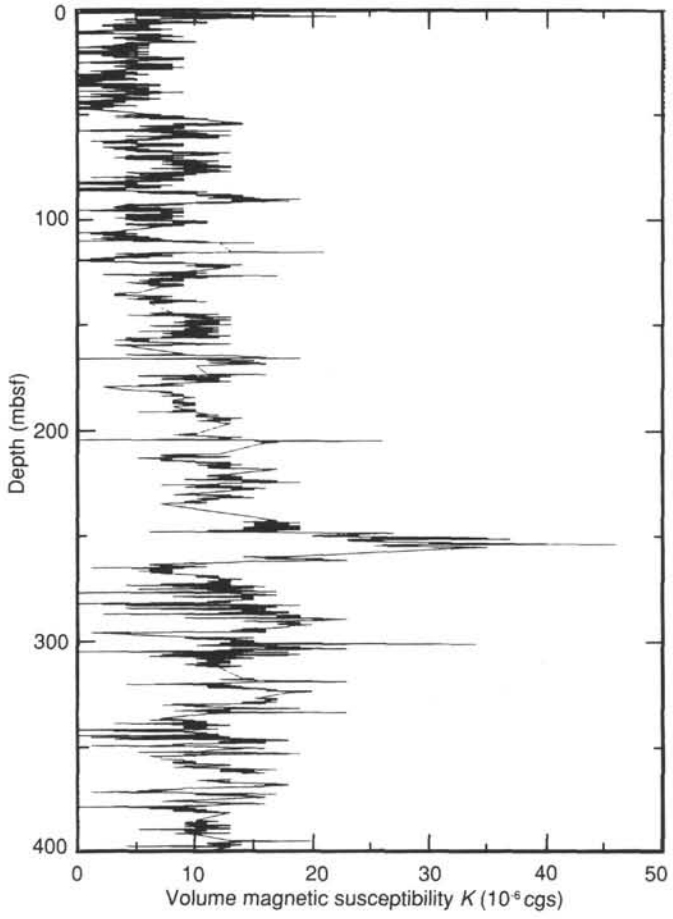

Figure 15. Variations downhole of magnetic susceptibility in Hole 822A.

indicates a strong inverse correlation (Fig. 16), supporting a control of depositional (terrigenous) influx on magnetization in these mixed siliciclastic-carbonate sediments.

SEDIMENTATION RATES

Site 822 yielded an excellent nannofossil biochronology for the entire 434 m of cored section that extended from the Holocene back to the upper Pliocene and spanned more than 2.60 Ma. Figure 17 is an age/depth plot based on nannofossil and planktonic foraminiferal biohorizons, as determined in core-catcher samples. The length of the error bar represents the length of core in which a biohorizon was determined, except for the first point, the *Emiliania huxleyi* lowest occurrence datum, for which the error bar represents the length of the next lower core (because it is a lowest occurrence). In general, sedimentation rates were moderate in the late Pliocene, substantially greater in the early and mid-Pleistocene, then decrease again in the late Pleistocene. When taken biohorizon by biohorizon, these sedimentation rates actually vary greatly over this relatively short time interval. At the very top of the section, from the seafloor to the *Emiliania huxleyi* lowest occurrence (which is taken as the midpoint of the error bar; i.e., 0–24.6 mbsf), the sedimentation rate is 8.9 cm/k.y. One can reasonably assume that a hiatus exists between the *Emiliania huxleyi* lowest occurrence datum and the next lower one, the highest occurrence of *Pseudoemiliania lacunosa* in Sample 133-822A-4H-CC, because these two bioevents are found between adjacent samples in this expanded section. For the early part of the late

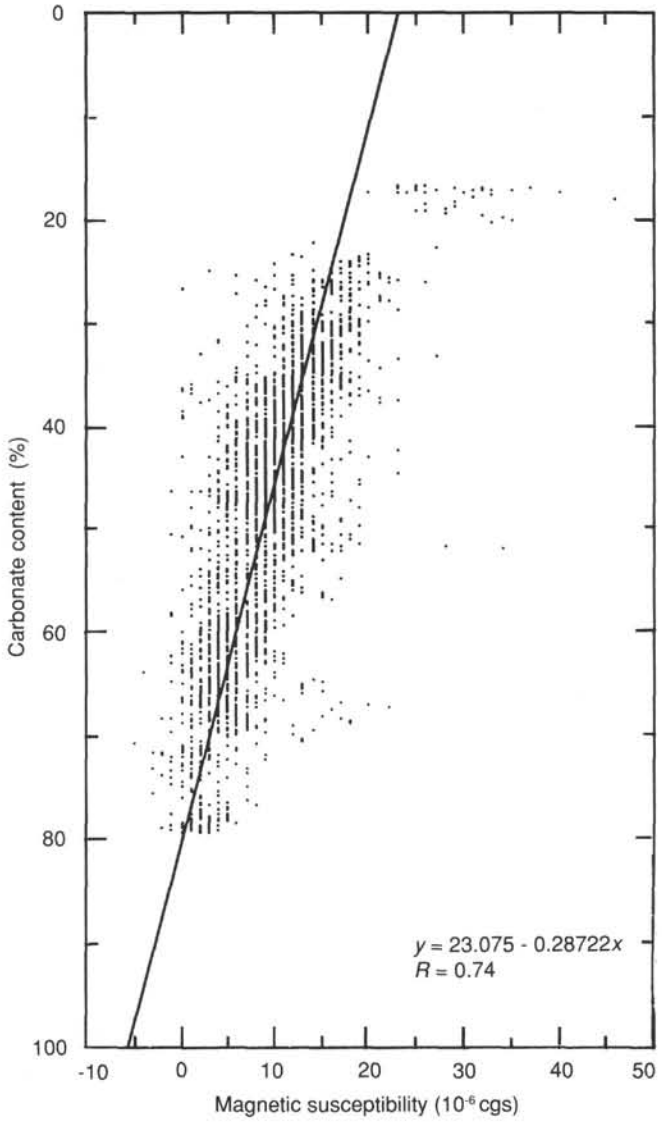

Figure 16. Plot of calcium carbonate contents vs. magnetic susceptibility for Hole 822A. A correlation coefficient of $R = 0.74$ for more than 2300 values supports a significant inverse correlation between susceptibility and carbonate contents of sediments cored in Hole 822A.

Pleistocene, from the upper limit of dominance of small *Gephyrocapsa* at 0.93 Ma to the highest occurrence of *Pseudoemiliania lacunosa* at 0.465 Ma (24.6–81.6 mbsf), sedimentation rates increase to 12.8 cm/k.y. An even sharper increase occurs in the next interval, from the small *Gephyrocapsa* datum to the highest occurrence of *Helicosphaera sellii* at 1.27 Ma (81.6–225.6 mbsf), in which a rate of 42.4 cm/k.y. is seen, and rates are slightly lower (36.8 cm/k.y.) immediately below to the *Calcidiscus tropicus* highest occurrence at 1.48 Ma (225.6–302.9 mbsf). Below this, rates decrease again: 7.2 cm/k.y. to the highest occurrence of *Discoaster brouweri* at 1.88 Ma (302.9–331.8 mbsf); 16.0 cm/k.y. to the highest occurrence of *Discoaster pentaradiatus* at 2.29 Ma (331.8–400 mbsf); and 4.0 cm/k.y. from there to the highest occurrence of *Discoaster tamalis* at 2.6 Ma (331.8–409.7 mbsf).

We determined only two planktonic foraminifer biohorizons for this site; these plot very near where they should be predicted from calcareous nannofossil biohorizons.

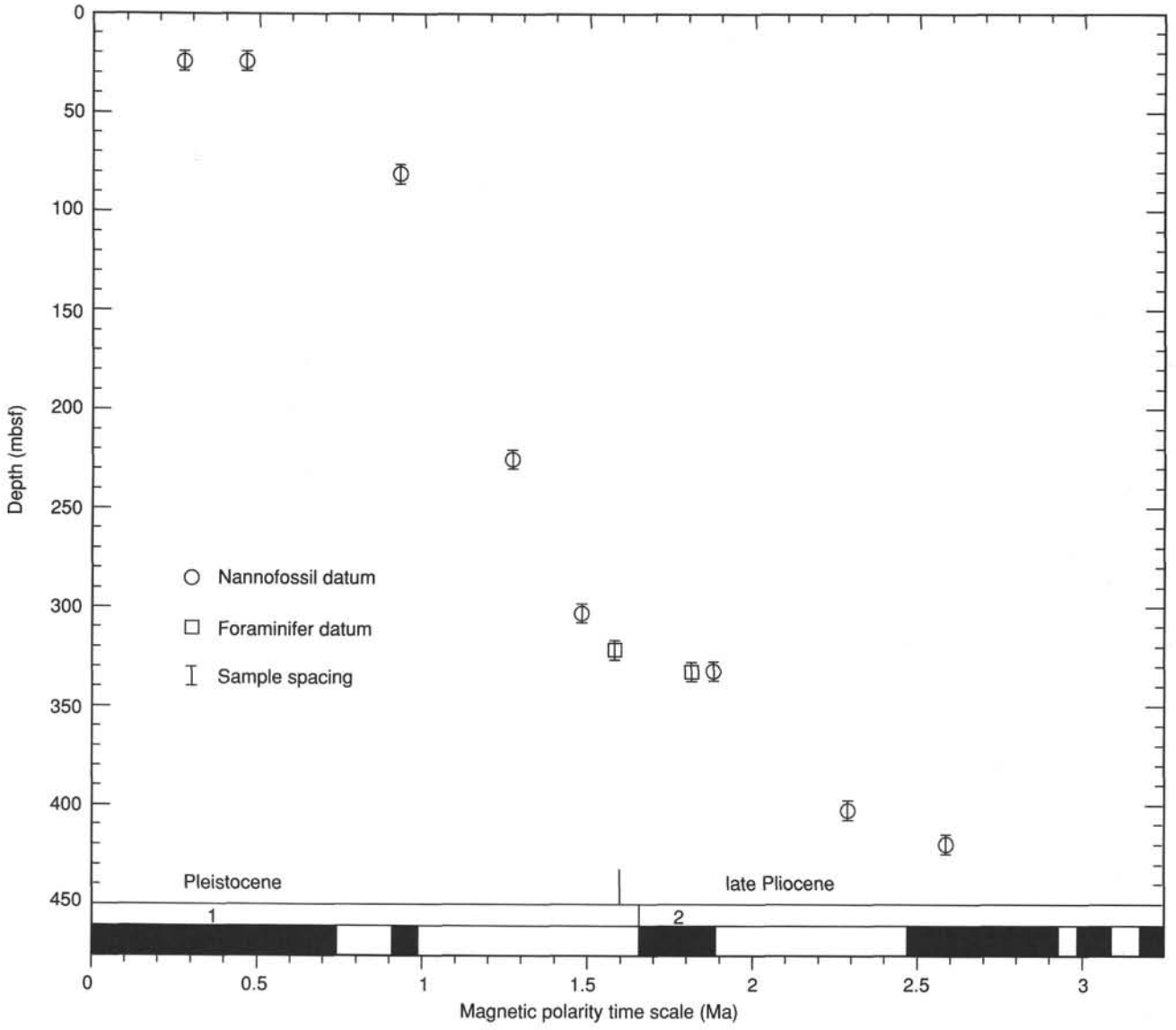

Figure 17. Plot of depth vs. age for Site 822.

INORGANIC GEOCHEMISTRY

Interstitial Waters

Interstitial water samples were taken from Cores 133-822A-2H to -11H and from 133-822A-14H, -17V, -20X, -23X, -27X, -29X, -32X, -35X, -38X, -41X, -44X, and -47X. In addition, the "Barnes" downhole water sampler (WSTP) was deployed before Cores 133-822A-12H, -18X, -23X, -28X, -33X, and -38X. Samples were squeezed and analyzed according to methods outlined in the "Explanatory Notes" chapter (this volume).

Calcium, Magnesium, Potassium, and Strontium

Concentrations of Ca^{2+}, Mg^{2+}, and K^+ all decrease from seawater values (10.54, 54.61, and 12.03 mM, respectively) within the top 100 mbsf to nearly constant values of 4, 20, and 4 mM, respectively, for the rest of the sampled interval (Fig. 18 and Table 2).

Concentrations of strontium in pore waters decreased slightly from surface-water values of 102 μM to 83 μM at 8.4 mbsf. Below this depth, values increase to 161 μM at 36.8 mbsf, where they remain constant until 294.3 mbsf; concentrations then increase to 290 μM at the bottom of the sampled interval (Fig. 18 and Table 2). The small increase in interstitial-water Sr^{2+}, when compared with that at other sites in this transect (819, 820, and 821), indicates that carbonate recrystallization is low at Site 822.

When concentrations were normalized to the value for surface-water chloride, an average loss of 6.43 mM of Ca^{2+} and 36.54 mM of Mg^{2+} took place (Fig. 19). Calcium probably has been used to form authigenic calcite, whereas magnesium was consumed during the formation of dolomite. Potassium also might be depleting in pore waters, with a net loss of 8.92 mM (Fig. 19). The loss concentrations of K^+ and Mg^{2+} may be the result of uptake into clays.

Chloride

Concentrations of chloride average slightly below that of seawater (545.80 mM) for the top 177.7 mbsf of the cored interval (Fig. 18 and Table 2). Below this depth, concentrations increase to 550.61 mM at the bottom of the hole. The

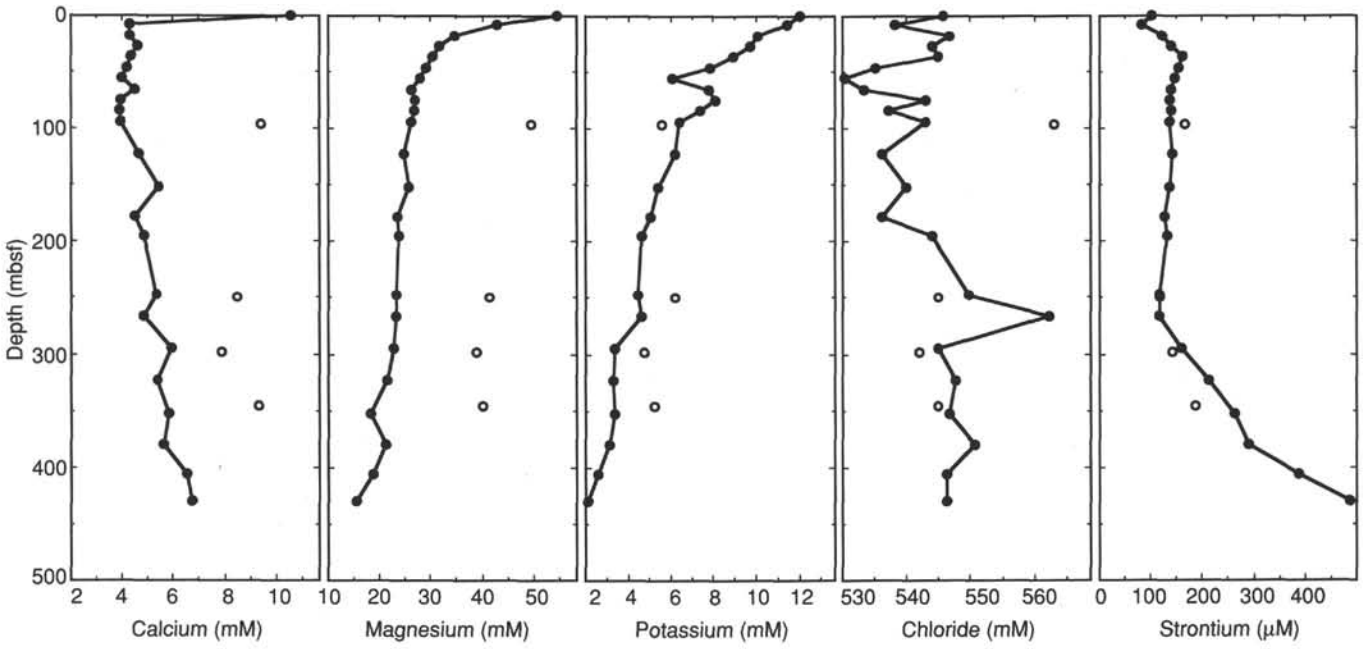

Figure 18. Calcium, magnesium, strontium, potassium, and chloride data as a function of depth for Site 822. Open circles indicate data from WSTP samples.

Table 2. Interstitial water data for Site 822.

Core, section, interval (cm)	Depth (mbsf)	pH	Alkalinity (mM)	Salinity (g/kg)	Calcium (mM)	Magnesium (mM)	Chloride (mM)	Silica (μM)	Strontium (μM)	Sulfate (mM)	Ammonia (μM)	Potassium (mM)	Phosphate (μM)
Seawater	0	8.20	2.750	35.0	10.54	54.61	545.80	2	102	28.54	89	12.03	1
133-822A-													
2H-5, 145–150	8.4	7.58	9.862	33.0	4.28	42.94	538.12	302	83	10.54	921	11.43	7
3H-5, 140–150	17.8	7.55	13.828	32.5	4.27	34.64	546.76	381	123	0.00	929	10.04	4
4H-5, 140–150	27.3	7.63	12.057	32.0	4.61	31.57	543.88	331	140	0.00	1396	9.70	3
5H-5, 140–150	36.8	7.32	11.822	32.0	4.35	30.31	544.84	436	161	0.00	1786	8.95	2
6H-5, 140–150	46.3	7.52	10.469	32.0	4.19	29.26	535.23	267	154	0.00	1956	7.83	2
7H-5, 140–150	55.8	7.46	10.910	32.0	3.99	27.89	530.43	222	146	0.00	2126	6.04	3
8H-5, 140–150	65.3	7.45	8.561	31.0	4.48	26.22	533.31	263	140	0.00	2240	7.77	1
9H-5, 140–150	74.8	7.72	9.270	31.8	3.96	26.83	542.92	202	138	0.00	2588	8.08	2
10H-5, 140–150	84.3	7.12	9.092	31.8	3.88	26.59	537.15	206	140	0.00	2742	7.37	2
11H-5, 140–150	93.8	7.62	9.498	31.5	3.95	26.05	542.92	210	137	0.00	2814	6.40	2
12H-10-7	95.9	7.70	3.571	35.0	9.39	49.48	563.10	159	166	26.88	2368	5.60	2
14H-5, 140–150	122.8	7.68	10.575	32.0	4.62	24.72	536.19	218	142	0.00	3174	6.16	2
17X-5, 140–150	151.7	7.47	10.686	32.0	5.41	25.69	540.04	255	136	1.24	3191	5.41	2
18X-10-7	154.0	8.12	5.981	34.0									2
20X-3, 140–150	177.7	7.73	8.703	31.0	4.49	23.51	536.19	171	126	0.00	3195	5.06	2
23X-10-7	192.2	8.70	8.093	35.0									2
23X-2, 140–150	195.1	7.69	8.347	31.8	4.84	23.72	543.88	231	132	0.00	2953	4.64	2
27X-5, 140–150	247.6	7.86	8.571	31.2	5.31	23.18	549.65	224	118	1.02	2784	4.44	2
28X-10-7	249.8	8.72	6.904	34.0	8.47	41.25	544.84	88	118	19.77	2372	6.16	2
29X-5, 140–150	266.9	7.83	7.049	32.2	4.85	23.27	562.14	139	116	2.36	3094	4.64	2
32X-4, 140–150	294.3	7.82	8.388	31.5	5.94	22.74	544.84	235	158	1.12	2453	3.38	2
33X-10-7	298.1	8.32	7.282	34.0	7.86	38.81	541.96	182	143	12.78	2482	4.73	10
35X-4, 140–150	323.4	7.70	5.941	31.5	5.40	21.35	547.72	167	214	0.64	2797	3.32	2
38X-10-7	346.3	8.27	4.178	34.0	9.29	40.09	544.84	143	187	21.47	1998	5.20	2
38X-4, 140–150	352.2	7.82	4.846	31.5	5.83	18.10	546.76	192	264	1.48	2614	3.37	2
41X-3, 140–150	379.5	7.69	5.769	31.8	5.65	21.22	550.61	121	290	3.45	2449	3.14	2
44X-4, 140–150	405.9	7.85	5.050	31.8	6.54	18.72	546.36	204	388	0.34	2559	2.62	
47X-4, 140–150	430.2	7.90	4.215	31.8	6.73	15.42	546.36	216	487	0.95	2740	2.10	

relationship between salinity and chlorinity is not conservative at this site (Fig. 20). Most samples are depleted in salinity relative to their chloride concentration; therefore, salinity is being reduced by diagenetic reactions within the sediments that involve the removal of Ca^{2+}, Mg^{2+}, HCO_3, and from pore fluids as authigenic precipitates.

Alkalinity, Ammonia, Phosphate, and Sulfate

Concentrations of alkalinity, NH_4^+, PO_4^{3-}, and SO_4^{2-} at Site 822 shave been affected by SO_4^{2-} reduction of organic matter in the sediments. Alkalinity values rapidly increase from a seawater value of 2.75 to 13.83 mM at 17.8 mbsf (Fig. 21 and

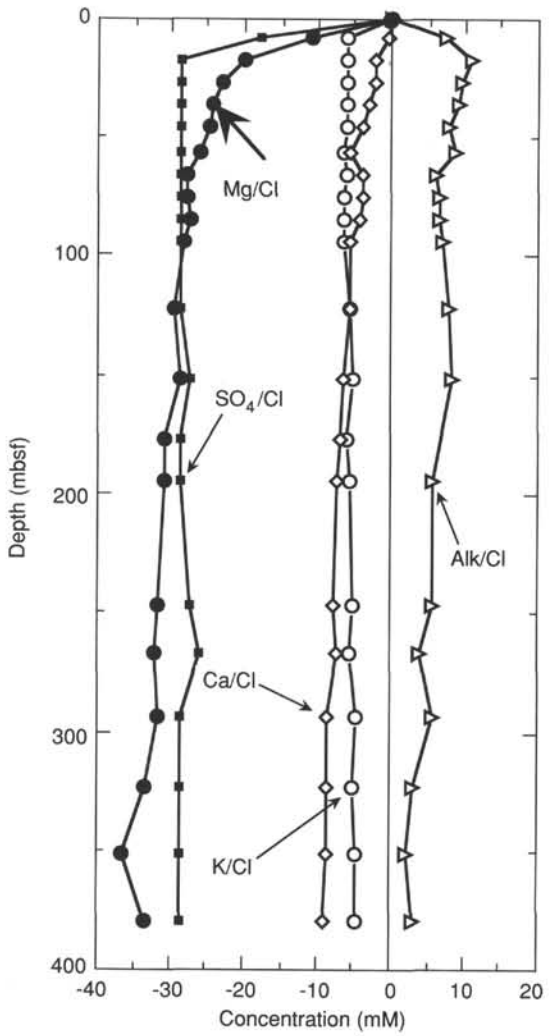

Figure 19. Concentrations of calcium, magnesium, alkalinity, potassium, and sulfate adjusted to surface-water salinity as a function of depth for Site 822.

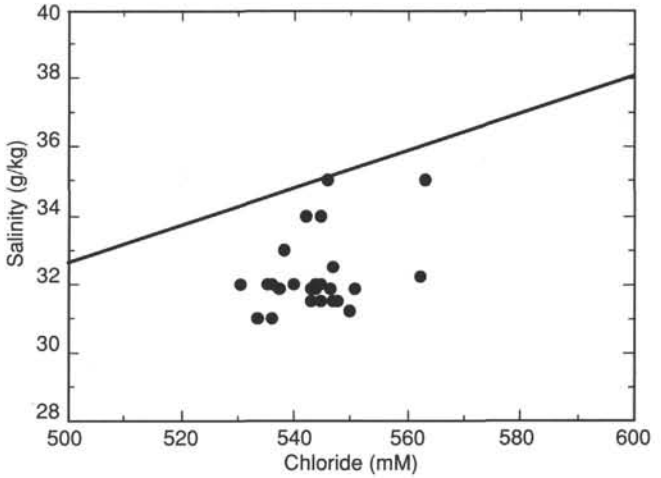

Figure 20. Concentrations of salinity vs. chloride for Site 822. Line in graph is that of conservative relationship between salinity and chlorinity.

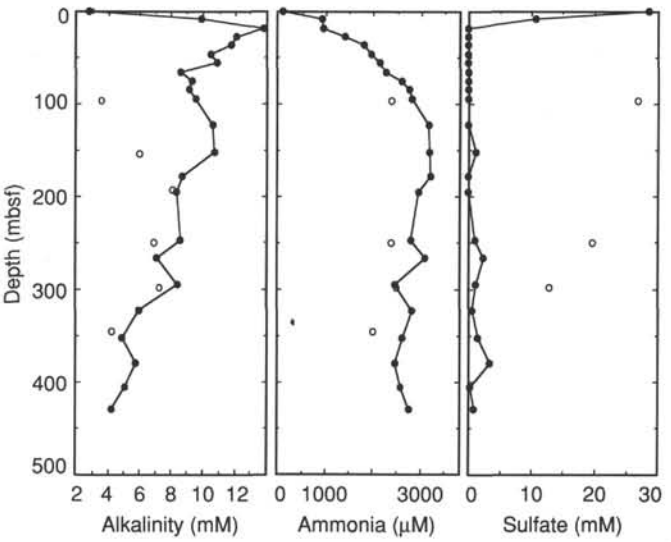

Figure 21. Alkalinity, ammonia, and sulfate data as a function of depth for Site 822. Open circles are WSTP data.

Table 2). Below this maximum, alkalinity values decrease to 4.85 mM at the bottom of the sampled interval. High alkalinity values occur at the same depth where SO_4^{2-} decreases to zero from a seawater value of 28.54 mM. Below 17.8 mbsf, no SO_4^{2-} is present for the rest of the sampled interval because all of it has been consumed during oxidation of the organic matter. Concentrations of ammonia increase from a seawater value of 89 to approximately 2600 μM and then remain nearly constant below 84.3 mbsf (Fig. 21 and Table 2). Concentrations of phosphate increase in the first sample from a seawater value of 1 to 7 μM. Below 17.8 mbsf, the PO_4^{3-} values remain nearly constant at approximately 2 μM for the remainder of the sampled interval (Table 2). From the stoichiometry of the sulfate-reduction reaction, we expected higher concentrations of PO_4^{3-} than we measured, indicating that PO_4^{3-} is being taken up into clays or has been consumed by the sediments as precipitation of amorphous apatite.

Silica

Concentrations of silica were low at Site 822 because of the absence of siliceous microfossils in the sediments. Concentrations did increase from surface-water values of 2 to 436 μM at 36.8 mbsf. Below 36.8 mbsf, concentrations decrease to 200 μM for the rest of the sampled interval (Fig. 22 and Table 2).

Results From WSTP Samples

Because of the degree of induration of sediments at Site 822, we were unable to penetrate these sediments successfully with the WSTP tool to acquire representative water samples. As a result, all of the WSTP samples have been contaminated with seawater and do not accurately reflect variations in interstitial water chemistry shown by squeezed samples (Figs. 18, 22, and 21).

Carbonate Content and X-Ray Diffraction Data

Samples for X-ray diffraction (XRD) analyses were taken from interstitial-water squeeze cakes and physical properties samples.

Sediments at Site 822 are predominantly calcite and aragonite with concentrations of 9.5% to 61.3% and 18.7% to 83.1%, respectively (Fig. 23 and Table 3). High-Mg calcite (HMC) is present in the top 300 mbsf of Site 822 in concentrations up to

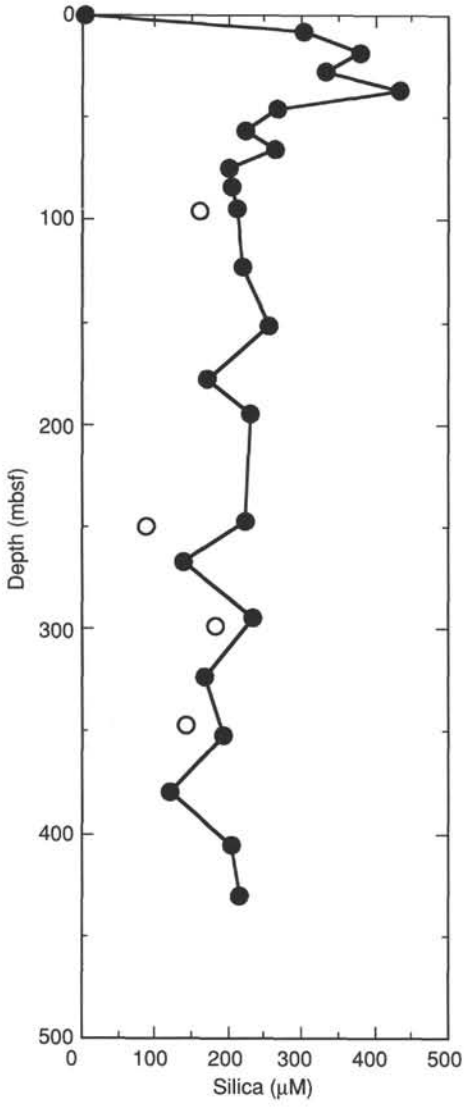

Figure 22. Silica contents of interstitial waters as a function of depth at Site 822. Open circles are WSTP data.

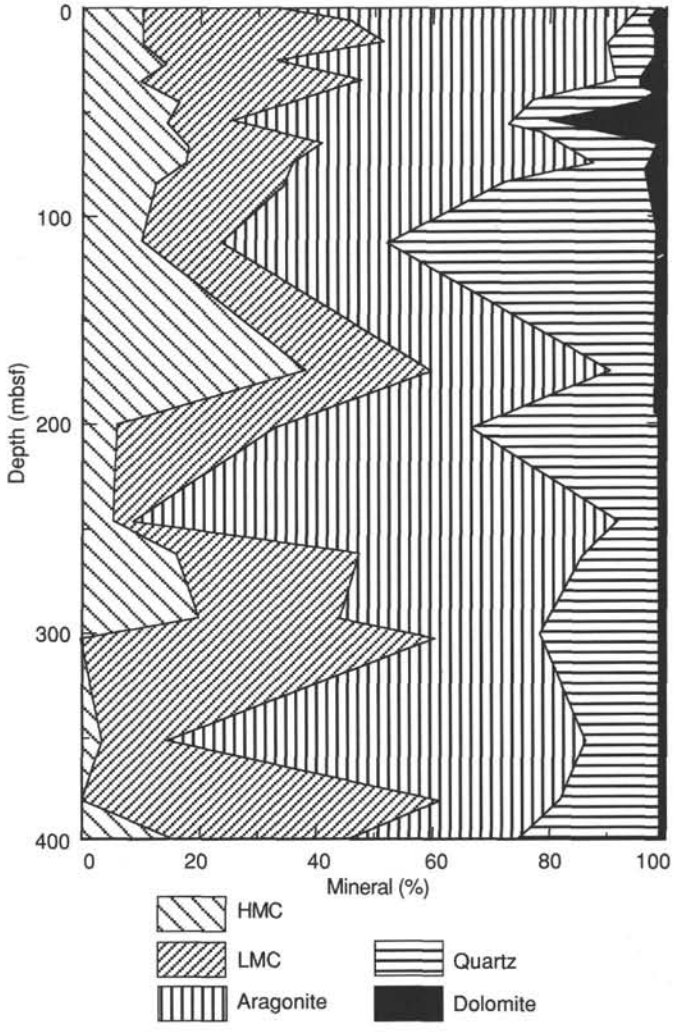

Figure 23. X-ray diffraction data for Site 822. We have assumed that sediments are composed entirely of calcite, aragonite, quartz, and dolomite.

30%. Below 300 mbsf, HMC concentrations decrease to nearly zero and increase at 430 mbsf to 15%. Dolomite is present in the top 157.2 mbsf with concentrations of 0.5% to 18.2%. Below 157.2 mbsf, dolomite is absent (Fig. 23 and Table 3). Detrital quartz is present within the entire sampled interval. Concentrations range from 1.3% to 47.3% and are generally higher below 68.8 mbsf (Fig. 23 and Table 3).

When mineral concentrations were calculated as percentages of quartz, carbonate and clay, we could see that clay concentrations increased with increasing depth, whereas quartz remained relatively constant, with the exception of high concentrations between 75 and 175 mbsf (Fig. 24 and Table 4).

Values of calcium carbonate range from 18% to 80% (Fig. 12 and Table 4) and are highly variable. Using a running average for every five points, distinct trends of cyclic variations in carbonate contents were seen (Fig. 12). These variations result from dilution of the carbonate fraction of the sediments by varying amounts of terrigenous influxes.

Summary

Sites 822, 819, 820, and 821 form a distal-to-proximal slope transect off the eastern margin of the Queensland continental

Table 3. X-ray diffraction data for Site 822.

Core, section, interval (cm)	Depth (mbsf)	Calcite (%)	Aragonite (%)	Quartz (%)	Dolomite (%)
133-822A-					
2H-4, 145–150	8.4	34.3	59.2	6.5	0.0
3H-5, 145–150	17.8	46.8	46.9	5.3	1.0
4H-5, 145–150	27.3	50.9	41.0	8.1	0.0
5H-5, 145–150	36.8	34.1	58.7	7.2	0.0
6H-5, 145–150	46.3	48.1	44.2	4.8	2.9
7H-5, 145–150	55.8	37.4	40.6	22.0	0.0
8H-5, 145–150	65.3	26.4	47.8	7.6	18.2
9H-5, 140–150	73.9	41.0	41.7	17.3	0.0
10H-5, 140–150	83.5	37.2	51.3	10.1	1.3
14X-5, 140–150	121.3	35.3	39.0	23.9	1.8
17X-5, 140–150	151.7	24.4	28.3	47.3	0.0
20X-3, 140–150	177.7	59.7	31.7	8.1	0.5
23X-2, 140–150	204.4	34.0	33.9	32.1	0.0
27X-5, 140–150	247.1	9.5	83.1	7.4	0.0
29X-3, 140–150	265.7	48.0	38.4	13.6	0.0
32X-4, 140–150	294.3	44.7	35.4	19.9	0.0
35X-4, 140–150	323.4	60.5	18.7	20.8	0.0
38X-4, 140–150	352.2	15.0	72.3	12.6	0.0
41X-3, 140–150	378.8	61.3	21.1	17.7	0.0
44X-4, 140–150	405.5	33.4	29.5	0.0	
47X-5, 140–150	430.2	28.2	29.5	1.3	

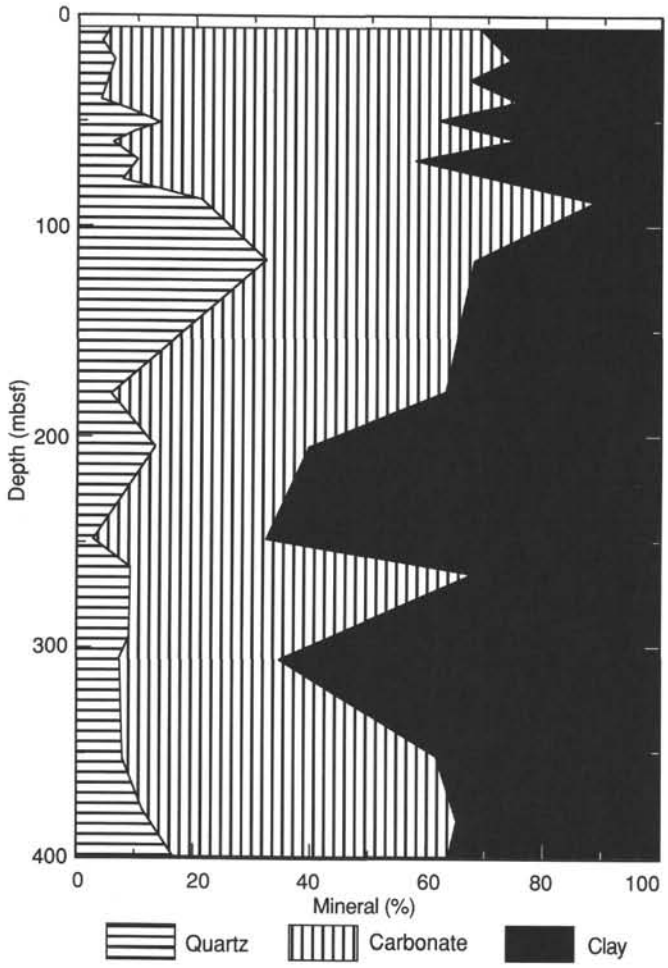

Figure 24. Mineralogy data for Site 822. We have assumed that sediments are composed entirely of carbonate, clay, and quartz.

shelf. Sediments are composed primarily of mixtures of metastable carbonate minerals, such as aragonite and high-Mg calcite that derived from the Great Barrier Reef and quartz, feldspars, and clay minerals that eroded from the Australian mainland (Fig. 11). The concentrations of clay minerals increase with distance from the continental shelf and reach more than 50% of the sediments at Sites 819, 822, and 821 (Fig. 10). Quartz makes up between 10% and 20% of the sediments at each site, and a slight tendency exists for the proximal sites to contain higher concentrations. In general, profiles of carbonate content along the transect reflect variations in dilution of carbonate by influxes of terrigenous sediments from the continent (Figs. 25 and 26). The peaks of the carbonate curves that correlate among sites most likely result from large-scale variations in terrigenous influxes that occur during variations in sea level. Portions of these carbonate-content curves that do not correlate with each other may be the result of localized deposition, as might occur from turbidites or the occurrence of a hiatus.

When viewing trends of carbonate data along the transect (Fig. 26), we can see that despite a large amount of variation, even in smoothed data, profiles for Sites 821, 820, and 819 correlate reasonably well, while most peaks correlate among all three sites, and an overall trend of increasing carbonate content occurs in the 0.465- to 1.27-Ma interval, then decreasing after 1.27 Ma. In contrast, Site 822 has a decreasing carbonate content with increasing depth, with a slight increase in carbonate content for sediments older than 1.48 Ma. In addition, amplitude of the fluctuations of carbonate is less than at the other three sites. Despite these differences, carbonate peaks at Site 822 still correlate well with those at the other sites in the transect. One possible explanation is that sediments distal from the continent at Site 822 are receiving less influx of carbonate. Both factors should reduce the amplitude of the fluctuations in carbonate content data.

Rapid rates of sedimentation at these sites (100–200 m/m.y.) have resulted in the burial of abundant organic material, which subsequently was oxidized by sulfate-reducing bacteria to produce H_2S and CO_2. As the types and amounts of minerals and organic material vary with distance from the shelf, the nature and magnitude of the diagenetic reactions occurring in the sediment also change, producing distinctive differences in the profiles of interstitial minor elements at the four sites.

The most dramatic change visible at all sites is the removal of sulfate during oxidation of organic material. Although complete sulfate reduction occurs at all sites, the process takes place as shallow as 25 mbsf at Sites 822 and 819, while at Site 821, sulfate is not completely exhausted until 144.5 mbsf (Fig. 27). As Sites 819 to 822 experienced approximately similar rates of sedimentation and do not exhibit significant differences in their physical properties (porosity, density, formation factor), the most plausible explanation for the different depths of sulfate reduction lies in the different amounts and types of organic material present at each site. Sites 819 and 822 initially must have contained higher concentrations of organic matter or material that was more easily degraded than that at Sites 821 and 820. This initial difference is reflected in the present-day content of organic material at these sites, which increases with increasing distance from the continental shelf. A further possibility is that as organic material at Sites 819 and 822 is predominantly of marine, rather than terrestrial, origin, it is more easily degraded by sulfate-reducing bacteria. Such a difference should promote higher rates of sulfate reduction at the distal sites. Differences in the rate of sulfate reduction are partially reflected in differences in alkalinity, with highest values occurring at Sites 819 and 822 (Fig. 27). However, the increase in alkalinity at these sites is significantly less than that one might expect as a result of sulfate reduction alone. The alkalinity deficit can be explained by (1) the precipitation of dolomite and calcite, (2) diagenesis of clay minerals, or (3) loss of H_2S during precipitation of pyrite. Confirmation of these processes can be observed in the gradients of Ca^{2+}, Mg^{2+}, K^+, and Sr^{2+}, the magnitude of which varies as a function of distance from the reef margin (Figs. 28 and 29). At Site 821, concentrations of interstitial K^+, Mg^{2+}, and Ca^{2+} decrease by 8, 50, and 8 mM, respectively. These decreases become progressively less at Sites 820, 819, and 822. Accompanying these changes in pore-water chemistry is an increase in concentrations of dolomite from the distal to proximal sites. Thus, the sites having the greatest degree of sulfate reduction and the highest alkalinity have the lowest concentration of dolomite. Such a distribution is contrary to current dogma about the formation of dolomite, which suggests that dolomitization should be favored by high concentrations of alkalinity and low amounts of sulfate (Baker and Kastner, 1981). One possible explanation is that the dolomite formed at some time in the past 1 to 1.5 m.y, at which time alkalinity was higher and sulfate lower than at present. Dolomitization might have been promoted through the dissolution of HMC, which together with ambient pore-water Mg^{2+} provided sufficient Mg^{2+} for the formation of dolomite. Such a hypothesis is supported by various proofs and evidence. First, dolomite may be most abundant in those portions of Sites 819, 820, and 821 that lack HMC. Although this might be a coincidence, the implication is that HMC in these sediments dissolved to provide sufficient Mg^{2+} for the

Table 4. Carbonate data for Site 822.

Core, section, interval (cm)	Depth (mbsf)	Carbon (%)	Carbonate (%)
133-822A-			
2H-1, 97–99	1.87	8.58	71.50
2H-3, 97–99	4.87	7.64	63.60
2H-5, 97–99	7.87	7.29	60.70
2H-5, 145–150	8.35	8.54	66.60
3H-1, 22–25	10.62	8.40	70.00
3H-3, 22–25	13.62	6.57	54.70
3H-5, 22–25	16.62	7.82	65.10
3H-5, 140–150	17.80	8.30	67.30
3H-7, 22–25	19.62	6.43	53.60
4H-1, 23–25	20.13	7.78	64.80
4H-3, 23–25	23.13	6.91	57.60
4H-5, 23–25	26.13	7.50	62.50
4H-5, 140–150	27.30	8.33	68.30
4H-7, 23–25	29.13	9.45	78.70
5H-1, 16–19	29.56	9.29	77.40
5H-3, 16–19	32.56	9.52	79.30
5H-5, 16–19	35.56	8.56	71.30
5H-5, 140–150	36.80	8.00	62.00
5H-7, 16–19	38.56	7.14	59.50
6H-1, 20–23	39.10	7.34	61.10
6H-3, 20–23	42.10	8.06	67.10
6H-5, 20–23	45.10	8.92	74.30
6H-5, 140–150	46.30	8.78	71.30
7H-1, 20–23	48.60	8.64	72.00
7H-3, 20–23	51.60	7.78	64.80
7H-5, 20–23	54.60	3.07	25.60
7H-5, 140–150	55.80	5.94	47.60
7H-7, 20–23	57.60	5.56	46.30
8H-1, 20–23	58.10	5.56	46.30
8H-3, 20–23	61.10	5.26	43.80
8H-5, 20–23	64.10	8.18	68.10
8H-5, 140–150	65.30	8.71	69.60
8H-7, 20–23	67.10	7.02	58.50
9H-1, 20–23	67.60	5.67	47.20
9H-3, 20–23	69.69	6.19	51.60
9H-5, 20–23	72.69	4.23	35.20
9H-5, 140–150	73.89	6.06	47.60
9H-7, 20–23	75.69	5.24	43.60
10H-1, 20–23	77.10	5.25	43.70
10H-3, 20–23	79.30	5.07	42.20
10H-5, 20–23	82.30	7.99	66.60
10H-5, 140–150	83.50	8.25	65.90
10H-7, 20–23	85.30	7.98	66.50
11H-1, 19–20	86.59	5.58	46.50
11H-3, 19–20	89.59	3.04	25.30
11H-5, 19–20	92.59	6.55	54.60
11H-5, 140–150	93.80	8.40	67.80
11H-7, 19–20	95.59	6.98	58.10
12X-1, 28–31	96.18	5.84	48.60
12X-3, 21–24	99.11	5.91	46.60
12X-5, 21–24	102.11	5.75	47.90
13X-1, 20–23	105.90	8.26	68.80
13X-3, 16–17	108.86	8.34	66.70
13X-5, 21–24	111.51	6.50	54.10
14X-1, 21–23	115.61	4.10	34.20
14X-3, 21–23	118.61	8.18	68.10
14X-4, 140–150	121.30	5.38	41.70
14X-5, 21–23	121.61	2.61	21.70
15X-1, 13–15	125.13	7.89	65.70
15X-3, 20–23	128.20	4.61	34.50
15X-5, 20–23	131.20	4.91	40.90
16X-1, 46–49	135.06	6.65	55.40
16X-3, 20–23	137.80	6.85	54.40
17X-1, 14–17	144.44	4.90	40.80
17X-3, 14–17	147.44	4.64	38.70
17X-5, 14–17	150.44	4.25	35.40
17X-5, 140–150	151.70	4.78	35.90
18X-1, 17–18	154.17	4.72	39.30
18X-3, 5–7	157.05	7.60	59.70
19X-1, 28–30	163.98	5.47	45.60
19X-3, 5–6	166.75	4.40	33.20
20X-1, 5–7	173.35	4.63	38.60
20X-3, 5–7	176.35	5.24	43.60
20X-3, 140–150	177.70	7.37	57.60
20X-5, 5–7	179.35	7.79	64.90
21X-1, 18–19	182.78	4.71	39.20
21X-3, 8–9	185.68	6.25	48.50
21X-5, 8–9	188.68	5.71	47.60
23X-1, 8–9	201.58	5.12	42.60
23X-2, 140–150	204.40	3.54	26.90
23X-3, 8–9	204.58	3.11	25.90

Table 4 (continued).

Core, section, interval (cm)	Depth (mbsf)	Carbon (%)	Carbonate (%)
24X-1, 5–7	211.25	3.25	27.10
24X-3, 5–7	214.25	6.14	46.30
24X-5, 5–7	217.25	4.50	37.50
25X-1, 6–8	220.96	3.95	32.90
25X-3, 6–8	223.96	4.08	29.50
25X-5, 6–8	226.96	5.01	41.70
26X-1, 23–26	230.73	4.29	35.70
26X-3, 6–9	233.56	5.82	45.60
27X-1, 4–6	240.24	3.27	27.20
27X-3, 4–6	242.78	3.75	31.20
27X-5, 4–6	245.78	3.62	30.20
27X-5, 140–150	247.14	3.85	29.60
28X-1, 4–6	249.84	2.10	17.50
28X-3, 4–6	252.84	2.17	16.60
29X-3, 15–17	261.49	3.36	28.00
29X-5, 15–17	264.49	6.21	51.70
29X-5, 140–150	265.74	7.49	58.40
29X-7, 15–17	267.49	7.37	61.40
30X-1, 15–17	269.25	5.64	47.00
30X-3, 13–15	272.23	4.80	34.90
30X-5, 13–15	275.23	4.67	38.90
30X-7, 13–15	278.23	4.18	34.80
31X-1, 45–47	279.25	4.18	34.80
31X-3, 45–47	281.31	5.49	41.30
31X-5, 45–47	284.31	3.80	31.70
31X-7, 45–47	287.31	3.97	33.10
32X-1, 19–21	288.59	3.22	26.80
32X-3, 19–21	291.59	2.86	23.80
32X-4, 140–150	294.30	4.48	33.90
32X-5, 19–21	294.59	3.66	30.50
33X-1, 19–21	298.29	5.71	47.60
33X-3, 23–25	301.33	6.64	52.10
33X-5, 19–21	304.29	5.01	41.70
33X-7, 19–21	307.29	3.10	25.80
34X-1, 20–23	308.00	4.14	34.50
33X-3, 20–23	311.00	4.91	37.90
35X-1, 33–36	317.83	4.10	34.20
35X-3, 33–36	320.83	5.07	42.20
35X-4, 140–150	323.40	3.67	27.20
35X-5, 33–36	323.83	2.83	23.60
36X-1, 23–24	327.23	3.19	26.60
36X-3, 23–24	330.23	7.40	59.60
36X-5, 23–24	333.23	5.01	41.70
37X-1, 20–22	336.80	5.61	46.70
37X-3, 20–22	339.16	5.75	44.60
37X-5, 20–22	342.16	7.37	61.40
37X-7, 20–22	345.16	4.82	40.20
38X-1, 21–23	346.51	2.84	23.70
38X-3, 21–23	349.51	5.99	49.90
38X-4, 140–150	352.20	6.70	53.60
38X-5, 21–23	352.51	6.38	53.10
39X-1, 21–23	356.11	5.17	43.10
39X-3, 21–23	359.11	5.40	40.80
39X-5, 21–23	362.11	3.83	31.90
40X-1, 20–23	365.70	4.78	39.80
40X-3, 20–23	368.70	4.31	33.50
40X-5, 20–23	371.70	6.47	53.90
41X-1, 4–7	375.14	7.05	58.70
41X-3, 4–7	377.46	4.61	38.40
41X-3, 140–150	378.82	6.68	53.40
41X-5, 4–7	380.46	5.88	49.00
42X-1, 4–7	384.84	5.94	49.50
42X-3, 4–7	387.84	5.75	45.80
42X-5, 4–7	390.84	5.03	41.90
43X-1, 5–7	394.55	3.38	28.20
43X-3, 5–7	397.55	4.23	32.20
44X-1, 20–21	400.20	3.99	33.20
44X-3, 20–21	403.20	3.86	32.20
45X-1, 20–22	405.10	4.31	35.90
44X-4, 140–150	405.90	4.48	34.70
44X-5, 20–21	406.20	5.30	44.10
45X-3, 20–22	407.83	6.29	50.50
45X-5, 20–22	410.83	3.89	32.40
45X-7, 20–22	413.83	4.45	37.10
46X-1, 20–22	414.80	4.31	35.90
46X-3, 20–22	417.42	5.49	43.10
46X-5, 20–22	420.42	4.70	39.20
47X-1, 7–9	424.37	4.30	35.80
47X-3, 13–14	427.43	6.31	52.60
47X-4, 140–150	430.20	5.28	40.70
47X-5, 20–21	430.50	4.70	39.20
47X-7, 18–19	433.21	4.28	35.70

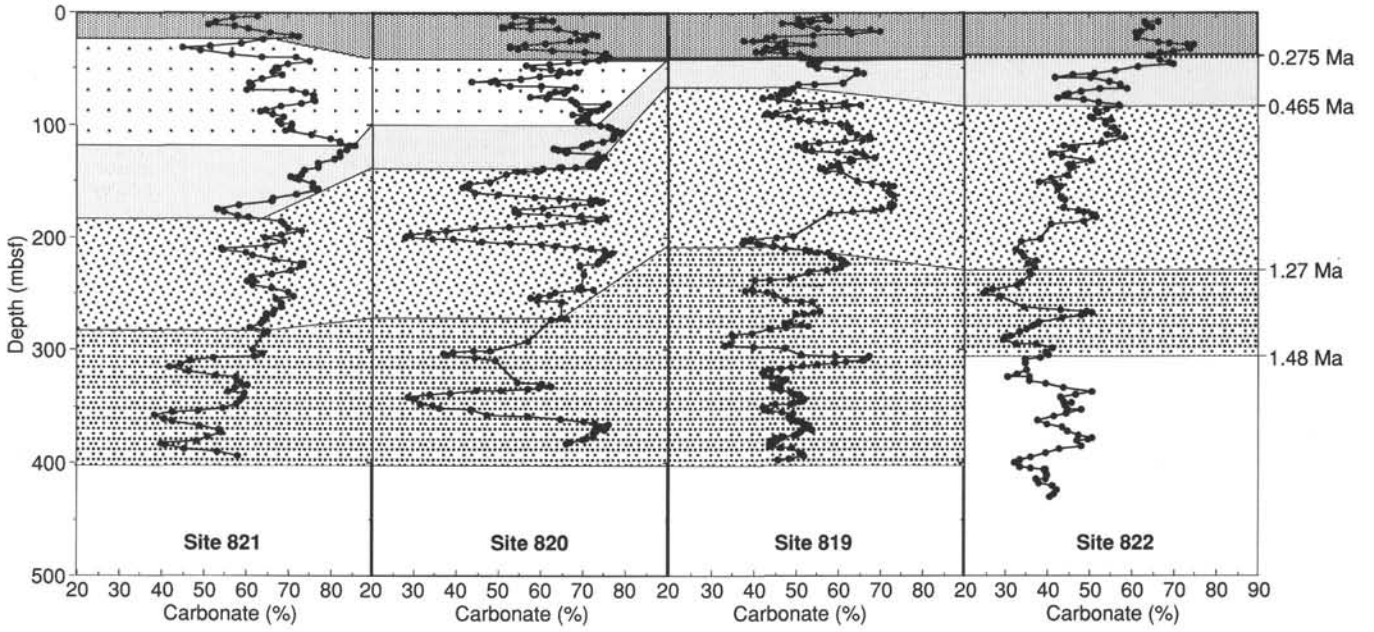

Figure 25. Smoothed carbonate datums for Sites 819 through 822, with biostratigraphic units.

formation of dolomite. As an example of the amount of Mg^{2+} that might be produced through dissolution of HMC, Swart and Guzikowski (1988) estimated that sediments containing 20% HMC (typical of the sediments at Site 821) might produce sufficient Mg^{2+} to form a sediment containing approximately 8% dolomite. The possibility that the absence of HMC at Sites 820 and 821 represents an influx signal is unlikely, considering that the sites nearest the probable source of HMC contain the lowest concentrations of this mineral. Second, all sites exhibit strongly negative Mg^{2+} gradients, the most negative of which occurs at Site 821, which is coincident with the highest concentration of dolomite. Although the amount of Mg^{2+} contained in pore waters is insufficient to produce significant concentrations of dolomite, the diffusion of Mg^{2+} from seawater might provide a source of Mg^{2+} should the dolomite form near the seafloor.

Diagenesis of feldspars (principally albite) to form kaolinite, illite, and other clay minerals may influence the chemistry of the interstitial waters according to their position relative to the continental margin. These reactions might influence dolomitization through the utilization of Mg^{2+} and the creation and destruction of alkalinity. The principal raw material for this series of reactions is feldspar albite ($NaAlSi_3O_8$). This mineral degrades to kaolinite, according to the following generalized Equation 1:

$$2NaAlSi_3O_8 + 2CO_2 + 11H_2O = Al_2Si_2O_5(OH)_4 + 2Na^+ + 2HCO_3^- + 4H_2SiO_4. \quad (1)$$

This process releases both HCO_3^- and Na^+ to the pore fluids. As one can see from Figure 30, concentrations of Na^+ in the interstitial pore fluids increase relative to the continental shelf, suggesting that the process of albite diagenesis occurs to a greater extent at the proximal sites. At Site 821, for example, an increase in Na^+ of almost 80 mM takes place between the sediment/seawater surface and 100 mbsf. According to the stoichiometry of Equation 2, this reaction should produce a similar increase in alkalinity and may promote dolomitization to a greater degree at Sites 820 and 821 than at Sites 822 and 819. Because such an increase in alkalinity was not observed in the pore water, HCO_3^- must be lost either through precipitation of carbonate or through a reverse reaction of kaolinite to form chlorite, as shown in Equation 2.

$$Al_2Si_2O_5(OH)_4 + 5Mg^{2+} + 10HCO_3^- + SiO_2 = Mg_5Al_2Si_3O_{10}(OH)_8 + 10CO_2 + 3H_2O. \quad (2)$$

$$1.1Al_2Si_2O_5(OH)_4 + 0.8K^+ + 0.5Mg^{2+} + 1.2SiO_2 = K_{0.8}Mg_{0.5}Al_{2.2}Si_{3.4}O_{10}(OH)_2 + 1.8H^+ + 0.3H_2O. \quad (3)$$

Kaolinite also reacts to produce illite, according to Equation 3. This process removes K^+ and Mg^{2+} from the pore fluids. As one can see from Equation 3, the ratio of K^+/Mg^{2+} used in this process is approximately unity; thus, the large decrease in Mg^{2+} seen at all sites cannot be a result of this reaction only. Another reaction that may be significant in further alteration of the minerals at these sites involves the formation of montmorillonite from kaolinite, according to Equation 4. Although using both K^+ and Mg^{2+}, this ratio is approximately 1:8. In addition, when Na^+ is removed from the pore fluids, sediments indicating the significance of this reaction should exhibit a decrease in Na^+, for example:

$$1.67Al_2Si_2O_5(OH)_4 + 0.84Mg^{2+} + 0.2Na^+ + 0.1K^+ + 4.66Si0_2 = (Na_{0.2}K_{0.1}Mg_{0.1}Mg_{0.18})Mg_{0.66}Al_{3.34}Si_8O_{20}(OH)_4 + 1.98H^+ + 0.35H_2O. \quad (4)$$

An interesting difference in the profiles of slope vs. depth of Mg^{2+} and K^+ occurs among the four sites (Fig. 28). The magnitude of change in concentrations of Mg^{2+} in the upper 50 mbsf increases steadily in those sites away from the continent. However, in the lower 375 m of cores, these profiles exhibit little change, and concentrations are lower at Sites 821 and 820, compared with those at Sites 822 and 819. In contrast, the

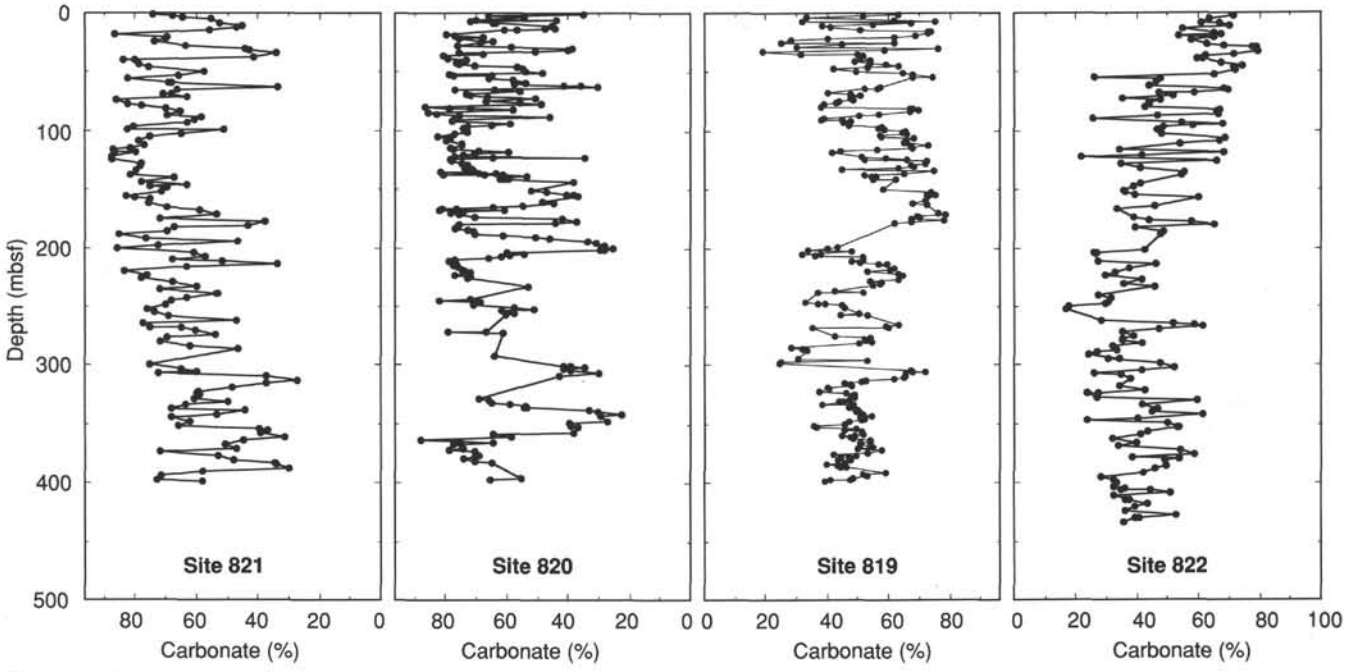

Figure 26. Summary of carbonate data as a function of depth for Sites 819 through 822.

magnitude of the decreased concentrations of K^+ is largest in the continental sites. These differences suggest that an alteration process involving Mg^{2+} and K^+ takes place more rapidly in the distal sites above 25 mbsf. Below this depth, either a different series of reactions dominate or conditions are more favorable at the proximal sites.

Sites 819 through 822 will allow us to gain a unique insight into diagenetic processes that occur off a continental margin dominated by influxes of siliciclastic and metastable carbonate minerals. In some portions of the core, HMC may have dissolved, perhaps under the influence of degradation of albite and organic materials. This process, in conjunction with conversion of kaolinite to illite, has promoted the formation of dolomite. Although, some dolomitization probably is still taking place today, most of this dolomite formation probably occurred near the sediment/seawater interface, where maximum rates of organic- material reduction and diagenesis of clay minerals took place.

ORGANIC GEOCHEMISTRY

In addition to monitoring hydrocarbons for safety, the main purpose of our shipboard organic geochemistry studies at Site 822 was to assess the amounts and origin of organic matter preserved in Pleistocene to Pliocene mixed sediments deposited on the lower slope of Queensland Trough, in front of today's Great Barrier Reef. Our second purpose was to characterize the proportions of different light hydrocarbons generated in the sediments through biogenic or thermogenic decay of organic matter.

Samples

Forty-two samples were collected from Hole 822A at 10-m intervals over a depth range from 8 to 430 mbsf. All sediments were analyzed for their compositions of light hydrocarbons (C_1–C_6), using headspace analyses, and for total nitrogen, sulfur, and carbon contents, using an NA 1500 Carlo Erba NCS analyzer.

Volatile Hydrocarbons

Hydrocarbon gases (C_1–C_6) in sediments were analyzed as part of ODP's safety and pollution-prevention monitoring program, using the headspace technique, the vacutainer technique (when gas pockets were observed in the core liner), the Carle gas chromatograph (for determining C_1–C_3 concentrations), and the NGA gas chromatograph (mainly for determining C_4–C_6 concentrations). The results of 48 headspace analyses from Hole 822A are presented in Table 5. In Figure 31, we present WSTP-temperature data from Sites 817, 820, and 822, and the geothermal gradient used at Site 822 for interpreting the depth-related evolution of the C_1/C_2 ratio.

Sediments at Site 822 contained high concentrations of methane, which represented no safety and/or pollution hazards. The evolution of the C_1/C_2 ratio with increasing depth and temperature did not indicate any anomalous trend (Fig. 32), and values from headspace analyses ranged between 27,000 and 1,500 (normal to unusual trends between 10° and 33°C). A sharp decrease in methane content encountered between 90 and 205 mbsf explains the shift of the C_1/C_2 ratio within an unusual field between 14° and 18°C.

Headspace concentrations of methane gas were low in the sulfate reduction zone (Fig. 33, see also "Inorganic Geochemistry" section, Fig. 21, this chapter), but with ethane, increased rapidly below 10 mbsf. Concentrations reached maximum values at 55 mbsf (methane = 77,000 ppm and ethane = 4 ppm in Sample 133-822A-7H-5, 140–141 cm) and rapidly decreased below this depth. Scattered amounts of propane appeared between 155 and 230 mbsf, and below 265 mbsf, concentrations exceeded those of ethane (C2/C3 ratio < 1, Fig. 33). Significant concentrations of iso-butane and isopentane were observed in headspace samples and in gas pockets below 265 mbsf (Table 5).

The observed coincidence between low SO_4^{2-} concentrations and high amounts of methane (> 1000 ppm) with trace amounts of ethane in these sediments suggests a bacterial

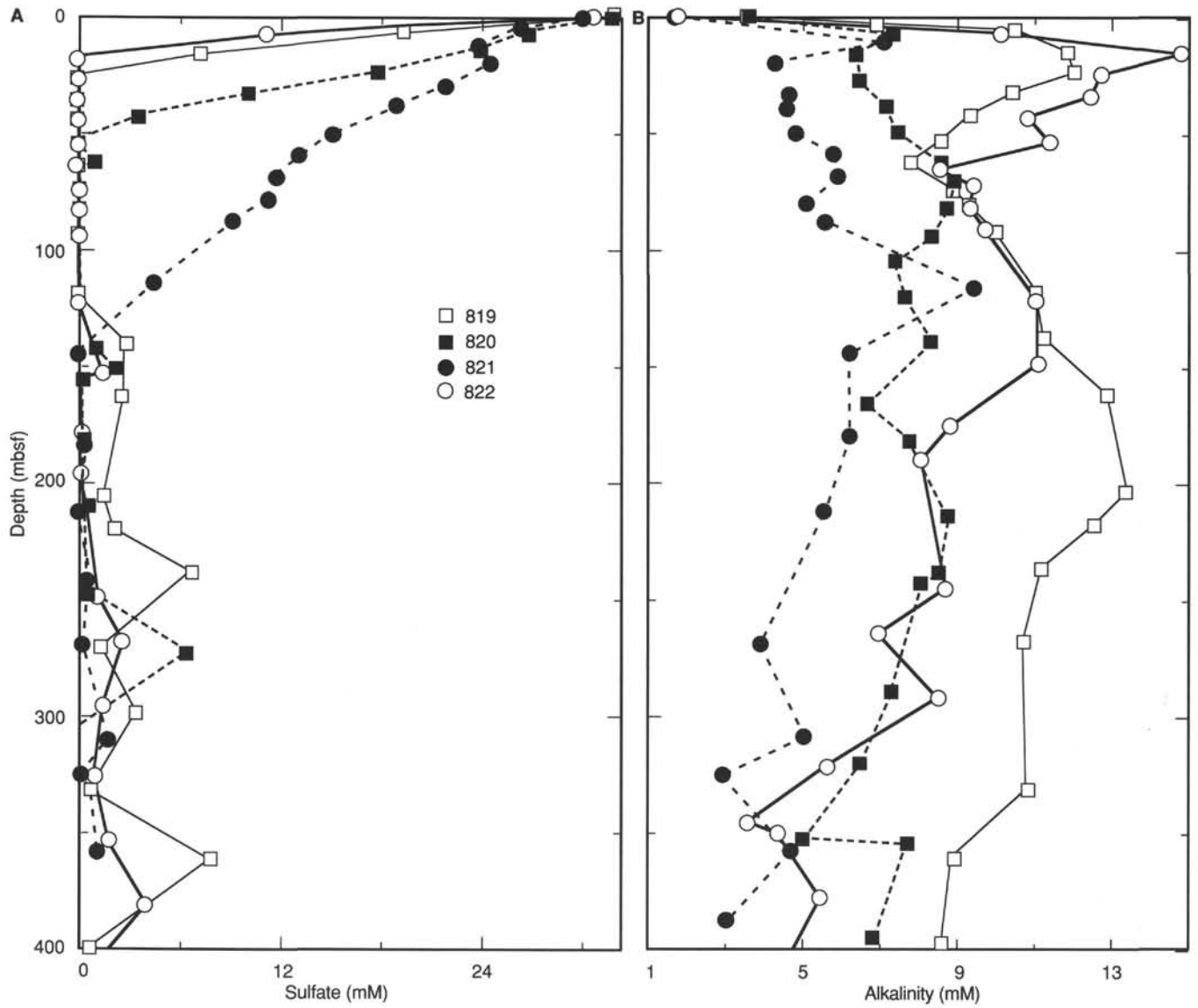

Figure 27. Changes in sulfate (A) and alkalinity (B) at the four continental sites (Sites 819 through 822).

origin for methane (and for ethane?) in the SO_4^{2-}-free section (between 15 and 265 mbsf) of sediments at Site 822 (Fig. 34). Below 265 mbsf, the appearance of propane, butane, and pentane; the progressive increase in concentrations of C_1, C_2, and C_3; and a decrease of both the C_2/C_3 and $C_1/(C_2+C_3)$ ratios at shallow depths and low temperatures (Figs. 33 and 34) are factors that clearly indicate the beginning of a mixing with thermogenic-free hydrocarbons. Below 300 mbsf, variations in concentrations of gas may result from very sharp changes in porosity of the sediments (see also "Physical Properties" section, this chapter).

Organic Carbon Contents

Contents of total organic carbon (TOC) and total inorganic carbon together with concentrations of total nitrogen and sulfur concentrations recorded in Site 822 are presented in Table 6.

Amounts of organic carbon at Site 822 did not exceed 0.65% TOC (Fig. 35). Cyclic changes in TOC values seem to follow variations in the carbonate/clay contents of these sediments (i.e., the highest organic contents were observed in the clayey-rich sediments encountered in Subunits IIB and IIC; Fig. 35; see also "Lithostratigraphy" section, this chapter).

Concentrations of total sulfur in these sediments ranged between 0% and 1% and showed progressive and cyclic increases with depth (Table 6).

Concentrations of total nitrogen in the sediments ranged from 0.05% to 0.12%, increased progressively with depth, and followed the trend of both organic carbon and clay contents of the sediments (Fig. 35).

On the basis of TOC/nitrogen ratios (Fig. 35), marine organic matter is abundant in all the lithologies encountered at Site 822. The coincidence between increasing organic carbon and nitrogen contents in clayey sediments may indicate better preservation of organic matter in the finest grain-size sediments. As a consequence of low organic contents, we were unable to conduct detailed geochemical characterizations of kerogen types using the Rock-Eval pyrolysis method as originally planned. More detailed shore-based studies (elemental analysis and optical investigations of extracted kerogens) will permit characterization of short-term fluctuations in vertical

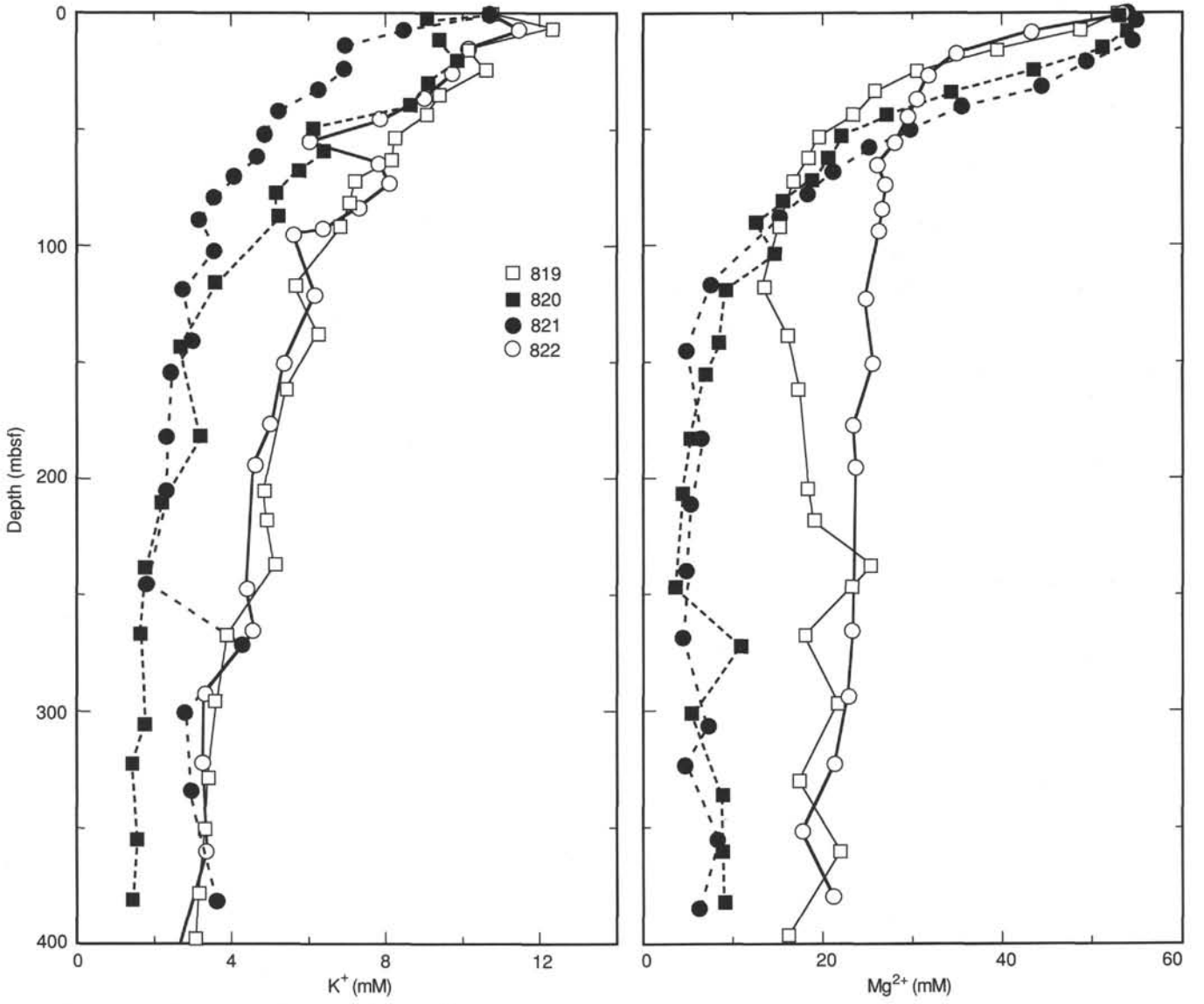

Figure 28. Variation in concentrations of K^+ and Mg^{2+} at Sites 819 through 822.

distribution and preservation of the different components of organic matter in sediments encountered at Site 822.

PHYSICAL PROPERTIES

Physical properties analyzed in cores from this site include bulk density, *P*-wave velocity, and magnetic susceptibility on unsplit cores and *P*-wave velocity, electrical-resistivity formation factor, shear strength, and index properties (including bulk density, grain density, water content, porosity, and void ratio). The methods used are described in detail in the "Explanatory Notes" chapter (this volume).

Conclusions Based on Physical Properties Data at Site 822

Two basic physical-property units were identified in terms of physical properties at Site 822 (see data in Tables 7 through 11). Unit A extends from the seafloor to 130 mbsf and consists predominantly of bioclastic and nannofossil oozes. Physical properties data indicated gradual changes, consistent with normal compaction trends (see Figs. 36, 37, and 38). An increasing trend was observed for bulk densities, with values going from 1.75 to 1.94 g/cm_3 over the 130-m interval (Fig. 37A). A gradual decrease in porosity and water content downhole was observed. Porosity values range from 60% at 2 mbsf to 50% at 130 mbsf (Fig. 37B), whereas water contents range from 54% to 35% (Fig. 37C) for the same interval. Figure 39 presents a plot of water content vs. density. *P*-wave velocity was measured for the top 31 mbsf only because we could not detect the 500-kHz compressional wave through unsaturated gassy sediments. Values of this property range from 1.52 to 1.61 km/s over the top 31-m interval (Fig. 37D). Formation factor data exhibited large variations, from 3.3 near the seafloor to about 5.0 at 130 mbsf (Fig. 37E). Vane shear strength exhibited a distinct increase from 10 kPa near seafloor to 85 kPa at 83 mbsf (Fig. 37F). Thermal conductivity values range between 0.85 and 1.2 W/m K (Fig. 37G).

Unit B, which extends from 130 to 430 mbsf, consists of mixed sediments of claystone and chalk. Physical-property data indicate greater variability, but remain relatively constant with depth. Bulk densities increase slightly from 1.95 to 2.1 g/cm^3, and then decrease to about 1.9 g/cm^3 at 390 mbsf. In this unit, the largest bulk density value was found at 342 mbsf. A noticeably high bulk-density value (2.35 g/cm^3) at 426 mbsf

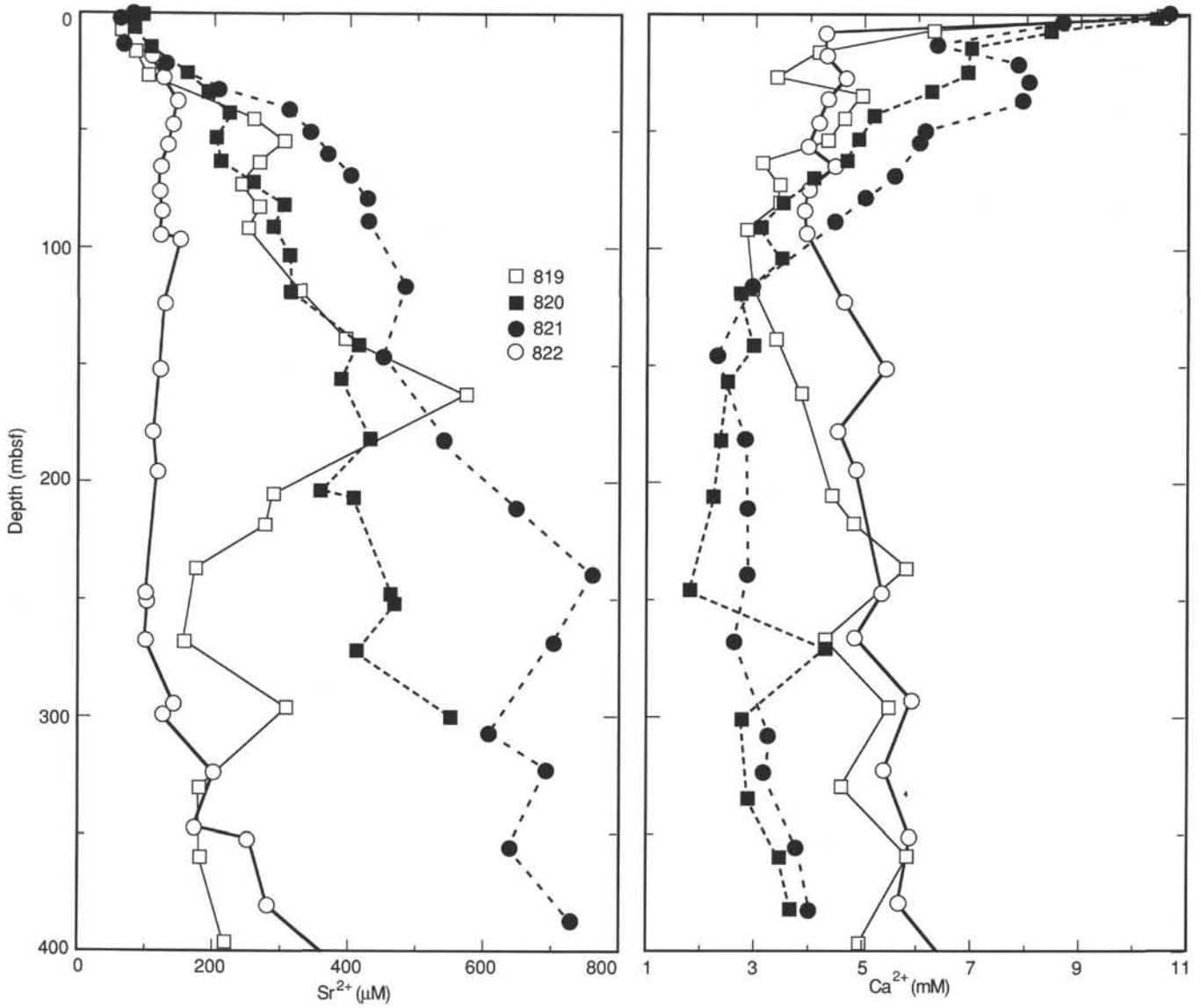

Figure 29. Variation in concentrations of Sr^{2+} and Ca^{2+} at Sites 819 through 822.

probably results from the occurrence of lithified material. Both porosity and water contents decrease slightly in this unit but exhibit large variations, which we found correlated with the occurrence of intercalations of claystone and chalk. In general, clay-rich sediments exhibit low bulk density and high porosity and water contents. Average formation factor values increase from 5.8 in the shallower part of this unit to about 6.3 at the interval between 200 and 300 mbsf because of a decrease of porosity during normal compaction. Thermal conductivity values vary between 1.0 and 1.3 W/m K, slightly higher than those in Unit A.

DOWNHOLE MEASUREMENTS

Reliability of Logs

Hole size is the most important control for accuracy of logs from Leg 133; hole size at Hole 822A was the most variable of that at any site during Leg 133. This variability had two effects on Site 822 logging: first, changes in hole size dominated log responses of some tools (as discussed later in this section). Second, hole constrictions or "bridges" prevented tool strings from reaching the bottom of the hole. Although total depth at logging time was 400 mbsf, logged intervals were from 324.7 to 66.7 mbsf for the seismic stratigraphic combination, 321.4 to 0.0 mbsf for the geochemical combination, and 179.6 to 83.4 mbsf for the FMS. These bridges probably were caused mostly by swelling clays, but caving silts also may have contributed.

Three types of caliper log were obtained (1) an apparent caliper that was calculated from the sonic log (see "Explanatory Notes" chapter, this volume), (2) a caliper from the mechanical caliper device (MCD), and (3) a two-axis caliper (Fig. 40) from the FMS. The lithodensity tool caliper did not operate at this site. The FMS caliper is much more reliable than either the sonic or MCD calipers, but the FMS was run only over the interval from 83.4 to 179.6 mbsf because of a bridge at 182 mbsf.

As is often the case with ODP holes, initial sonic logs from Hole 822A exhibited a few zones in which cycle-skipping caused apparent velocity to have unreliable swings. Reprocessing (see "Explanatory Notes" chapter, this volume) removed all unreliable data, and we consider the reprocessed velocity log in Figure 40 to be of good quality. For the short interval from 308.5 to 324.7 mbsf at the bottom of the hole,

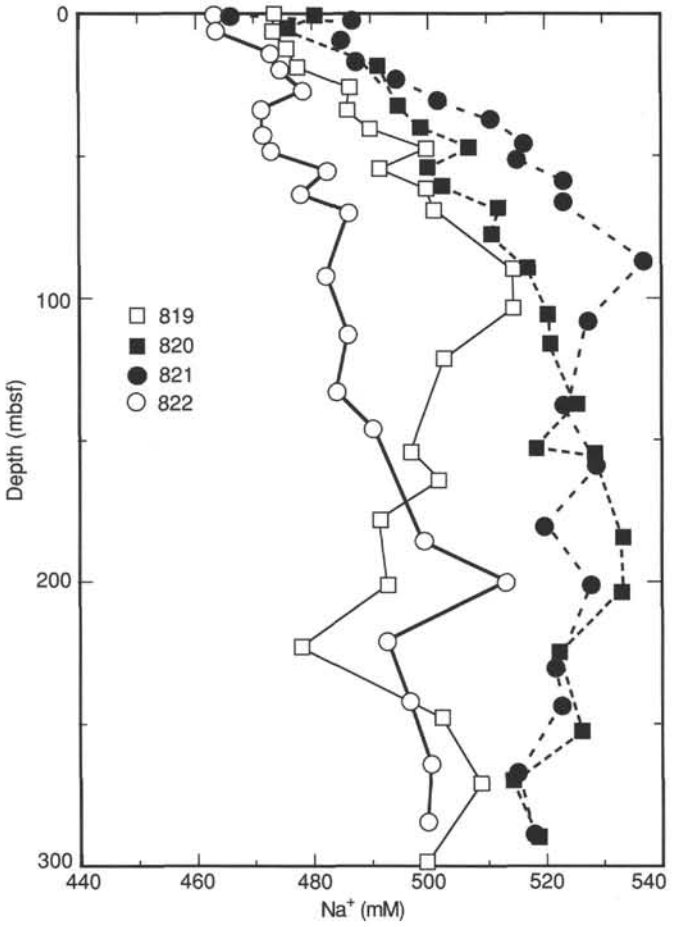

Figure 30. Variation in concentrations of Na^+ at Sites 819 through 822.

resistivity logs (but not sonic logs) are available because the resistivity tool is much lower on the tool string. A pseudosonic log was generated and used for this interval and is based on regression of sonic transit time on a logarithm of shallow resistivity for the overlying interval from 296.8 to 308.4 mbsf ($R = -0.66$).

The spectral gamma-ray tool is the only tool on the seismic stratigraphic combination that can provide useful formation data even through pipe. On the geochemical tool string, useful through-pipe data were obtained by the spectral gamma-ray, aluminum clay, and gamma-ray spectroscopy tools. At Hole 822A, through-pipe spectral gamma-ray logs were obtained for the interval from 66.6 to 74.0 mbsf during one run of the seismic stratigraphic combination and for the intervals from 0 to 74.0 mbsf and from 0 to 79.0 mbsf during two runs of the geochemical combination; these geochemical runs have a higher signal-to-noise ratio for spectral gamma-ray logs as a result of slower logging speed. Through-pipe aluminum and gamma-ray spectroscopy logs also were obtained with two passes of the geochemical string, while pipe was moved 5 m between both passes to permit discrimination of changes in pipe thickness with changes in the formation. Subjective examination of through-pipe geochemical logs for Hole 822A indicates that these did detect geochemical changes in formation. However, as yet we have not corrected for pipe changes in these logs.

A repeated pass of the geochemical combination also obtained a short interval of openhole logs. As expected, the second runs of spectral gamma-ray and aluminum logs were offset by irradiation effects in zones where the tool string paused or slowed for calibration before beginning the second run. However, in general, the two passes exhibit a high correlation in log character (Fig. 41).

During the first repeat pass of the seismic stratigraphic combination, we concluded that numerous large-diameter portions of the lithodensity run were obtained with only marginal or without pad contact against the borehole wall and thus yielded biased measurements. Further, we suspected that the large tool drag that we observed at that time was caused by the open density caliper in a sticky, variable-diameter hole. Therefore, we decided that values from the density log were insufficient to justify any increased risk of losing tools; thus, we ran the main logging pass with a closed density caliper. Density data were obtained (Fig. 40), but almost all these were biased to values that were too low. The FMS (see microfiche, this volume) also was affected adversely by the variability of the hole; this tool often lost pad contact with at least two of the four pads in those portions of the hole that were larger than the maximum 15-in. (38.1 cm) opening of the caliper (Fig. 40). Other types of logs do not require pad contact and thus usually are insensitive to changes in borehole size. However, interlog relationships discussed later in this section suggest that changes in hole size were severe enough at Site 822 to dominate many log responses.

Two porosity-sensitive logs were obtained at Site 822 using the geochemical tool string (Fig. 42): neutron and hydrogen. An uncalibrated neutron porosity log was generated by the aluminum clay tool; because the source of californium is much stronger than those sources of americium and beryllium used in conventional neutron porosity tools, apparent porosities are much higher and uncalibrated. Apparent neutron porosity values at Hole 822A were from 120% to 180% (fractional "porosities" of 1.2 to 1.8), but relative porosity variations can be reliable (see "Site 820" chapter, this volume). The gamma-ray spectroscopy tool (GST) detects variations in amount of hydrogen relative to several other elements (see "Explanatory Notes" chapter, this volume); again, these values were uncalibrated, but potentially useful as a relative measure. For both neutron porosities and GST hydrogen counts, total hydrogen has been detected without distinguishing whether hydrogen is free water in pores or bound water in clay minerals. Thus, these two logs may have overestimated the porosity in clay-rich intervals.

Relative Effects on Logs of Lithology, Porosity, and Hole Size

Changes in velocity with depth (Fig. 40) generally follow a gradual compaction profile, which suggests that mechanical compaction dominates diagenesis for controlling porosity at this site. Similar patterns were observed at Sites 814, 817, 819, 820, and 821 (see "Site 814," "Site 817," "Site 819," "Site 820," and "Site 821" chapters (this volume). Velocity within the logged open-hole interval is somewhat greater than one normally observes in terrigenous or calcareous sediments of comparable depths. Average velocity increased from 1.7 km/s at 75 mbsf to 2.2 km/s at 320 mbsf, compared with typical values for these depths of 1.55 to 1.60 and 1.9 km/s (Hamilton, 1979).

The velocity log was converted to a log of integrated traveltime (Fig. 43) to facilitate depth-to-time conversions for comparison of Site 822 data to seismic facies. For the unlogged interval between the seafloor and 72.0 mbsf, we used a simple linear interpolation between water velocity at the seafloor and the first log value at 72.0 mbsf. Subjectively, we estimate an error of less than 6 ms is associated with uncertainties of velocities in the top 72.0 mbsf. The reprocessed

Table 5. Volatile hydrocarbon data from headspace and vacutainer analyses at Site 822.

Core, section, interval (cm)	Depth (mbsf)	Sample	Volume (mL)	Gas chromato.	C_1 (ppm)	C_2 (ppm)	C_3 (ppm)	C_1/C_2	C_2/C_3	$C_1/(C_2+C_3)$
133-822A-										
2H-5, 149–150	8.39	HS	5	CAR132	3	0	0			
3H-5, 149–150	17.89	HS	5	CAR132	1,913	0	0			
4H-5, 149–150	27.39	HS	5	CAR132	57,686	2	0	28,843		28,843
5H-5, 140–141	36.8	HS	5	CAR132	75,000	4	0	18,750		18,750
7H-5, 140–141	55.8	HS	5	CAR132	77,077	4	0	19,269		19,269
8H-5, 140–141	65.3	HS	5	CAR132	59,024	3	0	19,675		19,675
9H-5, 140–141	73.89	HS	5	CAR132	53,845	2	0	26,922		26,922
10H-5, 140–141	83.5	HS	5	CAR132	60,274	3	0	20,091		20,091
11H-5, 140–141	93.8	HS	5	CAR132	7,505	1	0	7,505		7,505
12X-3, 149–150	100.39	HS	5	CAR132	39,670	3	0	13,223		13,223
13X-2, 149–150	108.69	HS	5	CAR132	15,073	2	0	7,536		7,536
14X-4, 140–141	121.3	HS	5	CAR132	4,503	1	0	4,503		4,503
15X-2, 149–150	127.99	HS	5	CAR132	15,538	3	0	5,179		5,179
16X-3, 149–150	139.09	HS	5	CAR132	6,209	1	0	6,209		6,209
17X-5, 140–141	151.7	HS	5	CAR132	6,771	2	0	3,386		3,386
18X-3, 149–150	158.49	HS	5	CAR132	9,376	3	2	3,125	1.5	1,875
19X-3, 149–150	168.19	HS	5	CAR132	1,490	1	0	1,490		1,490
20X-3, 149–150	177.79	HS	5	CAR132	8,971	2	0	4,486		4,486
21X-3, 149–150	187.09	HS	5	CAR132	4,260	1	0	4,260		4,260
22X-1, 149–150	193.69	HS	5	CAR132	6,294	2	0	3,147		3,147
23X-2, 149–150	204.49	HS	5	CAR132	854	0	0			
25X-4, 149–150	226.89	HS	5	CAR132	8,005	2	2	4,002	1.0	2,001
27X-5, 140–141	247.14	HS	5	CAR132	4,388	1	0	4,388		4,388
28X-3, 149–150	254.29	HS	5	CAR132	5,462	1	0	5,462		5,462
29X-5, 149–150	265.83	HS	5	CAR132	9,369	3	5	3,123	0.6	1,171
30X-6, 149–150	278.09	HS	5	CAR132	9,513	4	5	2,378	0.8	1,057
31X-4, 149–150	283.85	HS	5	CAR132	9,967	4	5	2,492	0.8	1,107
32X-4, 149–150	294.39	HS	5	CAR132	8,265	3	4	2,755	0.8	1,181
33X-5, 149–150	305.59	HS	5	CAR132	9,475	4	7	2,369	0.6	861
34X-2, 149–150	310.79	HS	5	CAR132	3,403	2	4	1,702	0.5	567
35X-4, 149–150	323.49	HS	5	CAR132	29,282	6	11	4,880	0.5	1,722
36X-1, 40–41	327.4	HS	5	CAR132	30,867	6	8	5,144	0.8	2,205
37X-5, 149–150	343.45	HS	5	CAR132	9,984	5	9	1,997	0.6	713
38X-4, 140–141	352.2	HS	5	CAR132	17,255	4	7	4,314	0.6	1,569
39X-1, 149–150	357.39	HS	5	CAR132	7,668	4	9	1,917	0.4	590
40X-5, 149–150	372.99	HS	5	CAR132	7,952	3	6	2,651	0.5	884
41X-3, 149–150	378.91	HS	5	CAR132	24,942	5	6	4,988	0.8	2,267
42X-5, 149–150	392.29	HS	5	CAR132	57,984	12	20	4,832	0.6	1,812
44X-4, 140–141	405.9	HS	5	CAR132	6,916	2	6	3,458	0.3	864
45X-5, 149–150	412.12	HS	5	CAR132	9,878	4	8	2,470	0.5	823
46X-5, 149–150	421.71	HS	5	CAR132	45,703	9	16	5,078	0.6	1,828
47X-4, 140–141	430.2	HS	5	CAR132	15,765	7	21	2,252	0.3	563
5H-1, 20–25	29.6	VAC	5	CAR132	48,009	1	0	48,009		48,009
6H-2, 0–5	40.4	VAC	5	CAR132	109,325	5	0	21,865		21,865
8H-2, 100–110	60.4	VAC	5	CAR132	250,000	18	2	13,889	9.0	12,500
9H-3, 10–20	69.59	VAC	5	CAR132	421,910	36	4	11,720	9.0	10,548
10H-3, 55–60	79.65	VAC	5	CAR132	510,994	47	5	10,872	9.4	9,827
11H-2, 10–15	88	VAC	5	CAR132	757,324	71	7	10,667	10.1	9,709
15X-5, 0–10	131	VAC	5	CAR132	17,861	1	0	17,861		17,861
16X-3, 10–15	137.7	VAC	5	CAR132	7,102	0	0			
29X-5, 0–10	264.34	VAC	5	CAR132	196,000	37	15	5,297	2.5	3,769
30X-4, 0–10	273.6	VAC	5	CAR132	93,021	9	4	10,336	2.3	7,155
31X-3, 0–20	280.86	VAC	5	CAR132	308,000	61	27	5,049	2.3	3,500
33X-4, 0–50	302.6	VAC	5	CAR132	182,000	36	20	5,056	1.8	3,250
42X-2, 0–5	386.3	VAC	5	CAR132	7,046	1	1	7,046	1.0	3,523
45X-4, 0–10	409.13	VAC	5	CAR132	390,000	144	128	2,708	1.1	1,434
46X-2, 0–1	415.72	VAC	5	CAR132	305,000	107	96	2,850	1.1	1,502

HS = headspace sample; VAC = vacutainer sample.

sonic log was used to calculate a synthetic seismogram, based on the algorithm described in the "Explanatory Notes" chapter (this volume). This synthetic seismogram is shown and interpreted in the "Seismic Stratigraphy" section (this chapter).

Lithostratigraphy at Site 822 is dominated by variations in concentration of two principal components: carbonate (either as nannofossils or micrite) and clay minerals. Quartz is present, but usually subsidiary, although locally, concentrations may be high. We based this conclusion on smear-slide descriptions (see "Lithostratigraphy" section, this chapter). On the basis of logging results at lithologically similar Site 820 (see "Site 820" chapter, this volume), we think that this conclusion can be independently demonstrated by geochemical logs. Figure 44 presents the strong correlation among geochemical logs that was obtained using three different tools. Log values for potassium, aluminum, and silicon (all abundant in the clay minerals, illite and kaolinite) are positively correlated with each other. Iron values are somewhat correlated with values for these other elements, but in general, variations in iron values probably are near the iron noise level of the GST tool. Surprisingly, logs of these elements usually are also positively correlated with values for calcium. An inverse correlation with calcium might be expected if these geochemical logs were semiquantitative indicators of relative abundance of calcite and clay minerals. The positive correlation

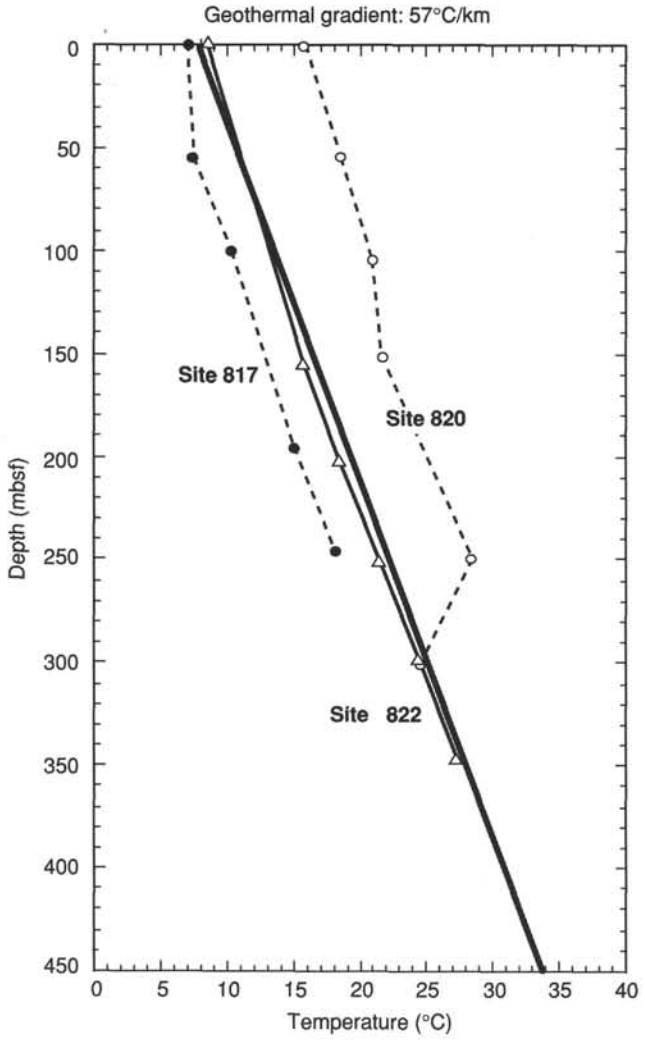

Figure 31. Geothermal gradient and WSTP temperature data from Sites 817, 820, and 822.

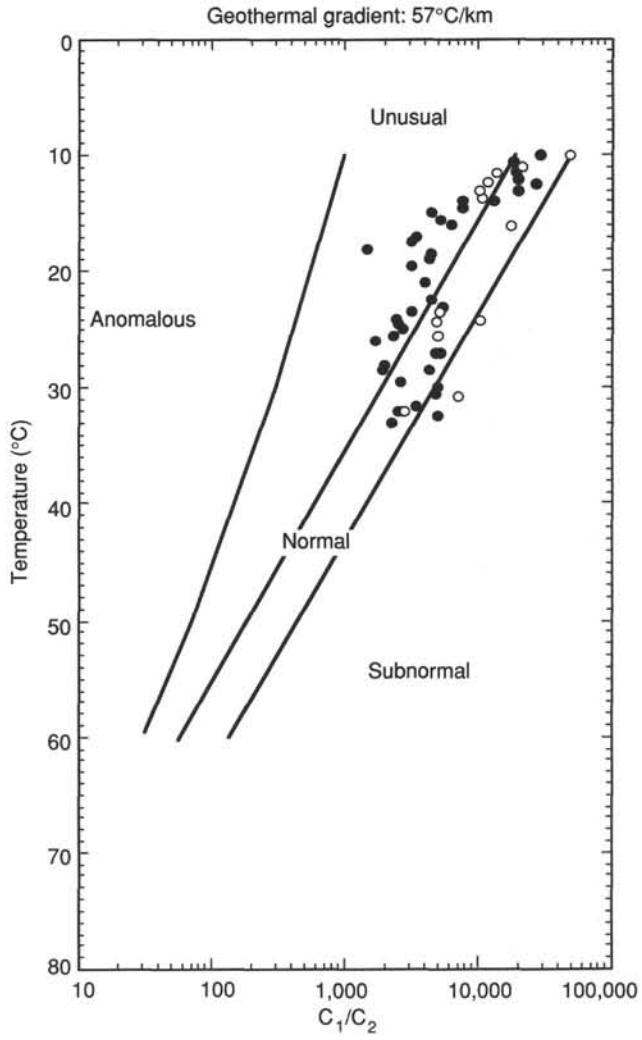

Figure 32. Distribution of the C_1/C_2 ratio from headspace analyses with temperature at Site 822. This diagram was compiled for ODP's shipboard safety and pollution-prevention monitoring program.

among all logged formation elements suggests that another component is present whose variations created these geochemical log responses.

Neutron and hydrogen porosity logs in Figure 42 depict a strong inverse correlation with the geochemical logs in Figure 44, implying that water is the component responsible for geochemical log minima. Further, these two porosity logs only moderately correlate with resistivity and velocity logs, two logs that are relatively insensitive to variations in hole size.

Velocity and resistivity strongly correlate throughout almost all of the logged interval at Hole 822A (Figs. 40 and 42). This correlation results from dominance of porosity in both logs; ratios of these logs (Fig. 45) may provide clues regarding pore geometry (see "Site 817" chapter, this volume). Here, a normal compaction pattern of increasing resistivity with increasing depth was not found below 170 mbsf (Fig. 40), although the velocity log exhibits a normal compaction pattern throughout the logged interval. Such a difference between velocity and resistivity trends had not been observed before during Leg 133. Further post-cruise analysis will be required to evaluate possible mechanisms that might account for this trend, because the trend may involve an integration of lithological, geochemical, and physical property data with downhole logs. This relatively constant resistivity does not imply a relatively constant porosity. Porosities calculated from resistivity use the electrical resistivity formation factor, a ratio of formation resistivity to water resistivity (Fig. 45), which does exhibit a subtle increase over this interval because of an assumed temperature-induced decrease in resistivity of pore water with depth (see "Explanatory Notes" chapter, this volume).

All the geochemical and porosity log responses can be accounted for by a dominant effect of variations in hole size on all logs except velocity and resistivity logs. To investigate this hypothesis further and possibly remove or reduce this effect of hole size, we used principal components analysis.

We applied principal components analysis to the interval from 74.3 to 313.6 mbsf for the following seven logs: neutron porosity, hydrogen counts, silicon counts, calcium counts, aluminum, gamma-ray, and potassium. The first principal component, which accounts for 61.7% of the covariance of these logs, clearly is a hole-size effect for it consists of roughly equal weightings for all seven logs, with neutron porosity and hydrogen counts having a sign opposite that of the other logs. Thus, this first principal component is a pseudocaliper log, which moderately correlates with the FMS caliper (Fig. 46).

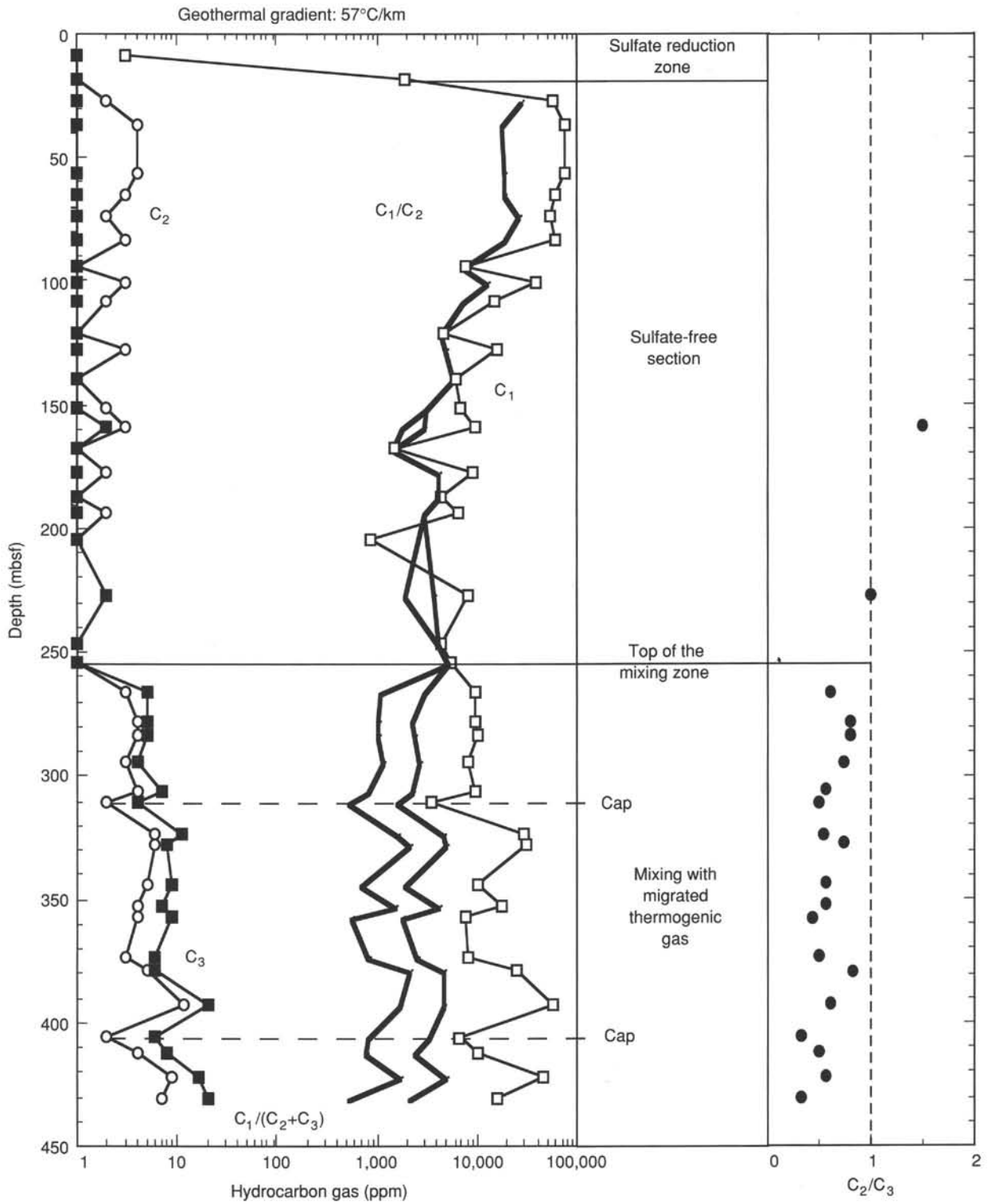

Figure 33. Distribution with depth of amounts of hydrocarbon gases in headspace samples at Site 822. Evolution of C_1/C_2, C_2/C_3, and $C_1/(C_2 + C_3)$ ratios.

The second principal component, which accounts for 18.6% of the covariance, can be identified as variations in relative proportions of carbonate and clay: calcium counts are heavily weighted and are opposite in sign to all other logs (except aluminum, which for unknown reasons is near zero in contribution). This second principal component is the pattern that one might have seen were borehole conditions better, as they were at Site 820 (see "Site 820" chapter, this volume). However, because principal components analysis and this second principal component are subject to noise in all seven logs, we consider this component to be only a general guide to variations in relative proportions of carbonate and clay min-

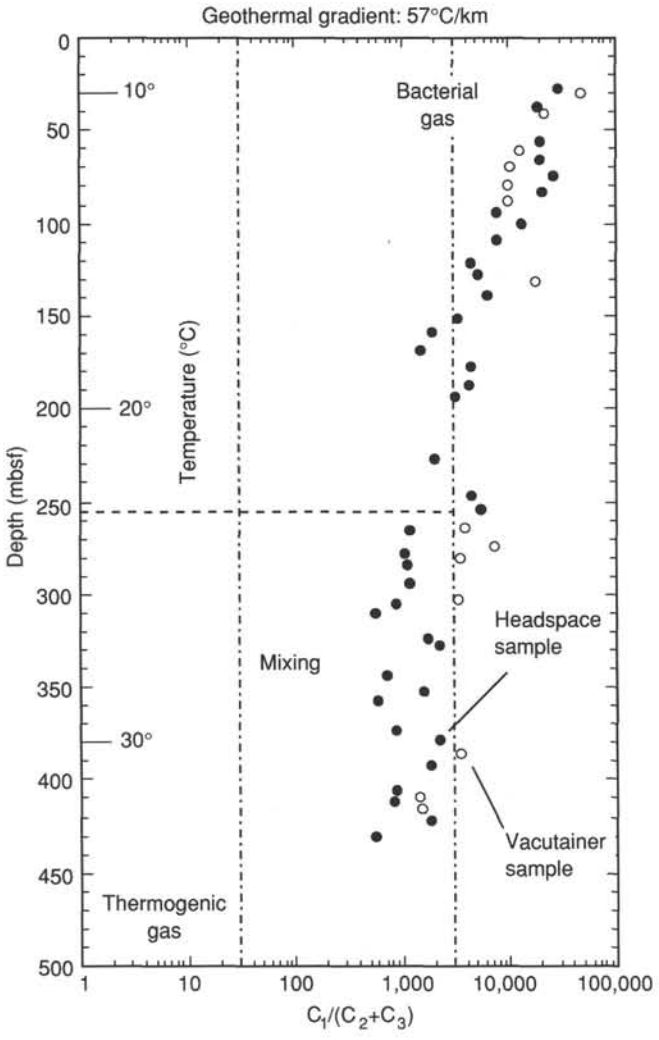

Figure 34. Evolution with depth and temperature of the $C_1/(C_2 + C_3)$ ratio at Site 822. Vertical dash-dot lines show approximate positions of bacterial, mixed, and thermogenic gases. Horizontal lines indicate separation into purely bacterial and mixed gases.

erals. This second principal component only moderately correlates with resistivity and velocity, although the character of these last two logs also probably was controlled by variations in relative proportions of carbonate and clay minerals (see "Site 820" chapter, this volume). Thus, detailed lithologic interpretation of Site 822 logs must await more accurate removal of the effects of hole size post-cruise.

Log-Based Units

Based on log responses, the logged openhole interval of Site 822 can be divided into four units and several subunits: log Unit 1 is from the base of the pipe (66.7 mbsf) to 120 mbsf, log Unit 2 from 120 to 168 mbsf, log Unit 3 from 168 to 263 mbsf, and log Unit 4 from 263 mbsf to the bottom of the logged interval at 323 mbsf. All four log-based units are within lithologic Unit II (see "Lithostratigraphy" section, this chapter).

Log Unit 1 is characterized by a smooth compaction profile for velocity and resistivity logs, as shown in Figure 40. A small number of thin layers of higher resistivity and velocity can be seen that may have resulted from density changes within similar lithologies.

The top of log Unit 2 is characterized by a sharp decrease in resistivity and velocity, which can be seen to produce a marked A/B positive anomaly in Figure 45 for the zone from 120 to 124 mbsf. This pattern indicates the possibility of a simultaneous increase in both porosity and cementation (see "Site 817" chapter, this volume) which might be caused by dolomitization. This zone is followed downhole by an interval of increasing resistivity and velocity that has the signature of a sequence in which clay minerals are decreasing downhole (see "Site 820" chapter, this volume). Post-cruise processing of geochemical logs will be required before one may surmise firm conclusions regarding this log-based unit, because of the degradation caused by the large variability in borehole size. Furthermore, integration of the downhole log and laboratory geochemical data is difficult on board ship because of a substantial difference in sampling intervals used. A thin layer occurs from 148 to 150 mbsf, which has high resistivity and velocity from lithification, probably a dolomite stringer.

Log Unit 3 consists of two subunits in which the amplitude of resistivity and velocity logs is similar, but character is markedly different. Subunit 3A extends from 168 to 202 mbsf and begins with a low resistivity layer similar to that at the top of log Unit 2, followed by an interval having constant trends in both resistivity and velocity. Subunit 3B is highly variable and exhibits cyclic changes with wavelengths of 15 and 2 m. The thin bed indicator, "Thin R," and the A/B ratio (Fig. 45, see also "Site 815" chapter, this volume) show large amplitudes and increased variability, respectively. Further post-cruise analysis will be necessary to separate thin-bed effects from larger-scale variations, which might be investigated for climatic links.

Log Unit 4 can be subdivided into three subunits: Subunit 4A, from 263 to 294 mbsf, which has uphole increasing resistivity and velocity; Subunit 4B, from 294 to 305 mbsf, which is similar to the topmost portion of Subunit 4A; and Subunit 4C from 305 to 323 mbsf, which exhibits increasing resistivity and velocity with depth. It may be possible to identify these subunits as upward-coarsening or -fining cycles using geochemical logs after correction post-cruise.

Resistivity and velocity logs exhibit substantial variability at a spacing of 1 to 2 m, which is close to the resolving power of the sondes. The FMS was run at Site 822, and we should be able to identify these thin layers almost exactly because of its increased resolution. The combination of data from deeper-penetrating resistivity sondes used with the ODP seismic stratigraphy tool string and FMS images should enable us to estimate properties of the thin layers at Site 822 with far greater confidence than might be possible with only one logging string.

Temperature

We ran the L-DGO temperature tool at the bottom of our seismic stratigraphic, geochemical, and FMS tool strings. Because hole temperatures were reduced by circulation during coring and by hole conditioning immediately prior to logging, one might infer an equilibrium thermal profile from these logging runs. Our recorded maximum temperatures of 14.7° and 16.8°C for the two deepest runs (Fig. 47) thus are minimum estimates of equilibrium temperature. WSTP measurements at this site indicate a thermal gradient of about 62°C/km and an extrapolated bottom-water temperature of about 6°C (see "Physical Properties" section, this chapter). In comparison, temperature logging measurements of bottom-water temperature were 5.0°C for all three runs (Fig. 47). Comparison of temperatures for the first two runs shows virtually no warming of hole temperatures above 100 mbsf: about 0.3°C of warming at 200 mbsf and 2.1°C of warming at

Table 6. Concentrations of total organic carbon, inorganic carbon, total carbon, total nitrogen, and sulfur in X-ray diffraction and physical properties samples from Site 822.

Core, section, interval (cm)	Depth (mbsf)	Sample	Total organic carbon (%)	Total inorganic carbon (%)	Total carbon (%)	Total nitrogen (%)	Total sulfur (%)	TOC/nitrogen	TOC/sulfur
133-822A-									
2H-5, 145-150	8.35	XRD	0.54	8	8.54	0.07	0.14	7.7	3.8
3H-5, 140–150	17.8	XRD	0.22	8.08	8.3	0.05	0.39	4.4	0.56
4H-5, 140–150	27.3	XRD	0.13	8.2	8.33	0.05	0.24	2.6	0.54
5H-5, 140–150	36.8	XRD	0.56	7.44	8	0.08	0.45	7	1.2
6H-5, 140–150	46.3	XRD	0.22	8.56	8.78	0.05	0.41	4.4	0.53
7H-5, 140–150	55.8	XRD	0.23	5.71	5.94	0.06	0.39	3.8	0.59
8H-5, 140–150	65.3	XRD	0.35	8.36	8.71	0.07	0.09	5	3.9
9H-5, 140–150	73.89	XRD	0.34	5.72	6.06	0.06	0.22	5.6	1.5
10H-5, 140–150	83.5	XRD	0.34	7.91	8.25	0.07	0.12	4.8	2.8
11H-5, 140–150	93.8	XRD	0.26	8.14	8.4	0.09	0.14	2.9	1.8
12X-3, 21–24	99.11	PP	0.31	5.6	5.91	0.07	0.24	4.4	1.3
13X-3, 16–17	108.86	PP	0.33	8.01	8.34	0.07	0.11	4.7	3
14X-4, 140–150	121.3	XRD	0.38	5	5.38	0.11	0.63	3.4	0.6
15X-3, 20–23	128.2	PP	0.47	4.14	4.61	0.1	0.18	4.7	2.6
16X-3, 20–23	137.8	PP	0.32	6.53	6.85	0.09	0.44	3.5	0.73
17X-5, 140–150	151.7	XRD	0.47	4.31	4.78	0.1	0.17	4.7	2.7
18X-3, 5–7	157.05	PP	0.43	7.17	7.6	0.1	0.1	4.3	4.3
19X-3, 5–6	166.75	PP	0.42	3.98	4.4	0.09	0.32	4.6	1.3
20X-3, 140–150	177.7	XRD	0.46	6.91	7.37	0.12	0.06	3.8	7.6
21X-3, 8–9	185.68	PP	0.43	5.82	6.25	0.1	0	4.3	
23X-2, 140–150	204.4	XRD	0.31	3.23	3.54	0.13	0.62	2.4	0.5
24X-3, 5–7	214.25	PP	0.58	5.56	6.14	0.1	0.14	5.8	4.1
25X-3, 6–8	223.96	PP	0.54	3.54	4.08	0.12	0.18	4.5	3
26X-3, 6–9	233.56	PP	0.34	5.48	5.82	0.09	0.23	3.8	1.5
27X-5, 140–150	247.14	XRD	0.3	3.55	3.85	0.09	0.24	3.3	1.2
28X-3, 4–6	252.84	PP	0.18	1.99	2.17	0.1	0.13	1.8	1.4
29X-5, 140–150	265.74	XRD	0.48	7.01	7.49	0.11	0.08	4.3	6
30X-3, 13–15	272.23	PP	0.61	4.19	4.8	0.11	0.12	5.5	5.1
31X-3, 45–47	281.31	PP	0.53	4.96	5.49	0.1	0.35	5.3	1.5
32X-4, 140–150	294.3	XRD	0.41	4.07	4.48	0.12	0.13	3.4	3.1
33X-3, 23–25	301.33	PP	0.39	6.25	6.64	0.09	0.51	4.3	0.76
34X-3, 20–23	311	PP	0.36	4.55	4.91	0.1	0.12	3.6	3
35X-4, 140–150	323.4	XRD	0.4	3.27	3.67	0.12	0.09	3.3	4.4
36X-3, 23–24	330.23	PP	0.25	7.15	7.4	0.08	0.1	3.1	2.5
37X-3, 20–22	339.16	PP	0.4	5.35	5.75	0.1	0.47	4	0.85
38X-4, 140–150	352.2	XRD	0.26	6.44	6.7	0.09	0.35	2.9	0.74
39X-3, 21–23	359.11	PP	0.5	4.9	5.4	0.11	0.69	4.5	0.72
40X-3, 20–23	368.7	PP	0.29	4.02	4.31	0.1	0.07	2.9	4.1
41X-3, 140–150	378.82	XRD	0.27	6.41	6.68	0.09	0.11	3	2.4
42X-3, 4–7	387.84	PP	0.25	5.5	5.75	0.09	0.99	2.8	0.25
43X-3, 5–7	397.55	PP	0.36	3.87	4.23	0.09	0.27	4	1.3
44X-4, 140–150	405.9	XRD	0.32	4.16	4.48	0.08	0.45	4	0.71
45X-3, 20–22	407.83	PP	0.23	6.06	6.29	0.06	0.32	3.8	0.72
46X-3, 20–22	417.42	PP	0.32	5.17	5.49	0.09	0.48	3.5	0.66
47X-4, 140–150	430.2	XRD	0.4	4.88	5.28	0.09	0.79	4.4	0.5

PP = physical properties sample; XRD = X-ray difraction sample.

about 300 mbsf. Variations in temperature rebound can probably be attributed to a decrease in circulation time at greater depths.

The temperature tool was run not to estimate heat flow, but in case fluid flow was present. In Figure 47, we present a plot of measured temperature as a function of pressure recorded simultaneously by this tool. Depths shown are approximate and may be revised by as much as 5 m after post-cruise merging of Schlumberger time/depth data with temperature-tool time/pressure data. Unlike previous temperature logging during Leg 133, temperature logging at Site 822 replaced the usual end sub with an aluminum go-devil 1 m long. A similar go-devil usually is dropped to fall freely through the pipe before logging begins to lock open the lockable flapper. Because we were considering deepening Hole 822A after logging, we could not leave a go-devil in the hole; thus, we used this go-devil end sub to open and close the lockable flapper. This go-devil had an adverse effect on our pressure log by creating pressure surges, which are evident in Figure 47 as high-frequency pressure noise. Normally, we did not run the temperature tool with the FMS during Leg 133 because of the risk of bending the tool. Our need for the go-devil compelled us to use the temperature tool with the FMS; although this short log (Fig. 47) has limited usefulness, no problems resulted.

The temperature pattern in Figure 47 exhibits evidence of thermal lags resulting from a mud-clogged end sub. Mud clogging can occur when the temperature tool, which is the bottom tool on the string, hits the bottom of a hole that contains sticky clay. The effect is a higher temperature for the upcoming log than that for the downgoing log, and a maximum temperature recording, not at the deepest point in the hole, but somewhat shallower than the deepest point on the upcoming log. When rigged down after logging, the temperature tool did encounter a mud-clogged end sub.

Downgoing logs probably were minimally affected by mud clogging. Their pattern is an approximately linear increase of temperature between the base of the pipe and the bottom of the hole. The extrapolated bottom-water temperature (based on observed sub-bottom thermal gradient) is substantially

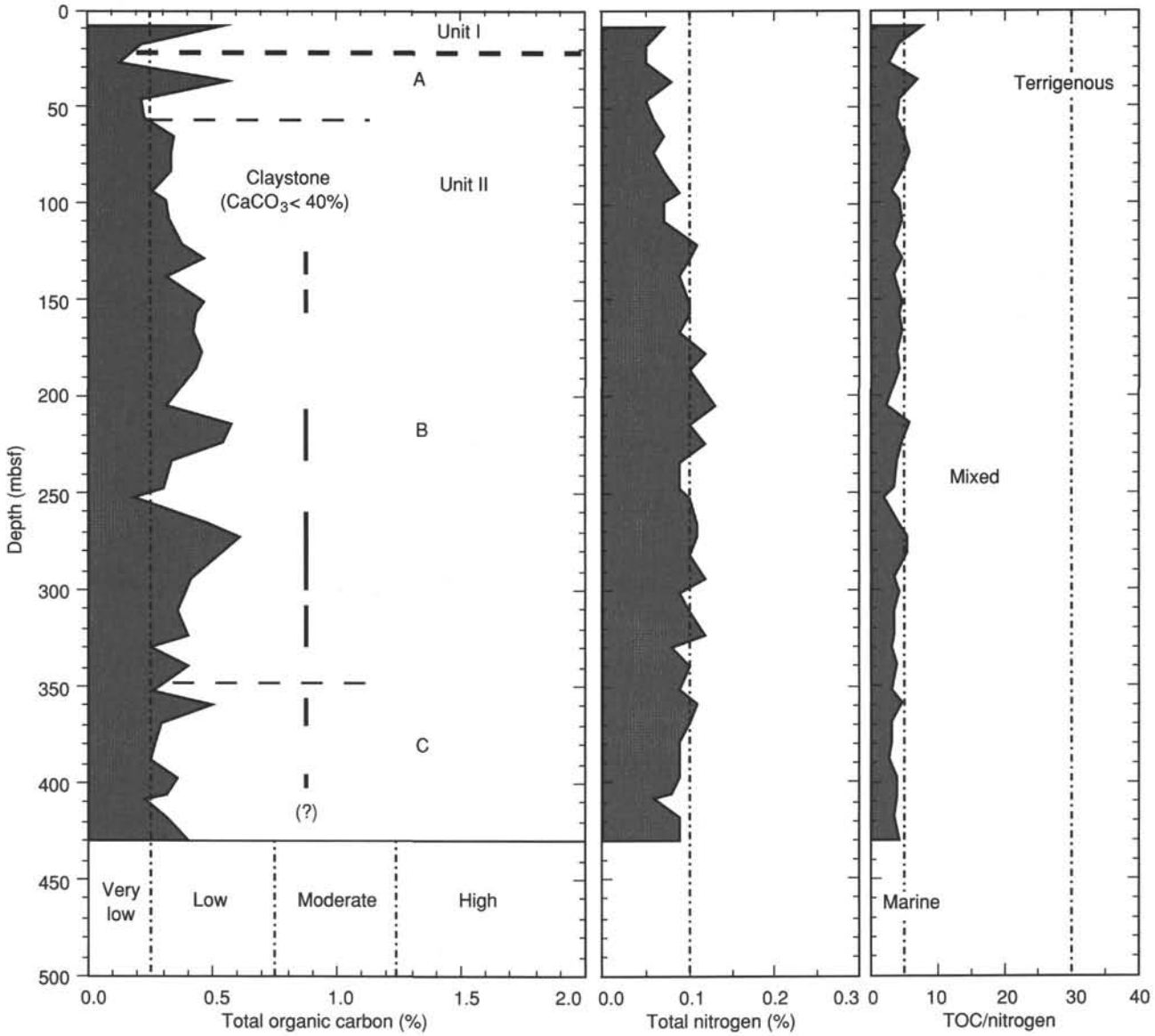

Figure 35. Distribution with depth of concentrations of total organic carbon and nitrogen and of TOC/nitrogen ratio at Site 822.

warmer than the observed bottom-water temperature (Fig. 47). This discrepancy may have been caused by either upward flux of pore fluids out of the formation or by bottom waters that currently are cooler than average; the latter scenario seems more likely in these relatively shallow waters.

SEISMIC STRATIGRAPHY

The BMR water-gun seismic profile collected during a 1987 site survey (Symonds and Davies, 1988; Feary et al., 1990) on a north-south strike line across Site 822 indicates that this hole is located on top of a mounded and channelled complex within the lower slope, adjacent to the Great Barrier Reef (Fig. 48). The section to about 0.2 s TWT below TD was subdivided into eight sequences, based on standard seismic stratigraphic procedures. Not all sequence boundaries displayed disconformable relationships in site-survey data, and in some cases, boundaries were based primarily on changes in reflection amplitude, reflection continuity, and changes in seismic character. We are not certain at this stage which sequence boundary has regional significance; however, one can see from site-survey data that some of those boundaries within the upper part of the section probably have been restricted to the lower-slope complex. These seismic sequences are briefly described next, as interpreted from BMR water-gun data–all time depths and thicknesses are two-way traveltime in seconds below the seafloor, as measured at the site.

Sequence 1

Sequence 1 extends from the seafloor down approximately 0.08 s and is uniform in thickness within the site area. The character of its upper part is largely disguised by interference with the seafloor reflection. However, where visible, it grades down from high-amplitude, discontinuous reflections to low-amplitude reflections toward its base (Fig. 48). The lower boundary of the sequence is an irregular broadly mounded surface that exhibits truncation of underlying reflectors, particularly on the flanks of the mound, and gentle onlap above. Sequence 1 basically drapes the underlying topography and caps the mound complex.

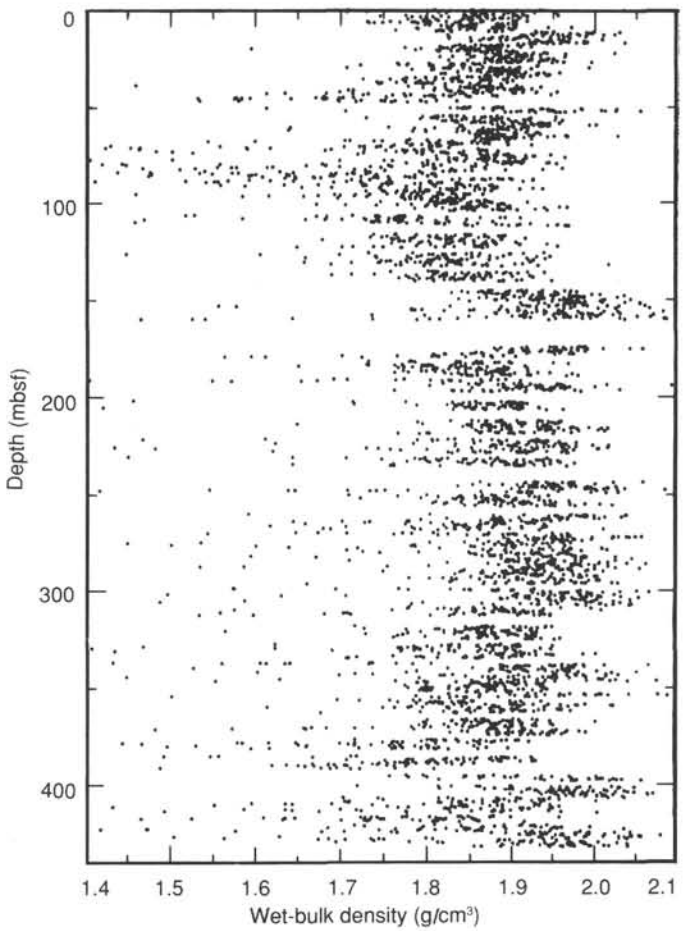

Figure 36. GRAPE bulk-density measurements for Site 822. Data values have been averaged at 5-cm intervals.

Sequence 2

Sequence 2 is approximately 0.09 s thick and is characterized by high-amplitude, wavy, parallel reflectors that become lower in amplitude and more discontinuous toward its base. Maximum thickness occurs within the main mound complex, which thins significantly on the flanks of the complex, where a chaotic, discontinuous reflection pattern is seen. This implies major variations in lateral facies within the sequence. Its lower boundary gently truncates reflectors below and is onlapped and downlapped above. Sequence 2 drapes the underlying topography.

Sequence 3

Sequence 3 is 0.06 s thick and is characterized by discontinuous, low-amplitude reflectors that form small overlapping mounds. This sequence may be totally constrained to the main mound complex and has created much of the relief that is draped by the overlying sequences (Fig. 48). Its lower boundary is conformable with reflectors below.

Sequence 4

Sequence 4 is 0.06 s thick and uniformly drapes the main mound to the south of Site 822. This consists of relatively high-amplitude, parallel to sub-parallel reflectors, with some zones of low-amplitude reflections. The sequence thickens off the main mound south of the site, and its internal configuration changes to low-amplitude, discontinuous reflections. Its lower boundary is generally conformable with underlying reflectors, but is onlapped by sequence 4 reflections on the flank of the main mound.

Sequence 5

Sequence 5 is 0.08 s thick at the site, but has a variable thickness throughout the slope complex. It is characterized by low-amplitude, slightly irregular reflections that fill in the channels on each side of the main mound. Its lower boundary is strongly onlapped and is normally conformable with reflectors below. Sequence 5 appears to thicken downslope into Queensland Trough, whereas the sequences above, and sequence 6 below, appear to thin in this direction.

Sequence 6

Sequence 6 is 0.09 s thick at the site, but thickens to 0.2 s to the south, where it forms the main mound. It has a low-amplitude, parallel to sub-parallel reflection character within the mound and becomes more irregular and chaotic along strike. Its lower boundary exhibits gentle downlapping above and, in some places, truncated reflections below.

Sequences 7 and 8

The top of sequence 7 lies just at or below TD. Sequences 7 and 8 are approximately 0.12 and 0.1 s thick, respectively, and both are uniform throughout the site area. They have similar characteristics that consist of zones of both high- and low-amplitude, subparallel, discontinuous reflections that ex-

hibit small-scale mounding and channelling. The lower boundaries of both sequences are relatively strong reflectors and generally are conformable with reflections above and below. Both sequences form a base to the mounded lower-slope complex and are significant regionally. They appear to thicken downslope into Queensland Trough.

The sequences just described form the uppermost part (0.7 s) of the sedimentary section in this area. Basement was not seen in water-gun data, but may be about 4 s below the seafloor in normal resolution air-gun data to the south of the site.

Correlation With Site 822 Lithostratigraphy

Correlation of logs with lithostratigraphy at Site 822 was based mainly on a depth match with a synthetic seismogram that we computed using *in-situ* velocity derived from a sonic log obtained from downhole logging. Because of our doubts concerning some of these density log data, we used a constant density to calculate acoustic impedance for the synthetic seismogram (see "Explanatory Notes" chapter, "Downhole Measurements" section, this volume, and "Downhole Measurements" section, this chapter, for details of how the synthetic seismograms were produced and for descriptions of relevant logs). In Figure 49, we summarize this correlation by showing seismic data from the site, the synthetic seismogram, and the velocity log, with its related depth scale, next to a summary of Site 822 lithostratigraphy. Considering the complexity of the site, a reasonable correlation exists between major reflectors in the seismic section and the synthetic seismogram.

Sequence 1 is approximately 50 m thick and correlates with lithologic Unit I, which is a clayey bioclastic nannofossil ooze of latest Pleistocene age (<0.93 Ma; nannofossil Zones CN15 and CN14a). We interpreted this as having been deposited at a time of low terrigenous influx.

Sequences 2 and 3 are approximately 100 and 50 m thick, respectively, and together correspond with Unit IIA. This is a clayey to silty mixed sediment of Pleistocene age (0.93–1.48 MA; nannofossil Zone CN13b). This unit has a more quartz-rich upper section that corresponds with seismic sequence 2, and sequence 3 appears to correspond with thicker claystone units. The mounded facies within these sequences are thought to be slumps, levees, or some other localized build-up of redeposited sediment that have been blanketed by terrigenous-dominated sediments.

Sequences 4 and 5 are approximately 55 and 70 m thick, respectively, and correlate with Unit IIB, which is a calcareous claystone and clayey-to-silty nannofossil mixed sediments of Pleistocene to latest Pliocene age (0.93–1.88 Ma; nannofossil Zones CN13b and CN13a). No major change in lithology has been ascribed to the base of sequence 4; however, it may be related to thicker claystone units. Both sequences have been interpreted as terrigenous-dominated sediments that have filled in an abandoned erosional channel.

Sequence 6 lies beyond the limit of our synthetic seismogram, but by extrapolating depths to TD we observed that it is approximately 100 m thick and corresponds with basal Subunit IIC. This unit comprises chalky, silty nannofossil mixed sediments of late Pliocene age (1.88–3.5 Ma; nannofossil Zones CN12d to CN12a). Probably, the base of sequence 6 lies just below TD, based on this interpretation. Deposition of this sequence has been interpreted as relating to a period of lower terrigenous influx, while later erosion of the unit formed a mounded erosional remnant.

Overall seismic geometries of the site agree well with our lithostratigraphic interpretation that the muddy lower slope was incised by gullies and canyons, while the sediments were eroded from canyon walls and transported into the adjacent Queensland Trough as slumps and debris flows (see "Lithostratigraphy" section, this chapter). Seismic data indicate that this process was not as prevalent in pre-late Pliocene time, because sequences below TD exhibit much less mounding and erosion.

SUMMARY AND CONCLUSIONS

Overview

Site 822 was located on a complex channelized lower-slope deposit east of Great Barrier Reef. Seismic profiles tie this lower-slope site to those three sites comprising the upper-slope transect (Sites 819–821) in Grafton Passage. Site 822 was selected for studying sedimentation processes on the lower slope of the continental margin and to determine ages and composition of sedimentary units that are correlatable to seismic reflectors imaged within the deposit. Drilling yielded uppermost Pliocene (> 2.6 Ma) to Pleistocene sediments, which provide a record of sedimentation in front of the Great Barrier Reef that is approximately 1 Ma longer than the record recovered along the upper-slope transect. Based on initial shipboard results, a preliminary sedimentation history consistent with data gathered at Sites 819 through 821 evolved.

Sedimentation History

Sediments recovered at Site 822 are mixed carbonate and siliciclastic deposits similar in composition to those deposited at Sites 819 through 821. Systematic variations in the percentage of carbonate and grain size of the siliciclastic component separate the sequence into distinct units. Changes in physical properties of sediments produced by these variations permit a potential correlation of the sedimentary units with reflectors in seismic profiles across the lower slope.

At the base of the cored section, the uppermost Pliocene sediments are rich in silt- and sand-size quartz particles. Redeposited bioclasts are common. The overlying lower Pleistocene sediments are characterized by a finer-grained siliciclastic component, whereas the middle Pleistocene sediments contain relatively more silt- and sand-size quartz particles. The record has been interrupted by a hiatus between 275,000 and 465,000 yr. The uppermost Pleistocene sediments are clayey bioclastic ooze relatively enriched in carbonate over terrigenous influxes, perhaps reflecting the influence of active carbonate production on the Great Barrier Reef.

Sedimentation rates were high throughout the sequence, while rates for the early to middle Pleistocene were about five times greater (about 40 cm/k.y.) than those calculated for sediments deposited during the late Pliocene and late Pleistocene. We calculated equally high middle Pleistocene sedimentation rates for all three sites on the upper-slope transect. A common cause for this phenomenon probably is related to increased terrigenous influx, induced by changes in climate during this period.

In summary, the excellent recovery and biostratigraphic control at Site 822 will aid in delineating a detailed late Pliocene/Pleistocene record of paleoenvironmental changes that occurred offshore the Great Barrier Reef. This record can then be correlated to the equally complete stratigraphic sequences on the upper-slope transect (Sites 819–821) in Grafton Passage. This integrated record derived from data obtained at all four sites will be used to evaluate various factors that influenced the evolution of the Great Barrier

Table 7. Index properties data for Site 822.

Core, section, interval (cm)	Depth (mbsf)	Bulk density (g/cm^3)	Grain density (g/cm^3)	Porosity (%)	Water content (%)	Void ratio
133-822A-						
2H-1, 97–100	1.87	1.75	2.76	60.1	54.2	1.50
2H-2, 97–100	3.37	1.77	2.85	58.8	51.4	1.43
2H-3, 97–100	4.87	1.72	2.73	62.8	59.9	1.69
2H-4, 97–100	6.37	1.65	2.82	67.6	72.7	2.09
2H-5, 97–100	7.87	1.73	2.79	60.4	55.4	1.52
2H-6, 97–100	9.37	1.75	2.86	61.5	56.5	1.60
3H-1, 22–25	10.62	1.74	2.62	61.3	56.7	1.59
3H-2, 22–25	12.12	1.91	2.82	54.1	41.0	1.18
3H-3, 22–25	13.62	1.82	2.73	55.3	45.1	1.24
3H-4, 22–25	15.12	1.87	2.83	66.6	57.6	1.99
3H-6, 22–25	18.12	1.76	2.81	57.3	49.9	1.34
3H-7, 16–19	19.56	1.76	2.77	62.3	57.1	1.66
4H-1, 16–19	20.06	1.76	2.78	59.4	53.0	1.46
4H-2, 16–19	21.56	1.79	2.74	55.7	46.8	1.26
4H-3, 16–19	23.06	1.85	2.82	59.9	49.9	1.50
4H-4, 16–19	24.56	1.78	2.82	58.5	50.9	1.41
4H-5, 16–19	26.06	1.83	2.76	56.0	45.7	1.27
4H-6, 16–19	27.56	1.80	2.76	58.7	50.1	1.42
4H-7, 16–19	29.06	1.84	2.79	57.0	46.5	1.33
5H-1, 16–19	29.56	1.86	2.82	54.1	42.3	1.18
5H-2, 16–19	31.06	1.82	2.78	58.2	48.6	1.40
5H-3, 16–19	32.56	1.83	2.79	56.0	45.6	1.27
5H-4, 16–19	34.06	1.86	2.75	55.1	43.6	1.23
5H-5, 16–19	35.56	1.93	2.77	56.8	43.3	1.31
5H-6, 16–19	37.06	1.80	2.70	57.1	48.1	1.33
5H-7, 16–19	38.56	1.83	2.70	57.1	47.0	1.33
6H-1, 20–23	39.10	1.80	2.77	57.6	48.9	1.36
6H-2, 20–23	40.60	1.84	2.77	55.9	45.2	1.27
6H-3, 20–23	42.10	1.87	2.75	53.3	41.3	1.14
6H-4, 20–23	43.60	1.84	2.79	56.6	45.9	1.30
6H-5, 20–23	45.10	1.81	2.80	54.4	44.6	1.20
6H-6, 20–23	46.60	1.85	2.80	55.9	44.8	1.27
7H-1, 20–23	48.60	1.84	2.80	55.4	44.6	1.24
7H-2, 20–23	50.10	1.83	2.70	56.1	45.9	1.28
7H-3, 20–23	51.60	1.94	2.78	49.3	35.1	0.97
7H-4, 20–23	53.10	1.87	2.79	53.7	41.8	1.16
7H-5, 20–23	54.60	1.89	2.76	51.0	38.2	1.04
7H-6, 20–23	56.10	1.93	2.79	49.2	35.5	0.97
7H-7, 20–23	57.60	1.93	2.78	51.0	37.1	1.04
8H-1, 20–23	58.10	1.88	2.63	51.5	38.9	1.06
8H-2, 20–23	59.60	1.83	2.92	53.4	42.7	1.15
8H-3, 20–23	61.10	1.85	2.63	54.6	43.2	1.20
8H-4, 20–23	62.60	1.84	2.77	51.6	40.2	1.07
8H-5, 20–23	64.10	1.90	2.73	50.9	37.7	1.04
8H-6, 20–23	65.60	1.91	2.80	50.3	36.9	1.01
8H-7, 20–23	67.10	1.90	2.80	52.9	39.9	1.12
9H-1, 20–23	67.60	1.92	2.87	59.5	46.5	1.47
9H-2, 20–23	68.19	1.81	2.83	55.8	46.2	1.26
9H-3, 20–23	69.69	1.83	2.79	55.7	45.4	1.26
9H-4, 20–23	71.19	1.85	2.64	54.8	43.5	1.21
9H-5, 20–23	72.69	1.89	2.59	53.4	40.7	1.15
9H-6, 20–23	74.19	1.92	2.82	49.7	36.0	0.99
9H-7, 20–23	75.69	1.86	2.73	50.1	38.1	1.00
10H-1, 20–22	77.10	1.87	2.77	53.3	41.1	1.14
9H-8, 20–23	77.19	1.89	2.85	53.5	40.9	1.15
10H-2, 20–22	77.80	1.91	2.81	52.2	38.8	1.09
10H-3, 20–22	79.30	1.86	2.74	53.9	42.2	1.17
10H-4, 20–22	80.80	1.83	2.76	51.2	40.1	1.05
10H-5, 20–22	82.30	1.87	2.76	49.0	36.6	0.96
10H-6, 20–22	83.80	1.92	2.77	51.3	37.7	1.05
10H-7, 20–22	85.30	1.92	2.74	50.9	37.4	1.04
11H-1, 20–22	86.60	1.88	2.80	52.3	39.8	1.10
10H-8, 20–22	86.80	1.93	2.77	50.7	36.9	1.03
11H-2, 20–22	88.10	1.90	2.80	51.0	37.8	1.04
11H-3, 20–22	89.60	1.89	2.68	52.4	39.7	1.10
11H-4, 20–22	91.10	1.87	2.78	52.7	40.5	1.12
11H-5, 20–22	92.60	1.89	2.75	51.8	39.0	1.07
11H-6, 20–22	94.10	1.92	2.77	51.1	37.3	1.04
11H-7, 20–22	95.60	1.93	2.75	49.3	35.6	0.97
12X-1, 28–31	96.18	1.91	2.77	55.8	42.6	1.26
12X-2, 20–23	97.60	1.87	2.74	54.8	42.9	1.21
12X-3, 20–23	99.10	1.87	2.79	53.8	41.8	1.16
12X-4, 21–24	100.61	1.89	2.72	52.7	39.9	1.12
12X-5, 20–23	102.10	1.89	2.71	51.0	38.1	1.04
13X-1, 20–23	105.90	1.83	2.72	56.2	45.9	1.29
13X-2, 27–29	107.47	1.84	2.77	55.1	44.3	1.23
13X-3, 19–22	108.89	1.89	2.74	54.2	41.6	1.18
13X-4, 20–23	110.40	1.93	2.78	49.6	35.6	0.98
13X-5, 20–23	111.50	1.96	2.76	47.4	32.9	0.90

Table 7 (continued).

Core, section, interval (cm)	Depth (mbsf)	Bulk density (g/cm^3)	Grain density (g/cm^3)	Porosity (%)	Water content (%)	Void ratio
14X-1, 20–23	115.60	1.84	2.75	54.4	43.5	1.19
14X-2, 20–23	117.10	1.87	2.73	51.4	39.1	1.06
14X-3, 20–23	118.60	1.91	2.74	51.9	38.7	1.08
14X-4, 20–23	120.10	1.91	2.77	50.9	37.7	1.04
14X-5, 20–23	121.60	1.94	2.75	48.0	33.8	0.92
15X-1, 14–16	125.14	1.99	2.64	48.6	33.4	0.95
15X-2, 20–23	126.70	1.91	2.73	50.2	37.0	1.01
15X-3, 20–23	128.20	1.87	2.74	53.3	41.3	1.14
15X-4, 20–23	129.70	1.93	2.72	50.2	36.4	1.01
15X-5, 20–23	131.20	1.95	2.74	49.8	35.4	0.99
16X-1, 46–49	135.06	1.86	2.77	50.6	38.7	1.03
16X-2, 20–22	136.30	1.81	2.76	56.3	46.6	1.29
16X-3, 20–22	137.80	1.92	2.80	53.9	40.5	1.17
16X-4, 20–22	139.30	1.94	2.73	52.8	38.6	1.12
17X-1, 14–17	144.44	2.02	2.78	44.9	29.4	0.81
17X-2, 14–17	145.94	2.00	2.77	45.3	30.3	0.83
17X-3, 14–17	147.44	1.96	2.73	45.0	30.8	0.82
17X-4, 14–17	148.94	1.98	2.71	47.9	32.8	0.92
17X-5, 14–17	150.44	2.03	2.72	44.9	29.3	0.81
17X-6, 14–17	151.94	2.04	2.77	44.0	28.4	0.79
18X-1, 17–18	154.17	2.03	2.83	48.6	32.4	0.94
18X-2, 5–7	155.55	2.00	2.71	49.7	34.1	0.99
18X-3, 5–7	157.05	2.08	2.76	47.6	30.7	0.91
18X-4, 5–7	158.55	2.08	2.78	43.1	26.9	0.76
19X-1, 28–29	163.98	1.95	2.73	48.1	33.7	0.93
19X-2, 6–7	165.26	1.99	2.71	52.2	36.8	1.09
19X-3, 5–6	166.75	1.99	2.76	47.9	32.7	0.92
19X-4, 6–7	168.26	1.81	2.82	48.5	37.8	0.94
20X-1, 5–7	173.35	2.03	2.67	46.2	30.5	0.86
20X-2, 5–7	174.85	2.13	2.63	54.5	35.6	1.20
20X-3, 5–7	176.35	1.97	2.79	51.4	36.4	1.06
20X-4, 5–7	177.85	1.97	2.78	50.0	35.2	1.00
20X-5, 5–7	179.35	1.92	2.74	51.9	38.2	1.08
20X-6, 5–7	180.85	1.98	2.68	51.1	35.9	1.05
21X-1, 18–19	182.78	1.87	2.70	52.5	40.5	1.11
21X-2, 8–9	184.18	1.90	2.81	50.9	37.8	1.04
21X-3, 8–9	185.68	1.91	2.84	53.1	39.8	1.13
21X-4, 8–9	187.18	1.96	2.69	48.8	34.3	0.95
21X-5, 8–9	188.68	1.89	2.68	52.7	40.1	1.12
21X-6, 8–9	190.18	1.92	2.73	51.4	37.7	1.06
23X-1, 8–9	201.58	1.93	2.80	44.5	31.0	0.80
23X-2, 8–9	203.08	1.97	2.71	50.1	35.3	1.00
23X-3, 8–9	204.58	1.94	2.79	52.2	37.9	1.09
24X-1, 5–7	211.25	1.84	2.80	50.2	38.9	1.01
24X-2, 5–7	212.75	1.99	2.77	49.5	34.2	0.98
24X-3, 5–7	214.25	2.07	2.71	49.5	32.5	0.98
24X-4, 5–7	215.75	1.96	2.79	51.1	36.4	1.04
24X-5, 5–7	217.25	1.97	2.79	48.6	33.9	0.95
25X-1, 6–8	220.96	2.03	2.81	47.4	31.4	0.90
25X-2, 6–8	222.46	2.03	2.69	50.8	34.6	1.03
25X-3, 6–8	223.96	1.98	2.76	51.4	36.2	1.06
25X-4, 6–8	225.46	2.01	2.79	47.7	32.0	0.91
25X-5, 6–8	226.96	1.86	2.77	46.7	34.6	0.88
25X-6, 6–8	228.46	1.95	2.77	51.4	37.0	1.06
26X-1, 23–25	230.73	1.99	2.72	51.6	36.2	1.07
26X-2, 5–7	232.05	1.88	2.75	52.3	39.9	1.10
26X-3, 5–7	233.55	1.90	2.78	45.5	32.5	0.84
26X-4, 5–7	235.05	1.99	2.78	47.3	32.2	0.90
27X-1, 4–6	240.24	2.03	2.80	45.3	29.6	0.83
27X-2, 4–6	241.28	1.97	2.80	48.2	33.4	0.93
27X-3, 4–6	242.78	2.01	2.77	48.2	32.6	0.93
27X-4, 4–6	244.28	2.04	2.76	47.4	31.3	0.90
27X-5, 4–6	245.78	2.05	2.72	42.8	27.2	0.75
27X-6, 4–6	247.28	2.00	2.80	44.1	29.1	0.79
28X-1, 4–6	249.84	1.97	2.76	48.7	33.8	0.95
28X-2, 4–6	251.34	2.03	2.78	45.0	29.4	0.82
28X-3, 4–6	252.84	1.95	2.79	47.2	32.9	0.90
28X-4, 4–6	254.34	1.99	2.76	49.7	34.5	0.99
29X-2, 15–18	259.99	1.97	2.76	47.5	32.9	0.90
29X-3, 15–18	261.49	2.06	2.73	48.1	31.4	0.93
29X-4, 15–18	262.99	1.95	2.88	51.3	36.8	1.05
29X-5, 15–18	264.49	1.93	2.79	49.1	35.3	0.97
29X-6, 15–18	265.99	1.95	2.78	49.3	34.8	0.97
29X-7, 15–18	267.49	1.97	2.70	47.2	32.6	0.90
30X-1, 12–15	269.22	1.97	2.75	46.6	31.9	0.87
30X-2, 12–15	270.72	2.02	2.78	44.5	29.1	0.80
30X-3, 12–15	272.22	1.97	2.80	45.1	30.6	0.82
30X-4, 12–15	273.72	2.00	2.70	47.6	32.3	0.91
30X-5, 12–15	275.22	1.94	2.76	46.5	32.6	0.87
30X-6, 12–15	276.72	1.95	2.79	50.3	36.0	1.01

Table 7 (continued).

Core, section, interval (cm)	Depth (mbsf)	Bulk density (g/cm^3)	Grain density (g/cm^3)	Porosity (%)	Water content (%)	Void ratio
30X-7, 12–15	278.22	1.95	2.82	50.9	36.4	1.04
31X-1, 45–47	279.25	2.05	2.77	44.8	28.7	0.81
31X-2, 45–47	279.81	1.96	2.71	45.0	30.7	0.82
31X-3, 45–47	281.31	2.01	2.76	42.5	27.6	0.74
31X-4, 45–47	282.81	2.06	2.83	43.3	27.5	0.77
31X-5, 45–47	284.31	2.09	2.77	45.7	28.8	0.84
31X-6, 45–47	285.81	2.05	2.80	41.6	26.2	0.71
31X-7, 45–47	287.31	2.00	2.78	45.0	30.0	0.82
32X-1, 19–21	288.59	2.05	2.81	42.3	26.8	0.73
32X-2, 19–21	290.09	2.05	2.74	43.2	27.5	0.76
32X-3, 19–21	291.59	2.00	2.80	44.5	29.6	0.80
32X-4, 19–21	293.09	2.00	2.82	44.9	29.8	0.81
32X-5, 19–21	294.59	2.03	2.78	43.9	28.5	0.78
33X-1, 20–22	298.30	2.04	2.71	45.1	29.3	0.82
33X-2, 20–22	299.80	2.02	2.80	42.2	27.2	0.73
33X-3, 23–25	301.33	1.99	2.74	46.6	31.5	0.87
33X-4, 20–22	302.80	2.07	2.78	41.8	26.0	0.72
33X-5, 20–22	304.30	2.02	2.78	44.7	29.4	0.81
33X-6, 20–22	305.80	2.02	2.78	45.3	29.8	0.83
33X-7, 20–22	307.30	2.03	2.97	45.5	29.8	0.84
34X-1, 20–22	308.00	2.01	2.80	45.0	29.7	0.82
34X-2, 20–22	309.50	1.94	2.80	49.0	34.8	0.96
34X-3, 20–22	311.00	2.00	2.76	48.1	32.7	0.93
34X-4, 20–22	312.50	2.02	2.80	44.3	29.0	0.80
35X-1, 33–35	317.83	1.92	2.76	49.2	35.6	0.97
35X-2, 33–35	319.33	1.95	2.79	47.6	33.4	0.91
35X-3, 33–35	320.83	1.98	2.81	48.5	33.6	0.94
35X-4, 33–35	322.33	2.00	2.84	46.8	31.4	0.88
35X-5, 33–35	323.83	1.93	2.79	47.6	33.7	0.91
36X-1, 23–25	327.23	1.98	2.62	45.9	31.0	0.85
36X-2, 24–26	328.74	1.96	2.79	49.4	34.9	0.98
36X-3, 23–25	330.23	1.90	2.79	46.7	33.6	0.88
36X-4, 23–25	331.73	1.97	2.82	46.3	31.8	0.86
36X-5, 23–25	333.23	2.02	2.75	45.0	29.4	0.82
36X-6, 23–25	334.73	2.02	2.82	45.6	30.0	0.84
37X-1, 21–23	336.81	2.01	2.83	44.3	29.1	0.80
37X-2, 21–23	337.67	1.98	2.75	44.6	30.0	0.81
37X-3, 21–23	339.17	1.98	2.77	45.4	30.6	0.83
37X-4, 21–23	340.67	2.03	2.74	45.6	29.9	0.83
37X-5, 21–23	342.17	2.13	2.82	39.8	23.7	0.66
37X-6, 21–23	343.67	2.05	2.78	44.6	28.6	0.80
37X-7, 21–23	345.17	2.09	2.78	40.9	25.0	0.69
38X-1, 21–23	346.51	2.04	2.76	46.4	30.4	0.86
38X-2, 21–23	348.01	1.91	2.83	46.1	32.9	0.86
38X-3, 21–23	349.51	2.01	2.80	49.7	33.8	0.99
38X-4, 21–23	351.01	1.99	2.74	47.6	32.4	0.91
38X-5, 21–23	352.51	1.80	2.78	56.7	47.8	1.31
38X-6, 21–23	354.01	1.92	2.78	44.6	31.3	0.80
39X-1, 21–23	356.11	1.96	2.78	48.7	34.1	0.95
39X-2, 21–23	357.61	1.91	2.76	47.0	33.7	0.89
39X-3, 21–23	359.11	2.01	2.76	46.3	30.9	0.86
39X-4, 21–23	360.61	1.98	2.82	47.9	33.0	0.92
39X-5, 21–23	362.11	1.95	2.81	47.7	33.4	0.91
40X-1, 20–23	365.70	2.04	2.76	54.5	37.9	1.20
40X-2, 20–23	367.20	2.08	2.70	49.1	32.0	0.97
40X-3, 20–23	368.70	2.08	2.80	48.9	31.7	0.96
40X-4, 20–23	370.20	2.01	2.74	53.4	37.3	1.15
40X-5, 20–23	371.70	2.07	2.75	49.6	32.4	0.98
40X-6, 20–23	373.20	2.07	2.72	46.2	29.8	0.86
41X-1, 5–7	375.15	2.03	2.72	48.7	32.6	0.95
41X-2, 5–7	375.97	1.87	2.73	51.9	39.6	1.08
41X-3, 5–7	377.47	1.98	2.74	51.4	36.2	1.06
41X-4, 5–7	378.97	1.90	2.63	51.0	37.9	1.04
41X-5, 5–7	380.47	1.85	2.74	55.5	44.3	1.25
42X-1, 5–7	384.85	1.87	2.72	53.3	41.3	1.14
42X-2, 5–7	386.35	1.90	2.68	49.6	36.3	0.98
42X-3, 5–7	387.85	1.84	2.80	51.8	40.6	1.08
42X-4, 5–7	389.35	1.93	2.79	52.9	39.1	1.12
42X-5, 5–7	390.85	1.91	2.72	49.7	36.4	0.99
42X-6, 5–7	392.35	2.02	2.77	47.2	31.5	0.89
43X-1, 5–7	394.55	2.01	2.80	48.1	32.5	0.93
43X-2, 5–7	396.05	1.98	2.80	47.3	32.3	0.90
43X-3, 5–7	397.55	2.14	2.70	42.6	25.6	0.74
43X-4, 5–7	399.05	2.01	2.75	47.4	31.9	0.90
44X-1, 20–22	400.20	2.09	2.70	41.3	25.3	0.70
44X-2, 20–22	401.70	2.10	2.72	41.3	25.2	0.71

Table 7 (continued).

Core, section, interval (cm)	Depth (mbsf)	Bulk density (g/cm^3)	Grain density (g/cm^3)	Porosity (%)	Water content (%)	Void ratio
44X-3, 20–22	403.20	2.13	2.74	37.9	22.3	0.61
44X-4, 20–22	404.70	2.11	2.80	36.8	21.7	0.58
45X-1, 20–22	405.10	2.04	2.81	42.2	26.9	0.73
44X-5, 20–22	406.20	2.11	2.83	39.8	24.0	0.66
45X-2, 20–22	406.33	2.09	2.79	39.7	24.1	0.66
45X-3, 20–22	407.83	2.07	2.82	44.3	28.1	0.80
45X-4, 20–22	409.33	2.05	2.80	42.4	26.9	0.74
45X-5, 20–22	410.83	2.03	2.74	42.9	27.6	0.75
45X-6, 20–22	412.33	1.97	2.75	48.7	33.9	0.95
45X-7, 20–22	413.83	2.06	2.81	44.6	28.5	0.81
46X-1, 20–22	414.80	2.05	2.75	43.9	28.0	0.78
46X-2, 20–22	415.92	1.98	2.86	47.0	32.2	0.89
46X-3, 20–22	417.42	1.98	2.72	49.6	34.6	0.99
46X-4, 20–22	418.92	1.96	2.79	48.0	33.4	0.92
46X-5, 20–22	420.42	2.03	2.76	44.3	28.8	0.80
46X-6, 20–22	421.92	1.98	2.76	42.6	28.3	0.74
47X-1, 17–20	424.47	2.15	2.73	44.2	26.6	0.79
47X-2, 17–20	425.97	2.35	2.76	33.3	17.0	0.50
47X-3, 17–20	427.47	2.19	2.75	38.0	21.6	0.61
47X-4, 17–20	428.97	2.08	2.77	43.2	27.0	0.76
47X-5, 17–20	430.47	2.12	2.71	45.8	28.4	0.84
47X-6, 17–20	431.97	2.15	2.66	43.1	25.8	0.76
47X-7, 17–20	433.20	2.22	2.79	42.6	24.5	0.74

Table 8. Compressional wave velocity data for Site 822.

Core, section, interval (cm)	Depth (mbsf)	Distance (mm)	Traveltime (μs)	Velocity (m/s)
133-822A-				
2H-1, 97–100	1.87	29.72	21.56	1554
2H-2, 97–100	3.37	30.50	21.90	1568
2H-3, 97–100	4.87	29.70	21.66	1545
2H-4, 97–100	6.37	30.46	22.48	1518
2H-5, 97–100	7.87	30.13	21.86	1551
2H-6, 97–100	9.37	29.72	21.70	1542
3H-1, 22–25	10.62	29.78	21.52	1561
3H-2, 22–25	12.12	29.53	20.78	1613
3H-3, 22–25	13.62	30.38	21.62	1586
3H-4, 22–25	15.12	29.99	21.52	1573
3H-5, 22–25	16.62	29.50	20.78	1611
3H-6, 22–25	18.12	29.59	21.30	1570
3H-7, 22–25	19.62	28.90	21.03	1554
4H-1, 16–19	20.06	29.37	21.21	1565
4H-2, 16–19	21.56	30.03	21.81	1550
4H-3, 16–19	23.06	29.73	21.31	1577
4H-4, 16–19	24.56	29.60	21.32	1568
4H-5, 16–19	26.06	30.77	21.69	1601
4H-6, 16–19	27.56	29.60	21.63	1542
5H-1, 16–19	29.56	29.74	21.84	1532
5H-2, 16–19	31.06	30.08	21.54	1576

Reef. In particular, Site 822 can provide information about environmental conditions that preceded the initiation of reef development in the central region of the Great Barrier Reef. From shore-based studies combining biostratigraphy, magnetostratigraphy, and chemostratigraphy, valuable criteria will be obtained for understanding the influence of fluctuations in climate and sea level on redeposited sediments in a mixed carbonate-siliciclastic system. This information will help us to define parameters that produce the seismic reflectors and sedimentary geometries in seismic profiles taken across the slopes east of the Great Barrier Reef and will aid in interpreting the record of eustatic sea levels stored in these profiles.

REFERENCES

Baker, P. A., and Kastner, M., 1981. Constraints on the formation of sedimentary dolomites. *Science,* 213:214–216.

Feary, D. A., Pigram, C. J., Davies, P. J., Symonds, P. A., Droxler, A. W., and Peerdeman, F., 1990. Ocean Drilling Program–Leg 133 safety package. *Bur. Miner. Res. Aust. Rec.,* 1990/6.

Hamilton, E. L., 1979. Sound velocity gradients in marine sediments. *J. Acoust. Soc. Am.,* 65:909–922.

Read, J. F., 1984. Carbonate platform facies models. *AAPG Bull.,* 69:1–21.

Swart, P. K., and Guzikowski, M., 1988. Interstitial-water chemistry and diagenesis of periplatform sediments from the Bahamas, ODP Leg 101. *In* Austin, J. A., Jr., Schlager, W., et al., *Proc. ODP, Sci. Results,* 101: College Station, TX (Ocean Drilling Program), 363–380.

Symonds, P. A., and Davies, P. J., 1988. Structure, stratigraphy, evolution and regional framework of the Townsville Trough and Marion Plateau region–research cruise proposal, project 9131.11. *Bur. Miner. Res. Aust. Rec.,* 1988/48.

van Morkhoven, F.P.C.M., Berggren, W. A., Edwards. A. S., et al., 1986. Cenozoic cosmopolitan deep-water benthic foraminifera. *Bull. Cent. Rech. Explor.-Prod. Elf Aquitaine,* Mem. 11.

Ms 133-115

NOTE: All core description forms ("barrel sheets") and core photographs have been printed on coated paper and bound separately as Part 2 of this volume, beginning on page 813.

Formation microscanner images for this site are presented on microfiche in the back of Part 2.

Table 9. Electrical-resistivity formation factor data for Hole 822A.

Core, section, interval (cm)	Depth (mbsf)	Seawater (ohms)	Sample (ohms)	Formation factor
133-822A-				
2H-1, 20–20	1.10	2.6	8.6	3.31
2H-1, 70–70	1.60	2.6	9.1	3.50
2H-1, 120–120	2.10	2.6	9.1	3.50
2H-2, 20–20	2.60	2.6	10.3	3.96
2H-2, 70–70	3.10	2.6	9.7	3.73
2H-2, 120–120	3.60	2.6	10.0	3.85
2H-3, 20–20	4.10	2.6	9.6	3.69
2H-3, 70–70	4.60	2.6	8.8	3.38
2H-3, 120–120	5.10	2.6	8.9	3.42
2H-4, 20–20	5.60	2.6	8.4	3.23
2H-4, 70–70	6.10	2.6	7.5	2.88
2H-4, 120–120	6.60	2.6	7.2	2.77
2H-5, 20–20	7.10	2.6	8.7	3.35
2H-5, 70–70	7.60	2.6	8.8	3.38
2H-5, 120–120	8.10	2.6	8.9	3.42
2H-6, 20–20	8.60	2.6	9.1	3.50
2H-6, 70–70	9.10	2.6	10.2	3.92
2H-6, 120–120	9.60	2.6	8.2	3.15
3H-1, 20–20	10.60	2.6	10.0	3.85
3H-1, 70–70	11.10	2.6	10.0	3.85
3H-1, 120–120	11.60	2.6	11.1	4.27
3H-2, 20–20	12.10	2.6	10.6	4.08
3H-2, 70–70	12.60	2.6	10.4	4.00
3H-2, 120–120	13.10	2.6	10.3	3.96
3H-3, 20–20	13.60	2.6	9.8	3.77
3H-3, 70–70	14.10	2.6	9.9	3.81
3H-3, 120–120	14.60	2.6	10.4	4.00
3H-4, 20–20	15.10	2.6	10.4	4.00
3H-4, 70–70	15.60	2.6	9.6	3.69
3H-4, 120–120	16.10	2.6	11.4	4.38
3H-5, 20–20	16.60	2.6	10.2	3.92
3H-5, 70–70	17.10	2.6	10.3	3.96
3H-6, 20–20	18.10	2.6	10.0	3.85
3H-6, 70–70	18.60	2.6	9.4	3.62
3H-6, 120–120	19.10	2.6	8.8	3.38
4H-1, 20–20	20.10	2.6	9.1	3.50
4H-1, 70–70	20.60	2.6	7.2	2.77
4H-1, 120–120	21.10	2.6	9.0	3.46
4H-2, 20–20	21.60	2.6	8.7	3.35
4H-2, 70–70	22.10	2.6	9.9	3.81
4H-2, 120–120	22.60	2.6	9.7	3.73
4H-3, 20–20	23.10	2.6	10.4	4.00
4H-3, 70–70	23.60	2.6	9.7	3.73
4H-3, 120–120	24.10	2.6	9.8	3.77
4H-4, 20–20	24.60	2.6	10.1	3.88
4H-4, 70–70	25.10	2.6	10.1	3.88
4H-4, 120–120	25.60	2.6	9.6	3.69
4H-5, 20–20	26.10	2.6	12.7	4.88
4H-5, 70–70	26.60	2.6	12.8	4.92
4H-5, 120–120	27.10	2.6	10.1	3.88
4H-6, 20–20	27.60	2.6	9.6	3.69
4H-6, 70–70	28.10	2.6	12.6	4.85
4H-6, 120–120	28.60	2.6	10.7	4.12
5H-1, 20–20	29.60	2.6	10.3	3.96
5H-1, 70–70	30.10	2.6	9.8	3.77
5H-1, 120–120	30.60	2.6	9.6	3.69
5H-2, 20–20	31.10	2.6	9.6	3.69
5H-2, 70–70	31.60	2.6	9.8	3.77
5H-2, 120–120	32.10	2.6	9.6	3.69
5H-3, 20–20	32.60	2.6	9.8	3.77
5H-3, 70–70	33.10	2.6	10.6	4.08
5H-3, 120–120	33.60	2.6	10.5	4.04
5H-4, 20–20	34.10	2.6	10.8	4.15
5H-4, 70–70	34.60	2.6	11.7	4.50
5H-4, 120–120	35.10	2.6	11.0	4.23
5H-5, 20–20	35.60	2.6	14.2	5.46
5H-5, 70–70	36.10	2.6	11.8	4.54
5H-5, 120–120	36.60	2.6	12.5	4.81
5H-6, 20–20	37.10	2.6	14.2	5.46
5H-6, 70–70	37.60	2.6	12.5	4.81
5H-6, 120–120	38.10	2.6	11.8	4.54
6H-1, 30–30	39.20	2.6	9.8	3.77
6H-1, 70–70	39.60	2.6	10.7	4.12
6H-1, 120–120	40.10	2.6	11.4	4.38

Table 9 (continued).

Core, section, interval (cm)	Depth (mbsf)	Seawater (ohms)	Sample (ohms)	Formation factor
6H-2, 20–20	40.60	2.6	11.9	4.58
6H-2, 70–70	41.10	2.6	11.7	4.50
6H-2, 120–120	41.60	2.6	13.7	5.27
6H-3, 20–20	42.10	2.6	12.7	4.88
6H-3, 70–70	42.60	2.6	11.6	4.46
6H-3, 120–120	43.10	2.6	12.4	4.77
6H-4, 20–20	43.60	2.6	11.1	4.27
6H-4, 70–70	44.10	2.6	11.4	4.38
6H-4, 120–120	44.60	2.6	13.3	5.12
6H-5, 20–20	45.10	2.6	15.1	5.81
6H-5, 70–70	45.60	2.6	14.1	5.42
6H-6, 20–20	46.60	2.6	10.6	4.08
6H-6, 70–70	47.10	2.6	15.4	5.92
6H-6, 110–110	47.50	2.6	11.0	4.23
7H-1, 20–20	48.60	2.6	10.3	3.96
7H-1, 70–70	49.10	2.6	10.0	3.85
7H-1, 120–120	49.60	2.6	12.7	4.88
7H-2, 20–20	50.10	2.6	12.6	4.85
7H-2, 70–70	50.60	2.6	9.6	3.69
7H-2, 120–120	51.10	2.6	13.0	5.00
7H-3, 20–20	51.60	2.6	13.1	5.04
7H-3, 70–70	52.10	2.6	13.4	5.15
7H-3, 120–120	52.60	2.6	11.9	4.58
7H-4, 20–20	53.10	2.6	12.9	4.96
7H-4, 70–70	53.60	2.6	15.8	6.08
7H-4, 120–120	54.10	2.6	18.8	7.23
7H-5, 20–20	54.60	2.6	17.6	6.77
7H-5, 70–70	55.10	2.6	14.0	5.38
7H-5, 120–120	55.60	2.6	13.9	5.35
7H-6, 20–20	56.10	2.6	15.0	5.77
7H-6, 70–70	56.60	2.6	19.3	7.42
7H-6, 120–120	57.10	2.6	19.2	7.38
8H-1, 20–20	58.10	2.6	11.8	4.54
8H-1, 70–70	58.60	2.6	11.5	4.42
8H-1, 120–120	59.10	2.6	11.6	4.46
8H-2, 20–20	59.60	2.6	11.0	4.23
8H-2, 70–70	60.10	2.6	11.0	4.23
8H-2, 120–120	60.60	2.6	12.9	4.96
8H-3, 20–20	61.10	2.6	11.7	4.50
8H-3, 70–70	61.60	2.6	11.9	4.58
8H-3, 120–120	62.10	2.6	13.3	5.12
8H-4, 20–20	62.60	2.6	15.8	6.08
8H-4, 70–70	63.10	2.6	12.2	4.69
8H-4, 120–120	63.60	2.6	12.2	4.69
8H-5, 20–20	64.10	2.6	12.9	4.96
8H-5, 70–70	64.60	2.6	13.2	5.08
8H-6, 20–20	65.60	2.6	14.1	5.42
8H-6, 70–70	66.10	2.6	13.5	5.19
8H-6, 120–120	66.60	2.6	15.6	6.00
9H-1, 20–20	67.60	2.6	12.2	4.69
9H-2, 20–20	68.19	2.6	10.3	3.96
9H-2, 70–70	68.69	2.6	9.8	3.77
9H-2, 120–120	69.19	2.6	10.0	3.85
9H-3, 20–20	69.69	2.6	13.8	5.31
9H-3, 70–70	70.19	2.6	12.6	4.85
9H-3, 120–120	70.69	2.6	13.4	5.15
9H-4, 20–20	71.19	2.6	16.4	6.31
9H-4, 74–74	71.73	2.6	15.6	6.00
9H-4, 120–120	72.19	2.6	13.4	5.15
9H-5, 20–20	72.69	2.6	15.2	5.85
9H-5, 70–70	73.19	2.6	16.3	6.27
9H-5, 120–120	73.69	2.6	14.2	5.46
9H-6, 18–18	74.17	2.6	15.9	6.12
9H-6, 70–70	74.69	2.6	15.3	5.88
9H-6, 120–120	75.19	2.6	13.6	5.23
9H-7, 20–20	75.69	2.6	13.5	5.19
9H-7, 70–70	76.19	2.6	14.1	5.41
9H-7, 120–120	76.69	2.6	15.4	5.92
10H-1, 20–20	77.10	2.6	15.1	5.81
9H-8, 20–20	77.19	2.6	15.6	6.00
9H-8, 73–73	77.72	2.6	13.5	5.19
10H-2, 20–20	77.80	2.6	11.8	4.54
10H-2, 70–70	78.30	2.6	10.3	3.96
10H-2, 120–120	78.80	2.6	10.8	4.15
10H-3, 20–20	79.30	2.6	11.1	4.27
10H-3, 75–75	79.85	2.6	13.3	5.12
10H-3, 124–124	80.34	2.6	11.5	4.42

Table 9 (continued).

Core, section, interval (cm)	Depth (mbsf)	Seawater (ohms)	Sample (ohms)	Formation factor
10H-4, 20–20	80.80	2.6	11.9	4.58
10H-4, 70–70	81.30	2.6	12.3	4.73
10H-4, 120–120	81.80	2.6	12.6	4.85
10H-5, 20–20	82.30	2.6	12.5	4.81
10H-5, 60–60	82.70	2.6	11.4	4.38
10H-5, 120–120	83.30	2.6	11.1	4.27
11H-1, 20–20	86.60	2.6	13.1	5.04
11H-1, 70–70	87.10	2.6	11.6	4.46
11H-1, 123–123	87.63	2.6	14.9	5.73
11H-2, 20–20	88.10	2.6	17.1	6.58
11H-2, 70–70	88.60	2.6	15.9	6.12
11H-2, 120–120	89.10	2.6	15.9	6.12
11H-3, 20–20	89.60	2.6	16.1	6.19
11H-3, 70–70	90.10	2.6	18.6	7.15
11H-3, 123–123	90.63	2.6	20.7	7.96
11H-4, 20–20	91.10	2.6	13.0	5.00
11H-4, 70–70	91.60	2.6	18.7	7.19
11H-4, 120–120	92.10	2.6	12.4	4.77
11H-5, 20–20	92.60	2.6	14.5	5.58
11H-5, 70–70	93.10	2.6	16.6	6.38
11H-5, 110–110	93.50	2.6	15.7	6.04
11H-6, 20–20	94.10	2.6	16.6	6.38
11H-6, 70–70	94.60	2.6	17.0	6.54
11H-6, 120–120	95.10	2.6	18.8	7.23
11H-7, 20–20	96.10	2.6	15.1	5.81
12X-1, 20–20	96.10	2.6	10.1	3.88
12X-1, 70–70	96.60	2.6	10.2	3.92
12X-1, 120–120	97.10	2.6	9.8	3.77
12X-2, 20–20	97.60	2.6	9.9	3.81
12X-2, 70–70	98.10	2.6	11.3	4.35
12X-2, 120–120	98.60	2.6	10.0	3.85
12X-3, 20–20	99.10	2.6	12.3	4.73
12X-3, 70–70	99.60	2.6	12.1	4.65
12X-3, 115–115	100.05	2.6	11.2	4.31
12X-4, 30–30	100.70	2.6	11.4	4.38
12X-4, 70–70	101.10	2.6	14.6	5.62
12X-4, 120–120	101.60	2.6	11.6	4.46
12X-5, 20–20	102.10	2.6	13.6	5.23
12X-5, 70–70	102.60	2.6	17.4	6.69
12X-5, 120–120	103.10	2.6	11.9	4.58
13X-1, 20–20	105.90	2.6	9.7	3.73
13X-1, 70–70	106.40	2.6	11.9	4.58
13X-1, 120–120	106.90	2.6	12.6	4.85
13X-4, 20–20	110.40	2.6	12.0	4.62
13X-4, 70–70	110.90	2.6	12.5	4.81
13X-5, 20–20	111.50	2.6	17.3	6.65
13X-5, 70–70	112.00	2.6	14.0	5.38
13X-5, 120–120	112.50	2.6	18.1	6.96
14X-1, 20–20	115.60	2.6	13.8	5.31
14X-1, 70–70	116.10	2.6	11.2	4.31
14X-1, 120–120	116.60	2.6	11.2	4.31
14X-2, 20–20	117.10	2.6	11.8	4.54
14X-2, 70–70	117.60	2.6	12.3	4.73
14X-2, 120–120	118.10	2.6	12.8	4.92
14X-3, 20–20	118.60	2.6	11.7	4.50
14X-3, 70–70	119.10	2.6	13.2	5.08
14X-3, 120–120	119.60	2.6	12.5	4.81
14X-4, 20–20	120.10	2.6	14.9	5.73
14X-4, 70–70	120.60	2.6	12.5	4.81
14X-4, 110–110	121.00	2.6	13.0	5.00
14X-5, 20–20	121.60	2.6	16.9	6.50
14X-5, 70–70	122.10	2.6	12.0	4.62
14X-5, 110–110	122.50	2.6	12.9	4.96
15X-1, 20–20	125.20	2.6	12.9	4.96
15X-1, 70–70	125.70	2.6	12.9	4.96
15X-1, 110–110	126.10	2.6	11.6	4.46
15X-2, 20–20	126.70	2.6	12.3	4.73
15X-2, 70–70	127.20	2.6	13.1	5.04
15X-2, 120–120	127.70	2.6	11.6	4.46
15X-3, 20–20	128.20	2.6	11.7	4.50
15X-3, 70–70	128.70	2.6	11.5	4.42
15X-3, 120–120	129.20	2.6	12.2	4.69
15X-4, 20–20	129.70	2.6	13.0	5.00
15X-4, 70–70	130.20	2.6	13.2	5.08
15X-4, 120–120	130.70	2.6	12.3	4.73
15X-5, 20–20	131.20	2.6	12.9	4.96
15X-5, 70–70	131.70	2.6	13.1	5.04

Table 9 (continued).

Core, section, interval (cm)	Depth (mbsf)	Seawater (ohms)	Sample (ohms)	Formation factor
16X-1, 20–20	134.80	2.6	10.9	4.19
16X-1, 70–70	135.30	2.6	11.9	4.58
16X-1, 120–120	135.80	2.6	12.6	4.85
16X-2, 45–45	136.55	2.6	12.4	4.77
16X-2, 77–77	136.87	2.6	14.1	5.42
16X-2, 124–124	137.34	2.6	13.9	5.35
16X-3, 20–20	137.80	2.6	13.8	5.31
16X-3, 120–120	138.80	2.6	12.4	4.77
16X-4, 20–20	139.30	2.6	11.1	4.27
17X-1, 20–20	144.50	2.6	16.1	6.19
17X-1, 70–70	145.00	2.6	14.0	5.38
17X-1, 120–120	145.50	2.6	16.3	6.27
17X-2, 20–20	146.00	2.6	15.9	6.12
17X-2, 70–70	146.50	2.6	14.8	5.69
17X-2, 120–120	147.00	2.6	15.2	5.85
17X-3, 20–20	147.50	2.6	13.5	5.19
17X-3, 70–70	148.00	2.6	16.6	6.38
17X-3, 120–120	148.50	2.6	14.7	5.65
17X-4, 20–20	149.00	2.6	13.1	5.04
17X-4, 70–70	149.50	2.6	16.3	6.27
17X-4, 120–120	150.00	2.6	14.4	5.54
17X-5, 20–20	150.50	2.6	16.4	6.31
17X-5, 70–70	151.00	2.6	14.8	5.69
17X-6, 20–20	152.00	2.6	16.0	6.15
17X-6, 70–70	152.50	2.6	18.3	7.04
17X-6, 120–120	153.00	2.6	19.1	7.35
18X-1, 20–20	154.20	2.6	10.7	4.12
18X-1, 70–70	154.70	2.6	17.3	6.65
18X-1, 125–125	155.25	2.6	14.2	5.46
18X-2, 20–20	155.70	2.6	19.2	7.38
18X-2, 70–70	156.20	2.6	13.9	5.35
18X-2, 120–120	156.70	2.6	15.3	5.88
18X-3, 20–20	157.20	2.6	13.2	5.08
18X-3, 75–75	157.75	2.6	17.7	6.81
18X-3, 125–125	158.25	2.6	19.9	7.65
18X-4, 20–20	158.70	2.6	14.5	5.58
18X-4, 70–70	159.20	2.6	18.6	7.15
18X-4, 120–120	159.70	2.6	15.6	6.00
19X-1, 20–20	163.90	2.6	12.8	4.92
19X-1, 70–70	164.40	2.6	13.5	5.19
19X-1, 120–120	164.90	2.6	11.4	4.38
19X-2, 15–15	165.36	2.6	15.1	5.81
19X-2, 70–70	165.90	2.6	14.1	5.42
19X-2, 120–120	166.40	2.6	16.3	6.27
19X-3, 20–20	166.90	2.6	13.7	5.27
19X-3, 70–70	167.40	2.6	12.5	4.81
19X-3, 125–125	167.95	2.6	11.2	4.31
19X-4, 20–20	168.40	2.6	11.8	4.54
19X-4, 70–70	168.90	2.6	11.9	4.58
19X-4, 120–120	169.40	2.6	14.1	5.42
20X-1, 20–20	173.50	2.6	15.1	5.81
20X-1, 70–70	174.00	2.6	14.0	5.38
20X-1, 120–120	174.50	2.6	14.1	5.42
20X-2, 20–20	175.00	2.6	13.4	5.15
20X-2, 70–70	175.50	2.6	13.0	5.00
20X-2, 120–120	176.00	2.6	14.2	5.46
20X-3, 20–20	176.50	2.6	12.6	4.85
20X-3, 70–70	177.00	2.6	14.8	5.69
20X-3, 110–110	177.40	2.6	14.8	5.69
20X-4, 20–20	178.00	2.6	14.4	5.54
20X-4, 70–70	178.50	2.6	11.7	4.50
20X-4, 120–120	179.00	2.6	11.5	4.42
20X-5, 20–20	179.50	2.6	16.0	6.15
20X-5, 70–70	180.00	2.6	13.0	5.00
20X-6, 20–20	181.00	2.6	12.3	4.73
20X-6, 70–70	181.50	2.6	12.2	4.69
20X-6, 120–120	182.00	2.6	12.6	4.85
21X-1, 20–20	182.80	2.6	15.4	5.92
21X-1, 70–70	183.30	2.6	12.0	4.62
21X-1, 120–120	183.80	2.6	11.3	4.35
21X-2, 20–20	184.30	2.6	13.8	5.31
21X-2, 70–70	184.80	2.6	12.3	4.73
21X-2, 120–120	185.30	2.6	11.3	4.35
21X-3, 20–20	185.80	2.6	9.7	3.73
21X-3, 70–70	186.30	2.6	10.4	4.00
21X-3, 120–120	186.80	2.6	10.5	4.04
21X-4, 20–20	187.30	2.6	12.0	4.62

Table 9 (continued).

Core, section, interval (cm)	Depth (mbsf)	Seawater (ohms)	Sample (ohms)	Formation factor
21X-4, 70–70	187.80	2.6	10.9	4.19
21X-4, 120–120	188.30	2.6	13.3	5.12
21X-5, 120–120	189.80	2.6	12.3	4.73
21X-6, 20–20	190.30	2.6	13.6	5.23
21X-6, 70–70	190.80	2.6	13.4	5.15
21X-6, 130–130	191.40	2.6	10.6	4.08
22X-1, 20–20	192.40	2.6	12.4	4.77
22X-1, 70–70	192.90	2.6	12.7	4.88
22X-1, 120–120	193.40	2.6	14.2	5.46
22X-2, 20–20	193.90	2.6	15.1	5.81
22X-2, 70–70	194.40	2.6	16.8	6.46
22X-2, 120–120	194.90	2.6	12.5	4.81
22X-3, 20–20	195.40	2.6	12.8	4.92
22X-3, 70–70	195.90	2.6	17.2	6.62
22X-3, 120–120	196.40	2.6	13.5	5.19
23X-1, 20–20	201.70	2.6	12.2	4.69
23X-1, 70–70	202.20	2.6	14.4	5.54
23X-1, 120–120	202.70	2.6	11.4	4.38
23X-2, 20–20	203.20	2.6	11.1	4.27
23X-2, 70–70	203.70	2.6	11.4	4.38
23X-2, 120–120	204.20	2.6	11.6	4.46
23X-3, 20–20	204.70	2.6	15.4	5.92
23X-3, 70–70	205.20	2.6	12.6	4.85
23X-3, 120–120	205.70	2.6	11.7	4.50
24X-1, 20–20	211.40	2.6	11.0	4.23
24X-1, 70–70	211.90	2.6	19.9	7.65
24X-1, 120–120	212.40	2.6	17.3	6.65
24X-2, 20–20	212.90	2.6	19.2	7.38
24X-2, 70–70	213.40	2.6	14.3	5.50
24X-2, 120–120	213.90	2.6	19.4	7.46
24X-3, 20–20	214.40	2.6	24.5	9.42
24X-3, 70–70	214.90	2.6	14.3	5.50
24X-3, 120–120	215.40	2.6	13.7	5.27
24X-4, 70–70	216.40	2.6	12.4	4.77
24X-4, 120–120	216.90	2.6	12.6	4.85
24X-5, 20–20	217.40	2.6	17.9	6.88
24X-5, 70–70	217.90	2.6	12.2	4.69
24X-5, 120–120	218.40	2.6	15.3	5.88
25X-1, 20–20	221.10	2.6	11.4	4.38
25X-1, 70–70	221.60	2.6	17.6	6.77
25X-1, 120–120	222.10	2.6	15.4	5.92
25X-2, 20–20	222.60	2.6	14.8	5.69
25X-2, 70–70	223.10	2.6	15.1	5.81
25X-2, 120–120	223.60	2.6	14.2	5.46
25X-3, 20–20	224.10	2.6	17.6	6.77
25X-3, 70–70	224.60	2.6	13.0	5.00
25X-3, 120–120	225.10	2.6	13.6	5.23
25X-4, 20–20	225.60	2.6	12.8	4.92
25X-4, 70–70	226.10	2.6	17.1	6.58
25X-4, 120–120	226.60	2.6	19.9	7.65
25X-5, 20–20	227.10	2.6	15.9	6.12
25X-5, 70–70	227.60	2.6	17.4	6.69
25X-5, 120–120	228.10	2.6	12.9	4.96
26X-1, 20–20	230.70	2.6	9.8	3.77
26X-1, 120–120	231.70	2.6	14.4	5.54
26X-2, 20–20	232.20	2.6	12.7	4.88
26X-2, 70–70	232.70	2.6	12.5	4.81
26X-2, 120–120	233.20	2.6	12.5	4.81
26X-3, 70–70	234.20	2.6	15.2	5.85
26X-3, 120–120	234.70	2.6	20.0	7.69
26X-4, 20–20	235.20	2.6	20.0	7.69
27X-1, 20–20	240.40	2.6	18.7	7.19
27X-1, 75–75	240.95	2.6	14.5	5.58
27X-2, 20–20	241.44	2.6	14.6	5.62
27X-2, 70–70	241.94	2.6	13.7	5.27
27X-2, 120–120	242.44	2.6	23.8	9.15
27X-3, 20–20	242.94	2.6	12.0	4.62
27X-3, 70–70	243.44	2.6	14.6	5.62
27X-3, 120–120	243.94	2.6	12.6	4.85
27X-4, 20–20	244.44	2.6	16.5	6.35
27X-4, 70–70	244.94	2.6	13.8	5.31

Table 9 (continued).

Core, section, interval (cm)	Depth (mbsf)	Seawater (ohms)	Sample (ohms)	Formation factor
27X-4, 120–120	245.44	2.6	15.0	5.77
27X-5, 20–20	245.94	2.6	16.4	6.31
27X-5, 70–70	246.44	2.6	19.4	7.46
27X-5, 120–120	246.94	2.6	13.8	5.31
27X-6, 20–20	247.44	2.6	13.8	5.31
27X-6, 70–70	247.94	2.6	14.7	5.65
27X-6, 120–120	248.44	2.6	15.0	5.77
28X-1, 20–20	250.00	2.6	18.2	7.00
28X-1, 120–120	251.00	2.6	20.5	7.88
28X-2, 20–20	251.50	2.6	19.9	7.65
28X-2, 70–70	252.00	2.6	20.7	7.96
28X-2, 120–120	252.50	2.6	21.0	8.08
28X-3, 20–20	253.00	2.6	16.0	6.15
28X-3, 70–70	253.50	2.6	17.5	6.73
28X-3, 120–120	254.00	2.6	17.8	6.85
28X-4, 20–20	254.50	2.6	21.2	8.15
28X-4, 70–70	255.00	2.6	15.7	6.04
28X-4, 120–120	255.50	2.6	19.3	7.42
29X-2, 20–20	260.04	2.6	14.2	5.46
29X-2, 70–70	260.54	2.6	19.1	7.35
29X-2, 120–120	261.04	2.6	22.9	8.81
29X-3, 20–20	261.54	2.6	19.8	7.62
29X-3, 70–70	262.04	2.6	19.4	7.46
29X-3, 120–120	262.54	2.6	14.3	5.50
29X-4, 20–20	263.04	2.6	13.5	5.19
29X-4, 70–70	263.54	2.6	14.9	5.73
29X-4, 120–120	264.04	2.6	17.8	6.85
29X-5, 20–20	264.54	2.6	23.0	8.85
29X-5, 70–70	265.04	2.6	14.9	5.73
29X-5, 120–120	265.54	2.6	13.9	5.35
29X-6, 20–20	266.04	2.6	19.0	7.31
29X-6, 70–70	266.54	2.6	14.0	5.38
29X-6, 120–120	267.04	2.6	13.2	5.08
30X-1, 20–20	269.30	2.6	14.2	5.46
30X-1, 70–70	269.80	2.6	19.8	7.62
30X-1, 120–120	270.30	2.6	16.4	6.31
30X-2, 20–20	270.80	2.6	16.8	6.46
30X-2, 70–70	271.30	2.6	18.0	6.92
30X-2, 120–120	271.80	2.6	17.6	6.77
30X-3, 20–20	272.30	2.6	19.3	7.42
30X-3, 70–70	272.80	2.6	16.9	6.50
30X-4, 20–20	273.80	2.6	19.0	7.31
30X-4, 70–70	274.30	2.6	16.9	6.50
30X-4, 120–120	274.80	2.6	19.2	7.38
30X-5, 70–70	275.80	2.6	13.6	5.23
30X-5, 120–120	276.30	2.6	22.0	8.46
30X-6, 20–20	276.80	2.6	12.6	4.85
31X-2, 20–20	279.56	2.6	16.0	6.15
31X-2, 55–55	279.91	2.6	13.8	5.31
31X-2, 100–100	280.36	2.6	15.6	6.00
31X-3, 20–20	281.06	2.6	13.0	5.00
31X-3, 70–70	281.56	2.6	17.6	6.77
31X-3, 100–100	281.86	2.6	16.5	6.35
31X-4, 20–20	282.56	2.6	15.6	6.00
31X-4, 70–70	283.06	2.6	20.5	7.88
31X-4, 130–130	283.66	2.6	22.0	8.46
31X-5, 20–20	284.06	2.6	16.5	6.35
31X-5, 70–70	284.56	2.6	16.5	6.35
31X-5, 140–140	285.26	2.6	13.9	5.35
31X-6, 20–20	285.56	2.6	12.0	4.62
31X-6, 70–70	286.06	2.6	16.8	6.46
31X-6, 130–130	286.66	2.6	18.3	7.04
31X-7, 20–20	287.06	2.6	17.4	6.69
31X-7, 70–70	287.56	2.6	18.3	7.04
31X-7, 130–130	288.16	2.6	18.1	6.96
32X-1, 30–30	288.70	2.6	16.6	6.38
32X-1, 72–72	289.12	2.6	22.1	8.50
32X-1, 120–120	289.60	2.6	18.0	6.92
32X-2, 20–20	290.10	2.6	21.2	8.15
32X-2, 73–73	290.63	2.6	14.8	5.69
32X-2, 120–120	291.10	2.6	16.8	6.46

Table 10. Vane shear strength data for Hole 822A.

Core, section, interval (cm)	Depth (mbsf)	Spring number	Torque (degrees)	Strain (degrees)	Shear strength (kPa)
133-822A-					
2H-1, 96–97	1.86	4	8	8	9.5
2H-2, 96–97	3.36	2	24	17	11.3
2H-3, 96–97	4.86	2	19	10	8.9
2H-4, 96–97	6.36	2	20	11	9.4
2H-5, 96–97	7.86	2	32	16	15.1
2H-6, 96–97	9.36	2	20	14	9.4
3H-1, 96–97	11.36	2	80	22	37.6
3H-2, 96–97	12.86	2	87	17	40.9
3H-3, 96–97	14.36	2	72	15	33.9
3H-4, 96–97	15.86	2	94	15	44.2
3H-5, 96–97	17.36	2	42	17	19.8
3H-6, 96–97	18.86	2	55	17	25.9
4H-1, 96–97	20.86	2	55	13	25.9
4H-2, 96–97	22.36	2	99	21	46.6
4H-3, 96–97	23.86	2	51	16	24.0
4H-4, 96–97	25.36	2	59	19	27.8
4H-5, 96–97	26.86	2	57	16	26.8
4H-6, 96–97	28.36	2	36	15	16.9
5H-1, 98–99	30.38	2	67	17	31.5
5H-2, 98–99	31.88	2	38	20	17.9
5H-3, 98–99	33.38	2	35	11	16.5
5H-4, 98–99	34.88	2	39	14	18.4
5H-5, 98–99	36.38	2	62	25	29.2
5H-6, 98–99	37.88	2	75	19	35.3
6H-1, 98–99	39.88	2	91	20	42.8
6H-2, 98–99	41.38	2	42	10	19.8
6H-3, 86–87	42.76	2	36	18	16.9
6H-4, 98–99	44.38	2	40	22	18.8
6H-6, 105–106	47.45	2	36	28	16.9
7H-1, 98–99	49.38	2	67	17	31.5
7H-2, 92–93	50.82	4	47	13	55.9
7H-3, 98–99	52.38	4	31	17	36.9
7H-4, 98–99	53.88	4	25	15	29.7
7H-5, 88–89	55.28	4	28	14	33.3
7H-6, 98–99	56.88	4	31	16	36.9
8H-1, 98–99	58.88	4	51	15	60.7
8H-2, 98–99	60.38	4	54	17	64.2
8H-3, 88–89	61.78	4	34	14	40.4
8H-4, 98–99	63.38	4	25	18	29.7
8H-5, 98–99	64.88	4	34	15	40.4
8H-6, 98–99	66.38	4	32	18	38.1
9H-1, 28–29	67.68	4	33	16	39.2
9H-2, 98–99	68.97	4	51	18	60.7
9H-3, 93–94	70.42	4	17	14	20.2
9H-4, 98–99	71.97	4	33	15	39.2
9H-5, 98–99	73.47	4	40	14	47.6
9H-6, 98–99	74.97	4	45	15	53.5
9H-7, 98–99	76.47	4	45	16	53.5
10H-1, 43–44	77.33	4	45	17	53.5
10H-2, 98–99	78.58	4	57	16	67.8
10H-3, 98–99	80.08	4	46	15	54.7
10H-4, 100–101	81.60	4	49	17	58.3
10H-5, 90–91	83.00	4	30	17	35.7
11H-1, 98–99	87.38	4	72	14	85.6
11H-2, 98–99	88.88	4	48	12	57.1
11H-3, 98–99	90.38	4	44	11	52.3
11H-4, 93–94	91.83	4	51	16	60.7
11H-5, 93–94	93.33	4	32	14	38.1
11H-6, 98–99	94.88	4	26	14	30.9
12X-1, 98–99	96.88	4	25	13	29.7
12X-2, 98–99	98.38	4	33	13	39.2
12X-3, 98–99	99.88	4	25	14	29.7
12X-4, 99–100	101.39	4	33	13	39.2
12X-5, 99–100	102.89	4	35	11	41.6
13X-4, 84–85	111.04	4	61	18	72.5

Table 11. Thermal conductivity data for Site 822.

Core, section, interval (cm)	Depth (mbsf)	Probe number	Thermal conductivity (W/m·K)	Standard error (W/m·K)	Calculated drift (W/m·K)
133-822A-					
2H-2, 70–70	3.10	32	1.0346	0.00328	-0.00763
2H-3, 70–70	4.60	3	1.0986	0.00470	0.00696
2H-5, 70–70	7.60	5	1.0967	0.00540	0.03852
2H-6, 70–70	9.10	150	1.0684	0.00398	-0.00037
3H-2, 60–60	12.50	32	0.9835	0.00616	0.02991
3H-3, 60–60	14.00	3	1.0875	0.00722	-0.00792
3H-5, 60–60	17.00	5	1.0044	0.00740	0.05621
3H-6, 60–60	18.50	150	1.0829	0.00653	0.00333
5H-2, 40–40	31.30	32	0.9439	0.01177	-0.03198
5H-3, 40–40	32.80	3	1.1197	0.01276	0.03483
5H-5, 40–40	35.80	5	1.1298	0.00588	0.07672
5H-6, 40–40	37.30	150	1.0563	0.00342	0.00938
7H-2, 49–49	50.39	32	0.9256	0.00154	-0.02231
7H-3, 34–34	51.74	3	1.1361	0.00531	-0.00009
7H-5, 51–51	54.91	5	1.2266	0.00609	0.05015
7H-6, 63–63	56.53	150	1.0634	0.00531	-0.00596
8H-2, 48–48	59.88	32	0.9770	0.00577	-0.01971
8H-3, 44–44	61.34	3	1.0708	0.00465	0.00629
8H-5, 54–54	64.44	5	1.2065	0.00531	0.05399
8H-6, 54–54	65.94	150	1.0454	0.00451	0.01451
9H-2, 43–43	68.42	32	1.0215	0.00439	-0.01422
9H-2, 43–43	68.42	32	1.0215	0.00439	-0.01422
9H-3, 30–30	69.79	3	0.9905	0.00746	-0.02117
9H-3, 30–30	69.79	3	0.9905	0.00746	-0.02117
9H-5, 53–53	73.02	5	0.9886	0.00563	0.02375
9H-5, 53–53	73.02	5	0.9886	0.00563	0.02375
9H-6, 62–62	74.61	150	1.0090	0.00503	-0.00227
9H-6, 62–62	74.61	150	1.0090	0.00503	-0.00227
10H-2, 53–53	78.13	32	1.0499	0.00529	-0.02278
10H-3, 30–30	79.40	3	0.9963	0.00490	-0.02301
10H-5, 79–79	82.89	5	0.8850	0.00330	0.00616
10H-6, 46–46	84.06	150	0.8608	0.00521	0.01744
11H-2, 38–38	88.28	32	0.9686	0.00499	-0.01647
11H-3, 51–51	89.91	3	0.9944	0.00541	-0.00419
11H-5, 51–51	92.91	5	1.0144	0.00382	0.04230
11H-6, 50–50	94.40	150	0.9069	0.00551	-0.00020
12X-2, 53–53	97.93	32	0.9396	0.00383	-0.03852
12X-3, 53–53	99.43	3	1.0960	0.00687	-0.00694
12X-5, 34–34	102.24	5	1.0992	0.00582	0.03803
12X-6, 19–19	103.59	150	0.8876	0.00635	-0.04093
13X-2, 60–60	107.80	32	1.0209	0.00623	0.00056
13X-3, 60–60	109.30	3	1.0880	0.00504	0.00594
13X-4, 60–60	110.80	5	1.1734	0.00635	0.03444
14X-2, 37–37	117.27	32	1.0338	0.00760	-0.00912
14X-3, 53–53	118.93	3	1.0123	0.00695	0.00654
14X-4, 35–35	120.25	5	0.9303	0.00618	-0.01248
14X-5, 26–26	121.66	150	0.9860	0.00559	-0.02172
15X-2, 27–27	126.77	32	0.9933	0.00376	-0.03124
15X-3, 52–52	128.52	3	0.8552	0.00581	-0.06128
15X-4, 50–50	130.00	150	1.0743	0.00330	-0.01662
15X-5, 80–80	131.80	5	0.9360	0.00361	-0.00720
16X-1, 46–46	135.06	32	1.0563	0.00446	-0.00558
16X-2, 26–26	136.36	3	1.0193	0.00619	0.00082
16X-3, 128–128	138.88	5	1.0941	0.00384	0.03679
16X-4, 45–45	139.55	150	1.1258	0.00526	-0.00015
17X-2, 60–60	146.40	32	1.0895	0.00322	-0.02546
17X-3, 60–60	147.90	3	1.2728	0.00453	0.02424
17X-4, 60–60	149.40	5	1.1622	0.00342	0.01186
17X-5, 60–60	150.90	150	1.1903	0.00297	0.00093
18X-4, 70–70	159.20	32	1.2869	0.00530	0.01559
19X-4, 69–69	168.89	3	1.1483	0.00502	-0.00427
20X-2, 80–80	175.60	5	1.0978	0.00489	0.03026
20X-6, 81–81	181.61	150	1.1250	0.00472	0.02096
21X-2, 92–92	185.02	32	1.0236	0.00369	-0.02096
22X-1, 94–94	193.14	3	1.1400	0.00540	0.00470
22X-2, 75–75	194.45	150	1.1587	0.00482	0.00862
23X-1, 31–31	201.81	5	1.1142	0.00639	0.03636
24X-2, 11–11	212.81	32	1.0945	0.00365	-0.02000
24X-3, 48–48	214.68	3	1.2150	0.00515	0.00980
24X-4, 59–59	216.29	5	1.2266	0.00609	0.03535
24X-5, 40–40	217.60	150	1.1762	0.00575	-0.00371
25X-2, 45–45	222.85	32	0.9955	0.00505	-0.02900

Table 11 (continued).

Core, section, interval (cm)	Depth (mbsf)	Probe number	Thermal conductivity (W/m·K)	Standard error (W/m·K)	Calculated drift (W/m·K)
25X-3, 37–37	224.27	3	1.1376	0.00646	-0.00070
25X-4, 87–87	226.27	5	1.0891	0.00477	0.02036
25X-5, 118–118	228.08	150	1.1857	0.00431	0.00292
26X-2, 30–30	232.30	32	1.1274	0.00626	-0.00728
26X-2, 110–110	233.10	3	1.1916	0.00616	-0.00002
26X-3, 32–32	233.82	5	1.1835	0.00442	0.03335
26X-3, 110–110	234.60	150	1.1829	0.00608	0.00124
27X-3, 48–48	243.22	32	1.1110	0.00409	-0.02802
27X-4, 90–90	245.14	3	1.0650	0.00699	-0.01783
27X-5, 87–87	246.61	5	1.2443	0.00527	0.03701
27X-6, 70–70	247.94	150	1.0018	0.00628	-0.03799
28X-1, 56–56	250.36	32	0.9255	0.00523	-0.04412
28X-2, 55–55	251.85	3	1.0836	0.00664	-0.00085
28X-3, 66–66	253.46	5	0.9877	0.00611	0.02295
28X-4, 77–77	255.07	150	1.0997	0.00619	-0.00324
29X-2, 77–77	260.61	32	1.0550	0.00444	-0.03081
29X-3, 76–76	262.10	3	1.0654	0.00820	-0.02497
29X-4, 56–56	263.40	5	1.1584	0.00477	0.03090
29X-5, 73–73	265.07	150	1.0556	0.00501	-0.00726
30X-2, 48–48	271.08	32	1.1160	0.00315	-0.01657
30X-3, 62–62	272.72	3	1.1983	0.00455	0.00220
30X-4, 92–92	274.52	5	1.0414	0.00521	0.00253
30X-5, 56–56	275.66	150	1.1153	0.00554	0.00226
31X-2, 57–57	279.93	32	1.0872	0.00548	-0.01538
31X-3, 75–75	281.61	3	0.9514	0.00497	-0.02622
31X-4, 55–55	282.91	5	1.2808	0.00507	0.04454
31X-5, 69–69	284.55	150	1.1556	0.00496	0.00212
32X-2, 63–63	290.53	32	1.0938	0.00412	-0.00162
32X-3, 63–63	292.03	3	1.1164	0.01421	-0.01224
32X-4, 63–63	293.53	5	1.1270	0.00539	0.03232
32X-5, 61–61	295.01	150	1.1354	0.00517	0.00201
33X-2, 70–70	300.30	32	1.1382	0.00539	-0.03233
33X-3, 70–70	301.80	3	1.2039	0.00645	-0.01701
33X-5, 89–89	304.99	5	1.2432	0.00522	0.03700
33X-6, 87–87	306.47	150	1.2213	0.00565	0.01430
34X-1, 60–60	308.40	5	1.1842	0.00632	0.07905
34X-2, 60–60	309.90	32	1.1799	0.00552	0.01690
34X-3, 60–60	311.40	3	1.1989	0.00452	0.01054
35X-1, 70–70	318.20	32	1.0330	0.00370	-0.03057
35X-2, 70–70	319.70	3	1.1736	0.00356	-0.00413
35X-3, 70–70	321.20	5	1.2134	0.00568	0.05461
35X-5, 70–70	324.20	150	1.1300	0.00329	-0.01711
36X-1, 70–70	327.70	32	1.1667	0.00586	-0.00398
36X-2, 70–70	329.20	3	1.2335	0.00590	0.01143
36X-3, 70–70	330.70	5	1.2431	0.00385	0.03636
36X-4, 70–70	332.20	150	1.2361	0.00556	0.00166
37X-2, 50–50	337.96	32	1.1171	0.00576	-0.03533
37X-3, 50–50	339.46	3	1.1682	0.00525	-0.00618
37X-5, 50–50	342.46	5	1.1888	0.00616	0.02017
37X-6, 50–50	343.96	150	1.0593	0.00428	-0.01026
38X-2, 43–43	348.23	32	1.1379	0.00348	-0.01626
38X-3, 43–43	349.73	3	1.1620	0.00766	-0.01012
38X-5, 43–43	352.73	5	1.1845	0.00544	0.02352
38X-6, 43–43	354.23	150	1.1650	0.00577	-0.00334
39X-2, 40–40	357.80	32	1.1312	0.00568	-0.00376
39X-3, 40–40	359.30	3	1.2226	0.00604	0.02185
39X-4, 40–40	360.80	5	1.2363	0.00670	0.03756
39X-5, 40–40	362.30	150	1.0587	0.00522	-0.00595
40X-2, 40–40	367.40	32	1.0774	0.00433	-0.01063
40X-3, 40–40	368.90	3	1.2160	0.00714	0.02397
40X-5, 40–40	371.90	5	1.1948	0.00361	0.02683
40X-6, 40–40	373.40	150	1.1694	0.00598	0.00643
41X-2, 41–41	376.33	32	1.0806	0.00755	-0.02035
41X-3, 49–49	377.91	3	1.1522	0.00579	-0.00041
41X-4, 51–51	379.43	5	1.1548	0.00361	0.02788
41X-5, 63–63	381.05	150	1.2104	0.00505	0.01614
42X-1, 67–67	385.47	32	1.2817	0.00316	0.02464
42X-6, 42–42	392.72	3	1.2664	0.00632	0.02407
43X-3, 82–82	398.32	5	1.3166	0.00763	0.04919
44X-1, 90–90	400.90	32	1.2021	0.00524	-0.00360
44X-2, 79–79	402.29	3	1.2908	0.00762	0.01819
44X-3, 65–65	403.65	5	1.2570	0.00457	0.02736
44X-4, 56–56	405.06	150	1.1555	0.00567	-0.01861

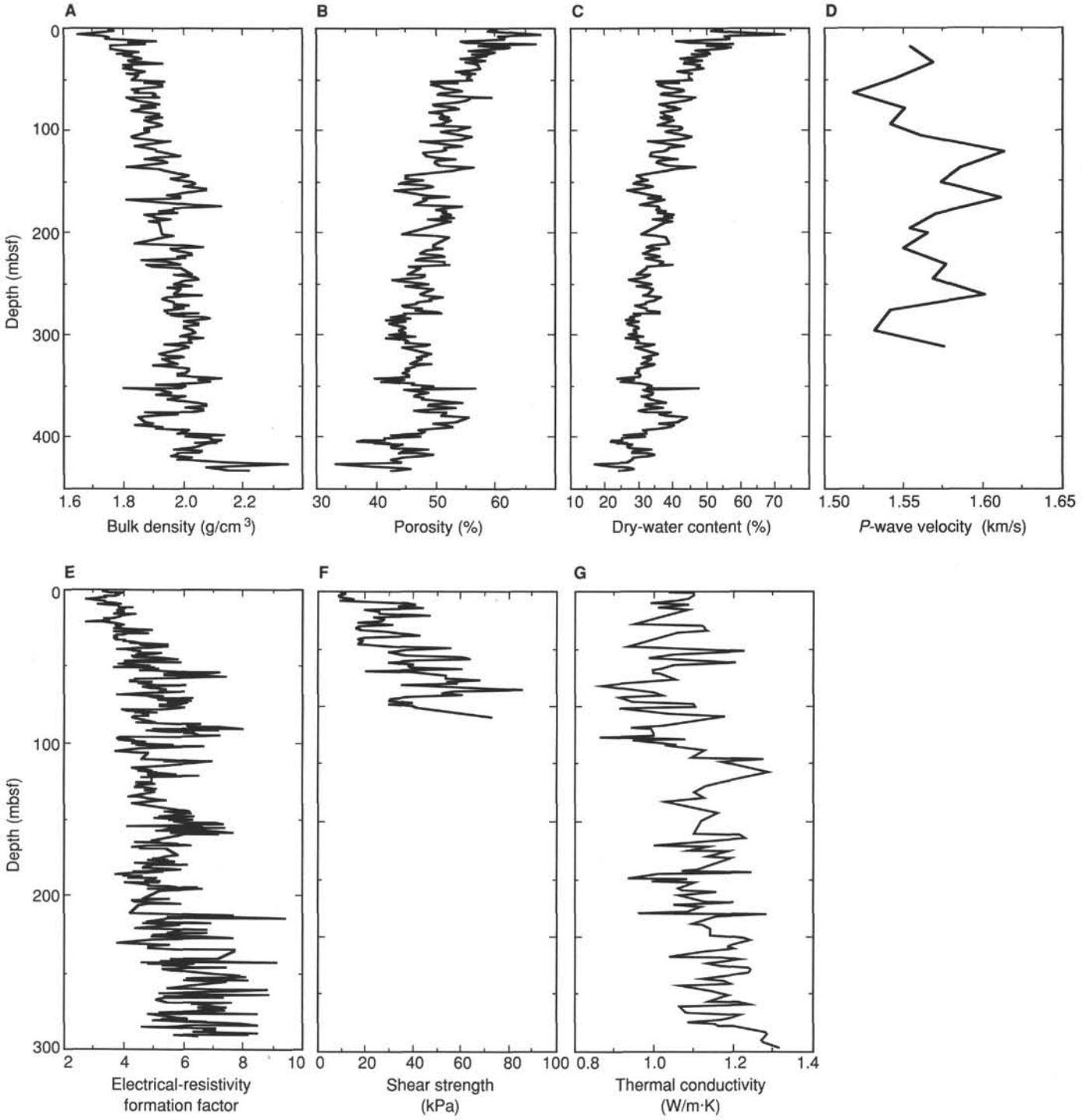

Figure 37. Physical properties vs. depth, Site 822. **A.** Bulk density vs. depth at Site 822. Data were obtained from mass and volume measurements for samples taken from split cores. **B.** Porosity vs. depth at Site 822. Data were obtained from mass and volume measurements for samples taken from split cores. **C.** Dry-water content vs. depth at Site 822. Data were obtained from samples taken from split cores. **D.** *P*-wave velocity at Site 822. Data were obtained from samples taken from split cores using the Hamilton frame. **E.** Electrical-resistivity formation factor values from Site 822. Data were obtained from split cores using the Werner electrode probe. **F.** Shear strength values at Site 822. Data were obtained from split cores using the Wykeham-Farrance motorized vane apparatus. **G.** Thermal conductivity at Site 822. Data were obtained from split cores using the needle probe apparatus.

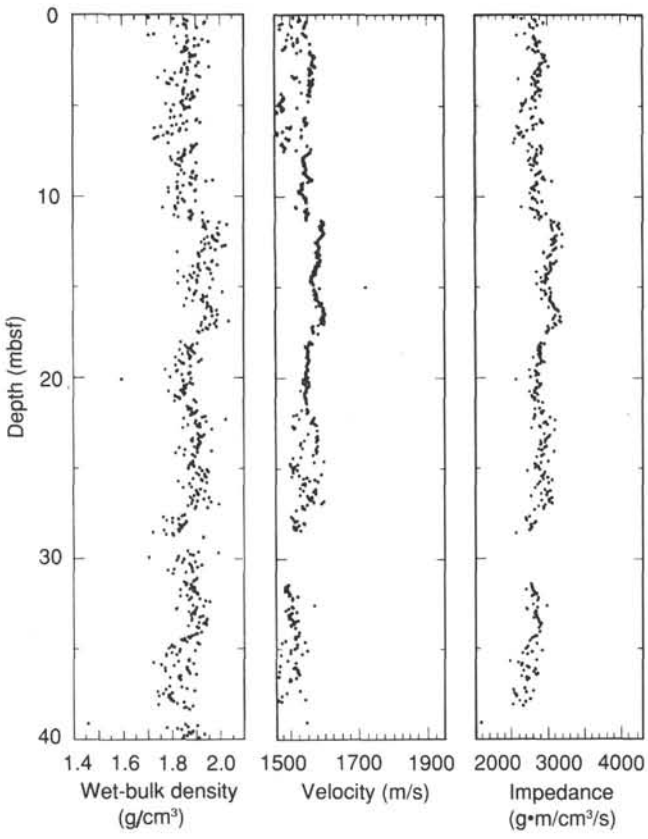

Figure 38. Velocity vs. depth for the upper 150 mbsf of section at Site 822 determined from Hamilton Frame measurements for samples from split cores and from wireline logging.

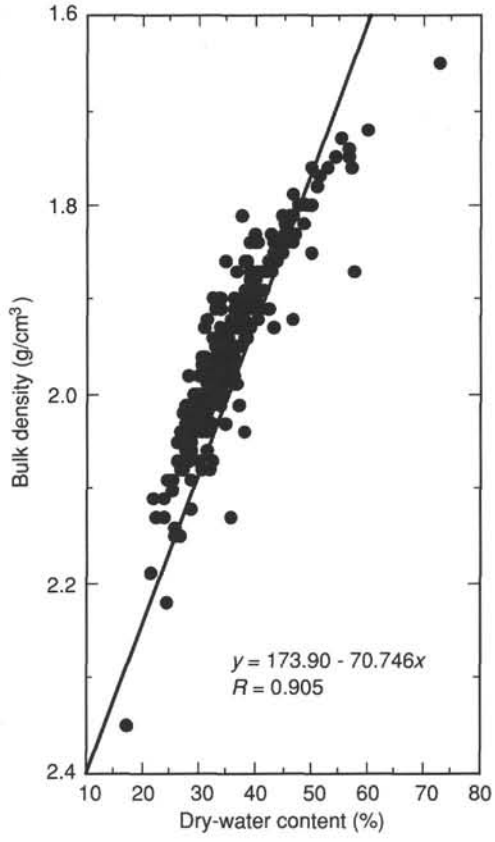

Figure 39. Dry-water content vs. depth at Site 822. Data were obtained from mass and volume measurements of samples taken from split cores.

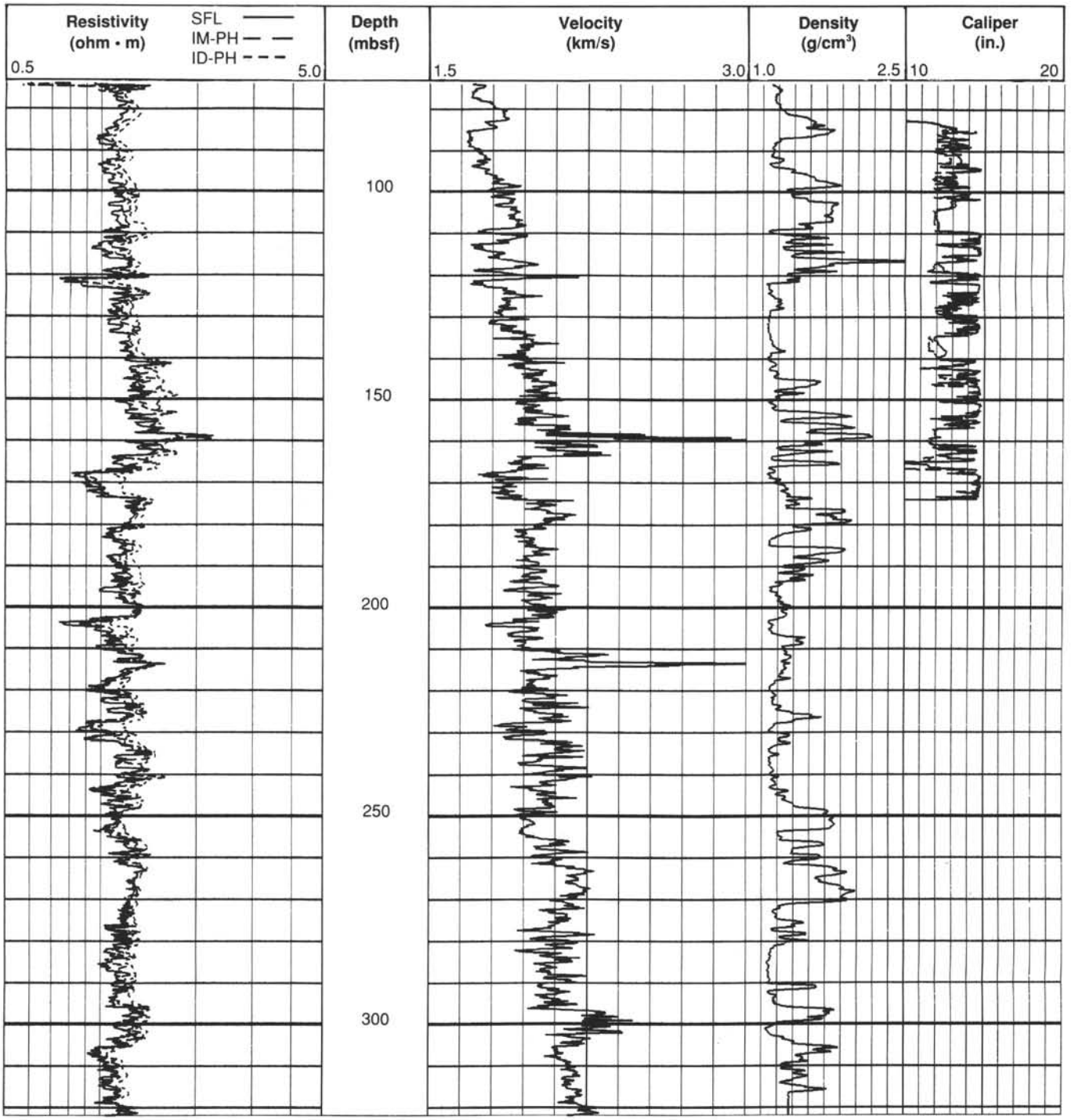

Figure 40. Primary porosity logs obtained by the seismic stratigraphic tool string at Hole 822A.

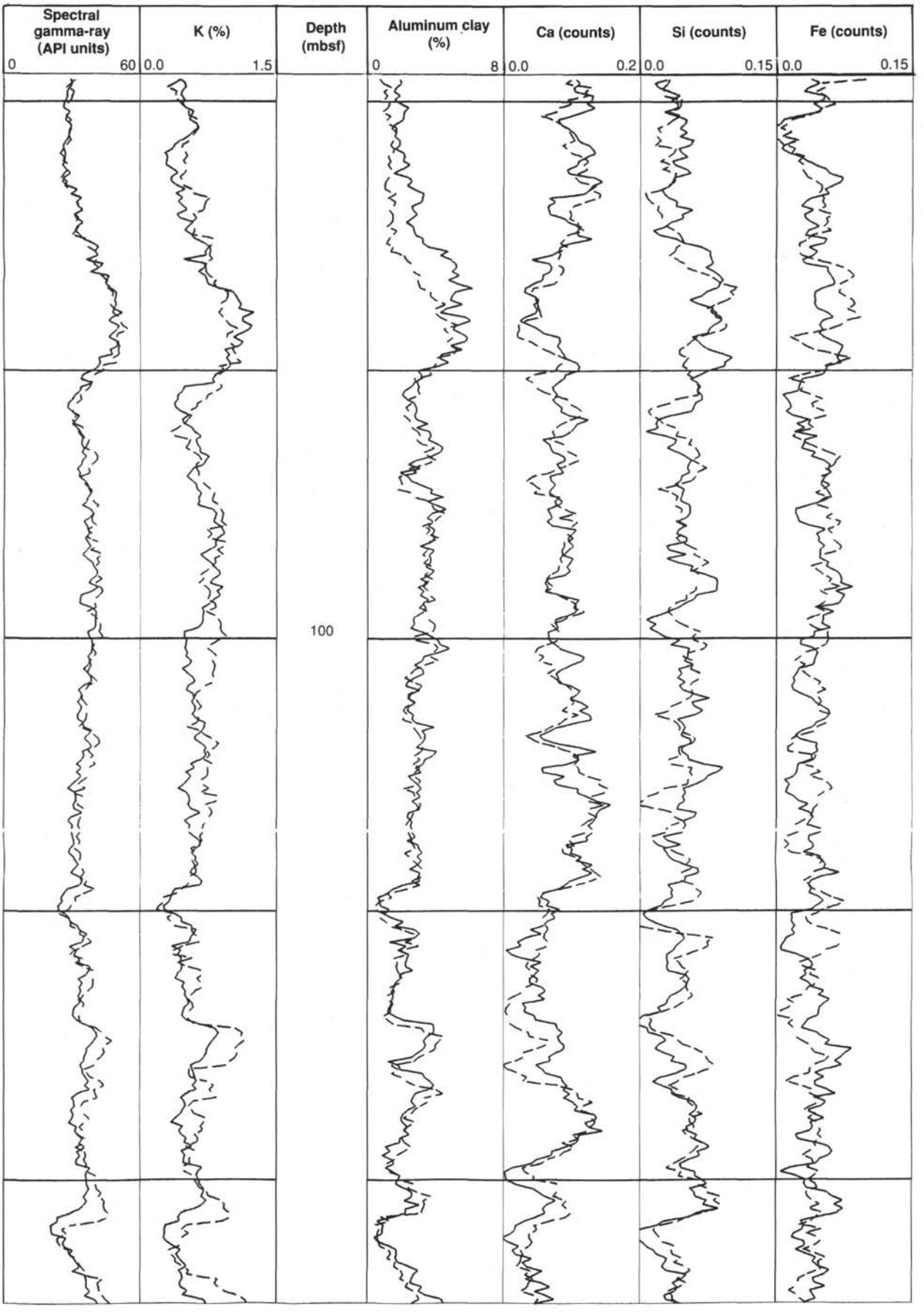

Figure 41. Geochemical logs for the interval from 79.2 to 124.6 mbsf at Site 822 showing the replicability of two logging passes over this interval.

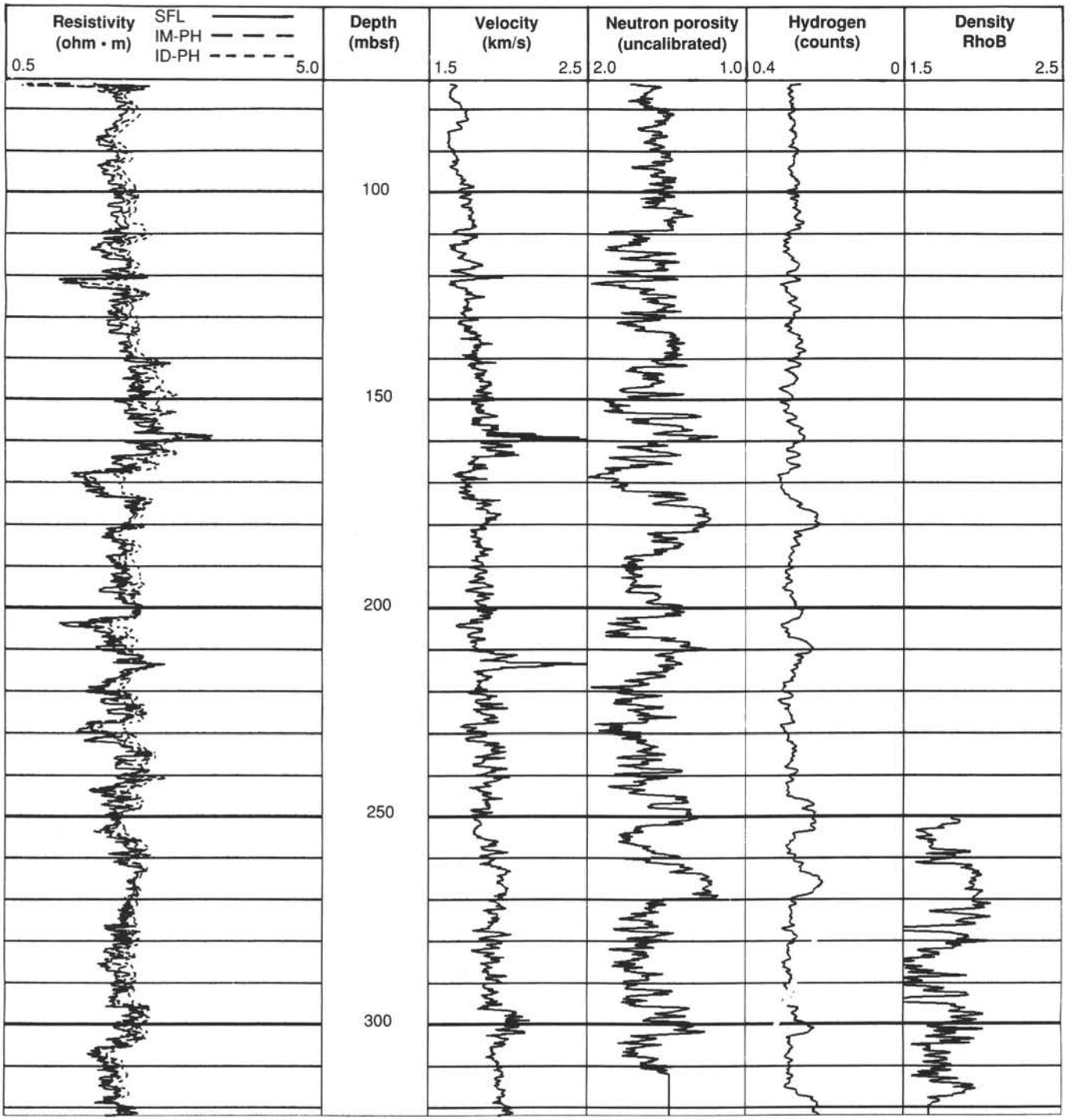

Figure 42. Comparison of porosity-sensitive logs for Site 822 to evaluate their quality. Note the strong character match between resistivity and velocity logs, both of which are good indicators of variations in porosity and are relatively insensitive to variations in hole size. In contrast, the neutron, hydrogen, and bulk density logs easily confuse porosity with borehole fluid in washed-out intervals of the hole.

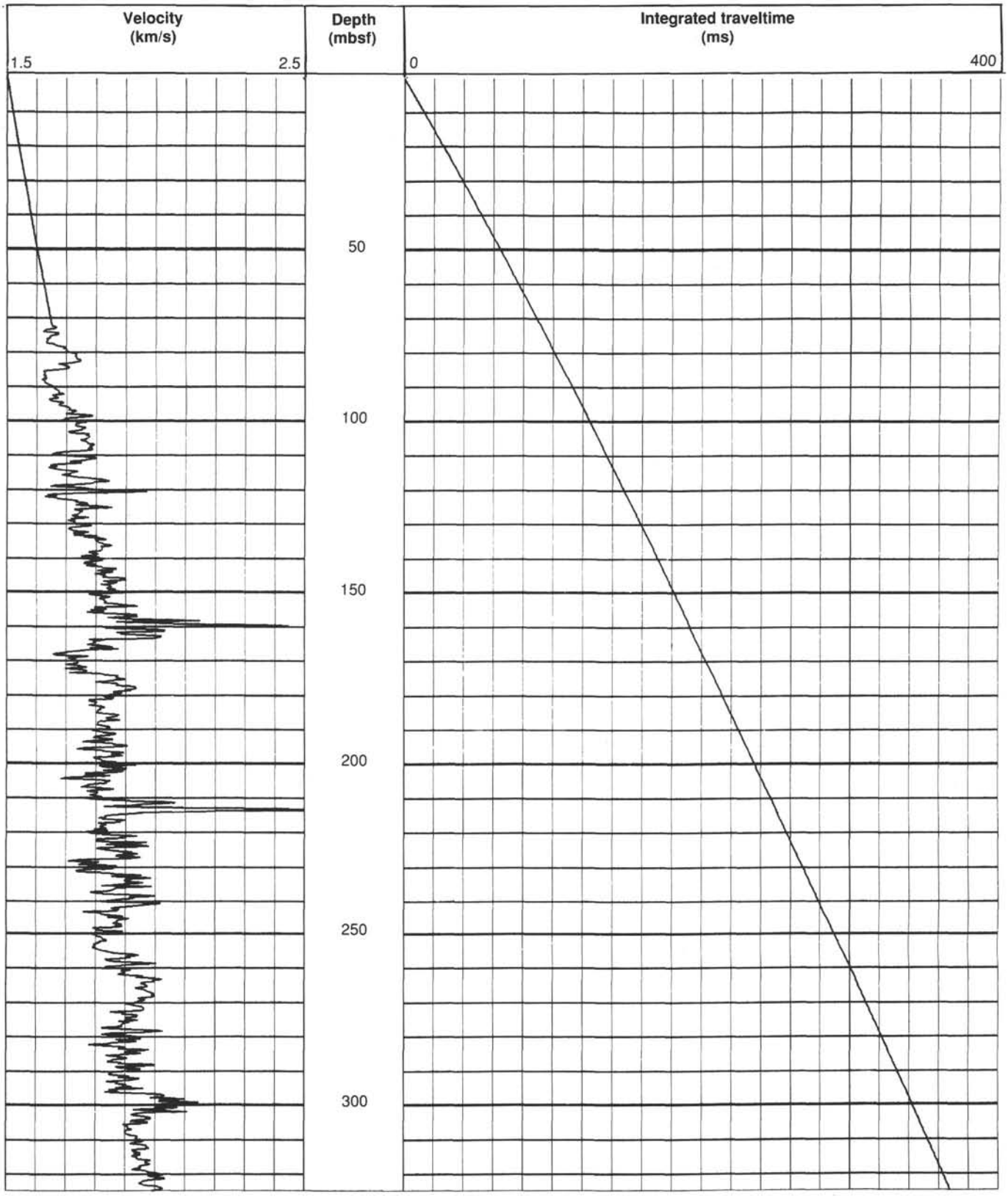

Figure 43. Velocity log (and integrated TWT function that it implies) for matching core-based information from Site 822 with seismic sections across the site.

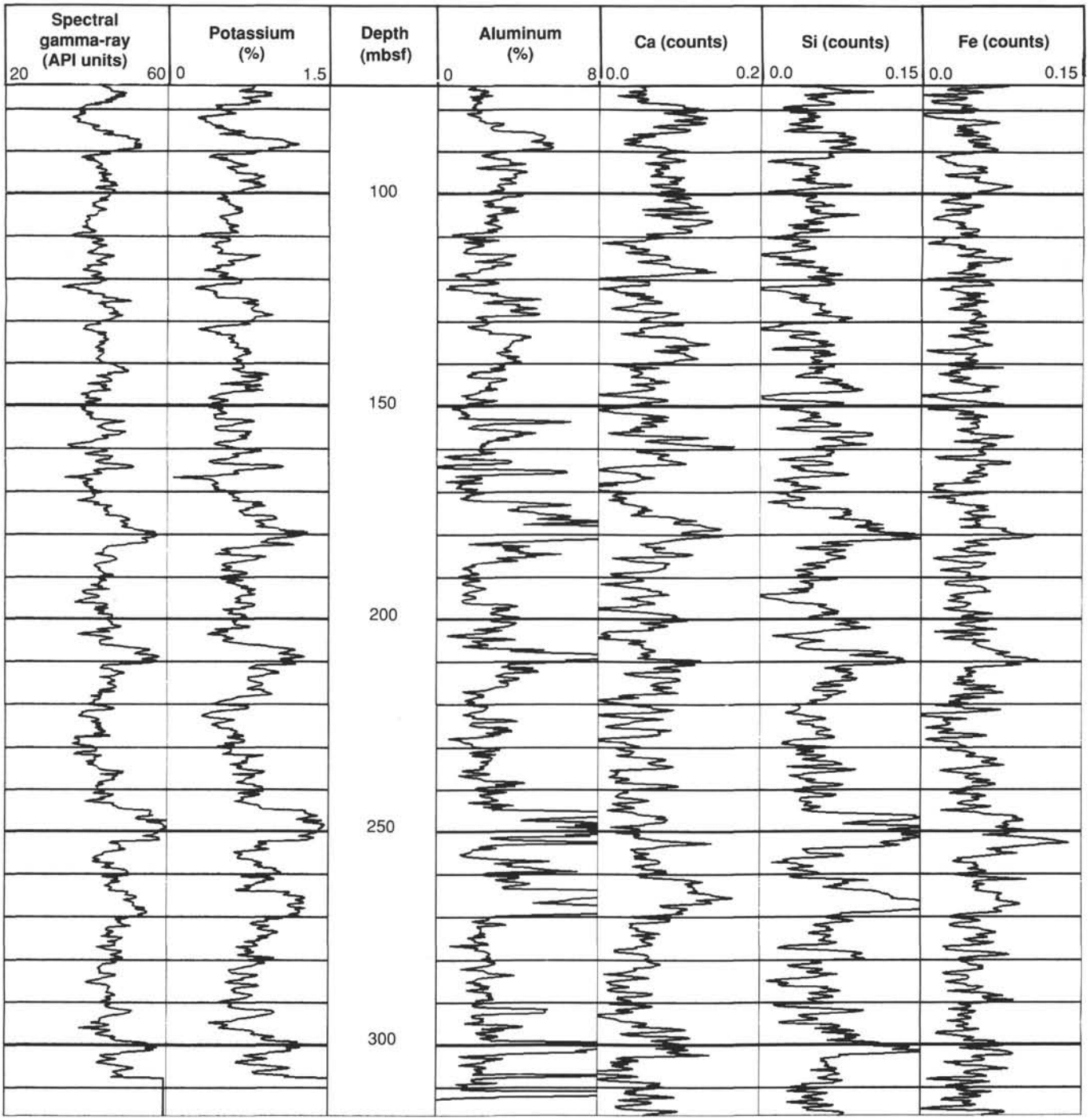

Figure 44. Geochemical logs from the portion of Site 822 for which open-hole logs were obtained.

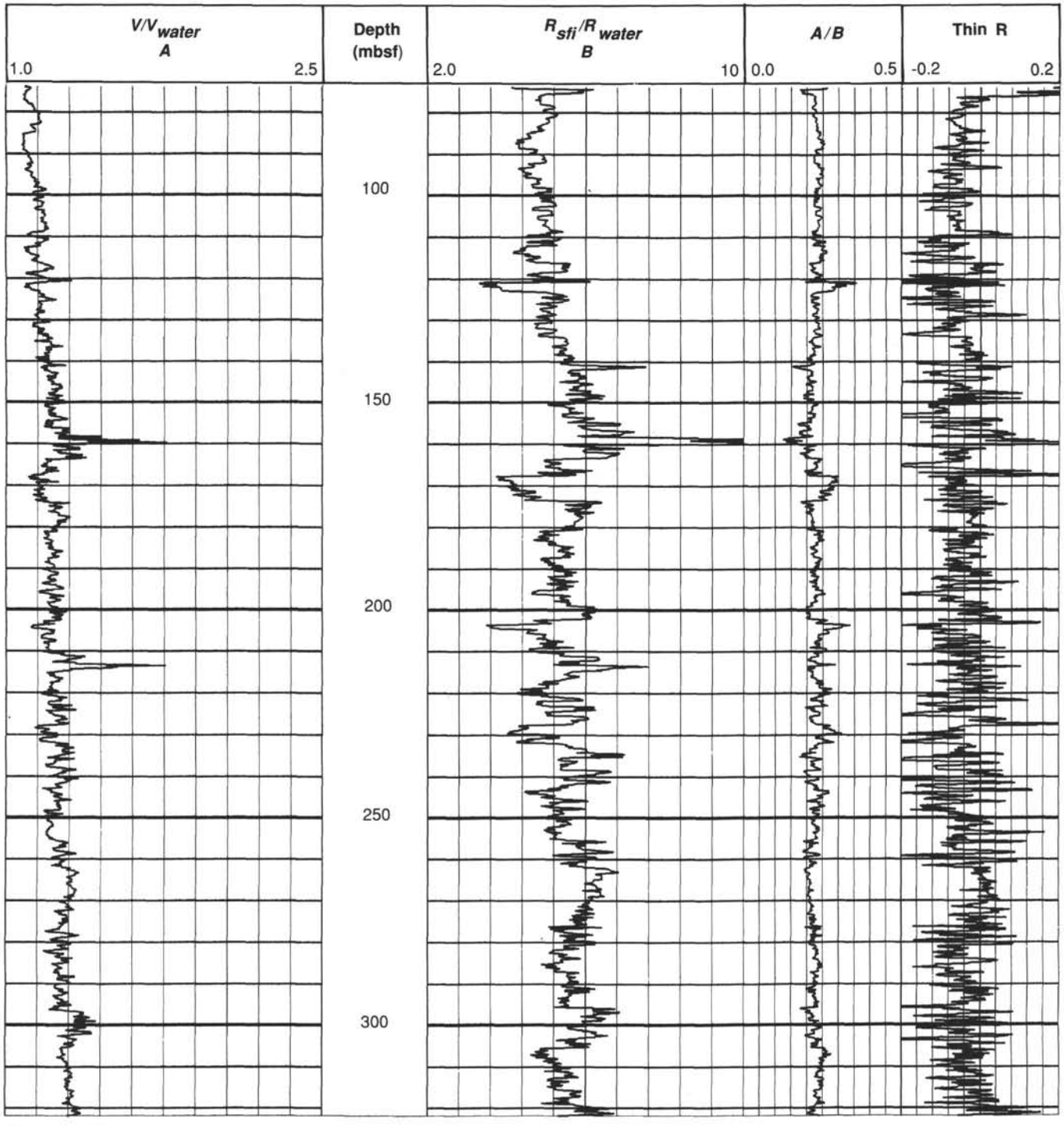

Figure 45. Velocity and resistivity logs for Site 822, plotted as ratios to each other and to water to highlight changes in pore geometry.

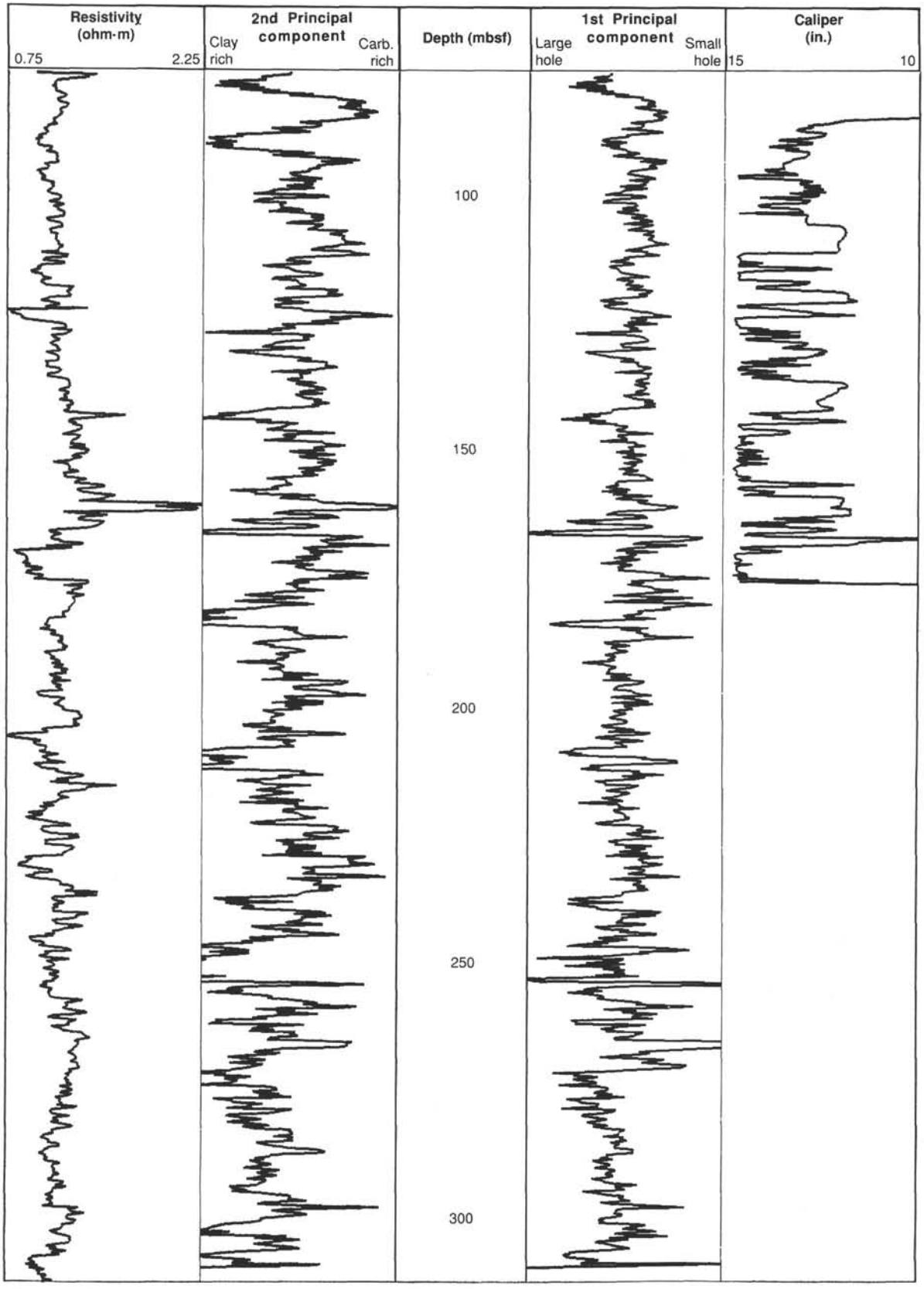

Figure 46. First two principal components of the neutron, hydrogen, silicon, calcium aluminum, gamma-ray, and potassium logs. Values of the eigenvector suggest that the first principal component is that of the effect of hole size and that the second principal component is sensitive to relative proportions of clay minerals and carbonate.

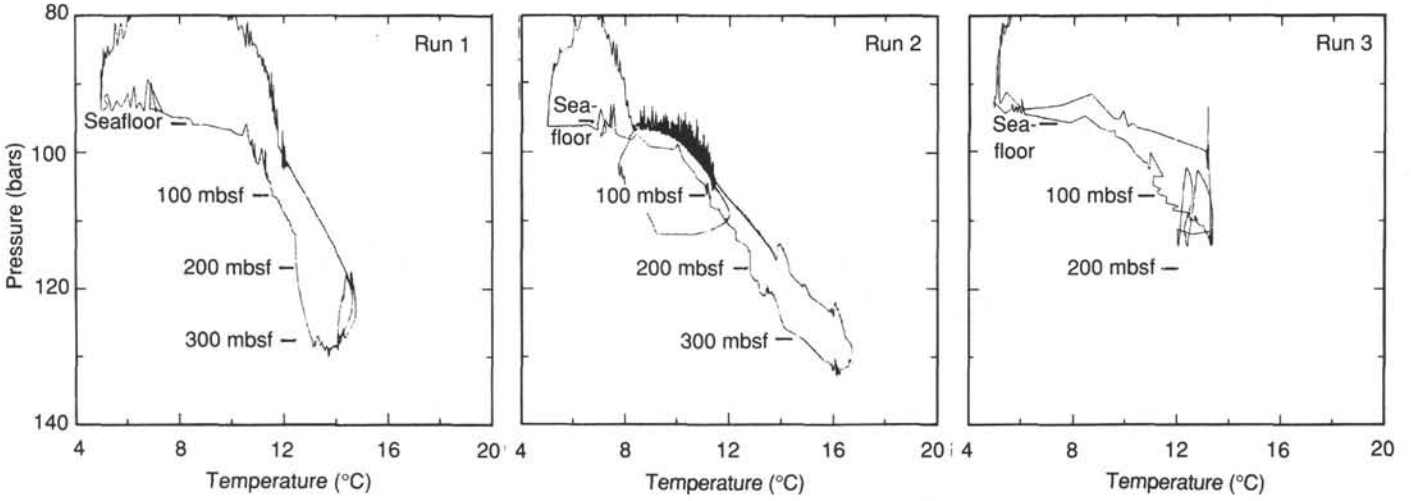

Figure 47. Temperature log as a function of pressure (or depth) for Site 822.

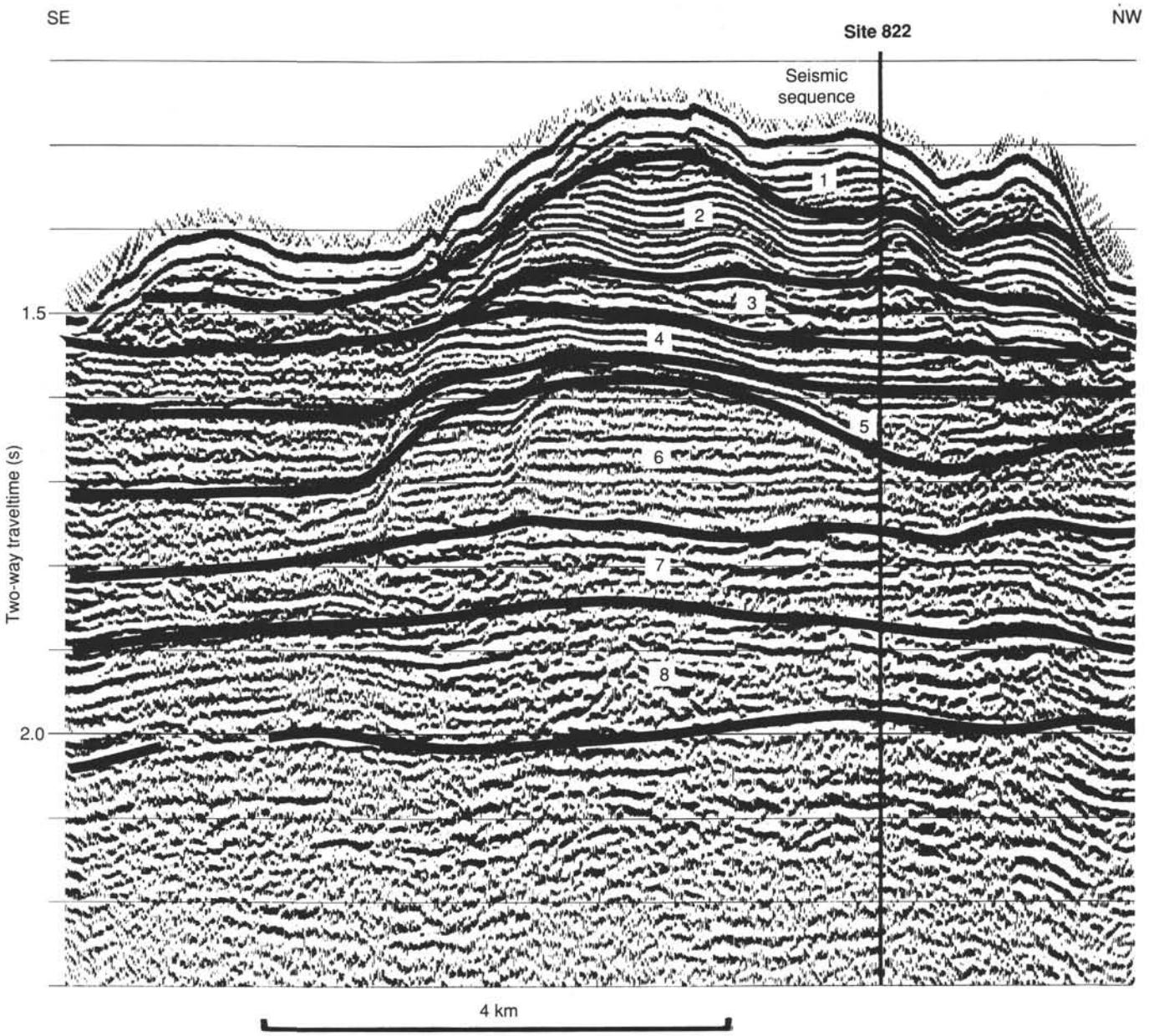

Figure 48. Portion of BMR multifold water-gun seismic profile (Line 7545, Part A) across Site 822, indicating characteristics of preliminary seismic sequences 1 through 8, as identified within site area. Profile location is shown in Figure 3.

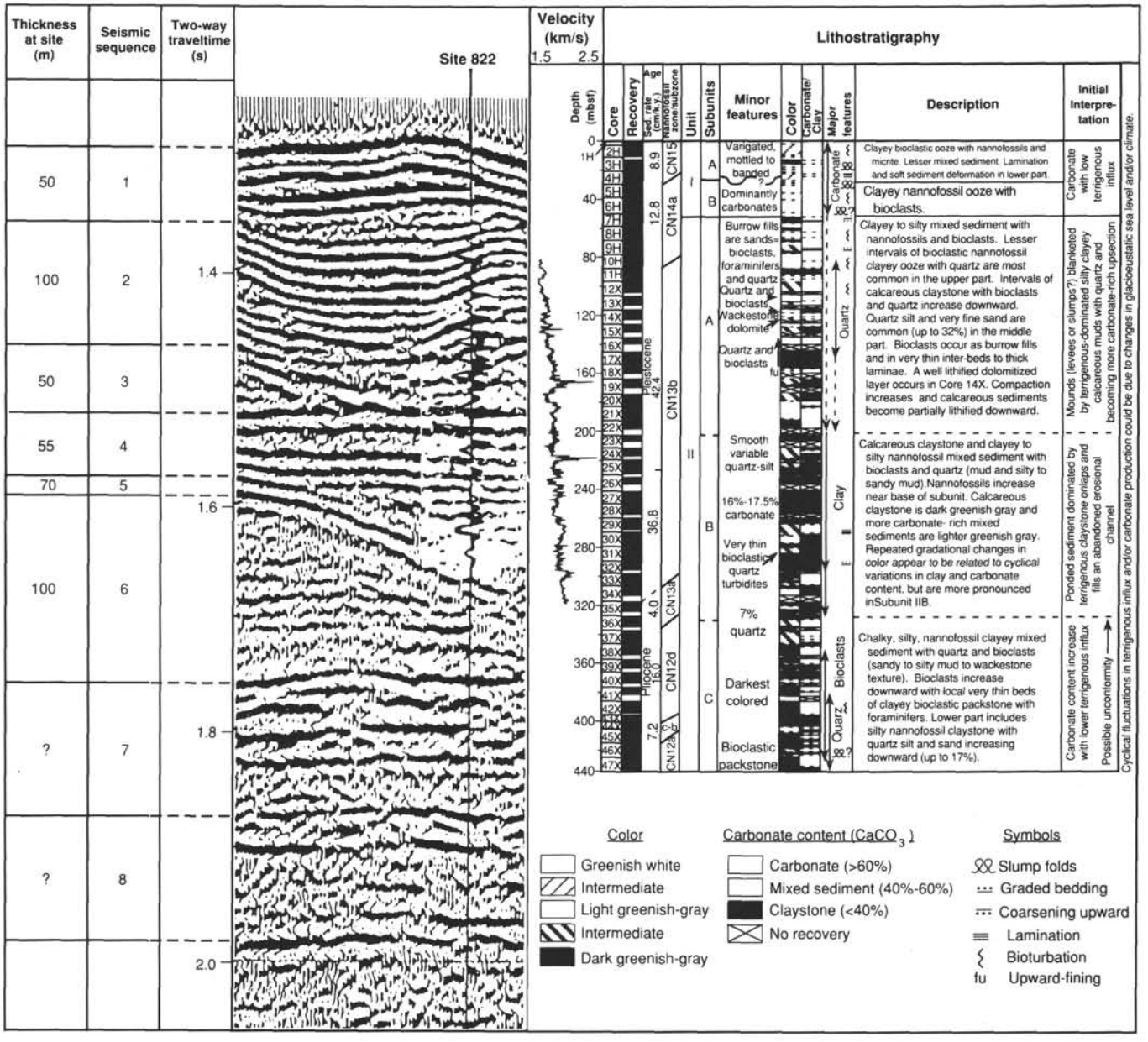

Figure 49. Preliminary correlation of seismic sequences at Site 822 with drilling results. Shows synthetic seismogram and velocity log derived from downhole logging and simplified lithostratigraphy of site.

Hole 822A: Resistivity-Sonic-Natural Gamma Ray Log Summary

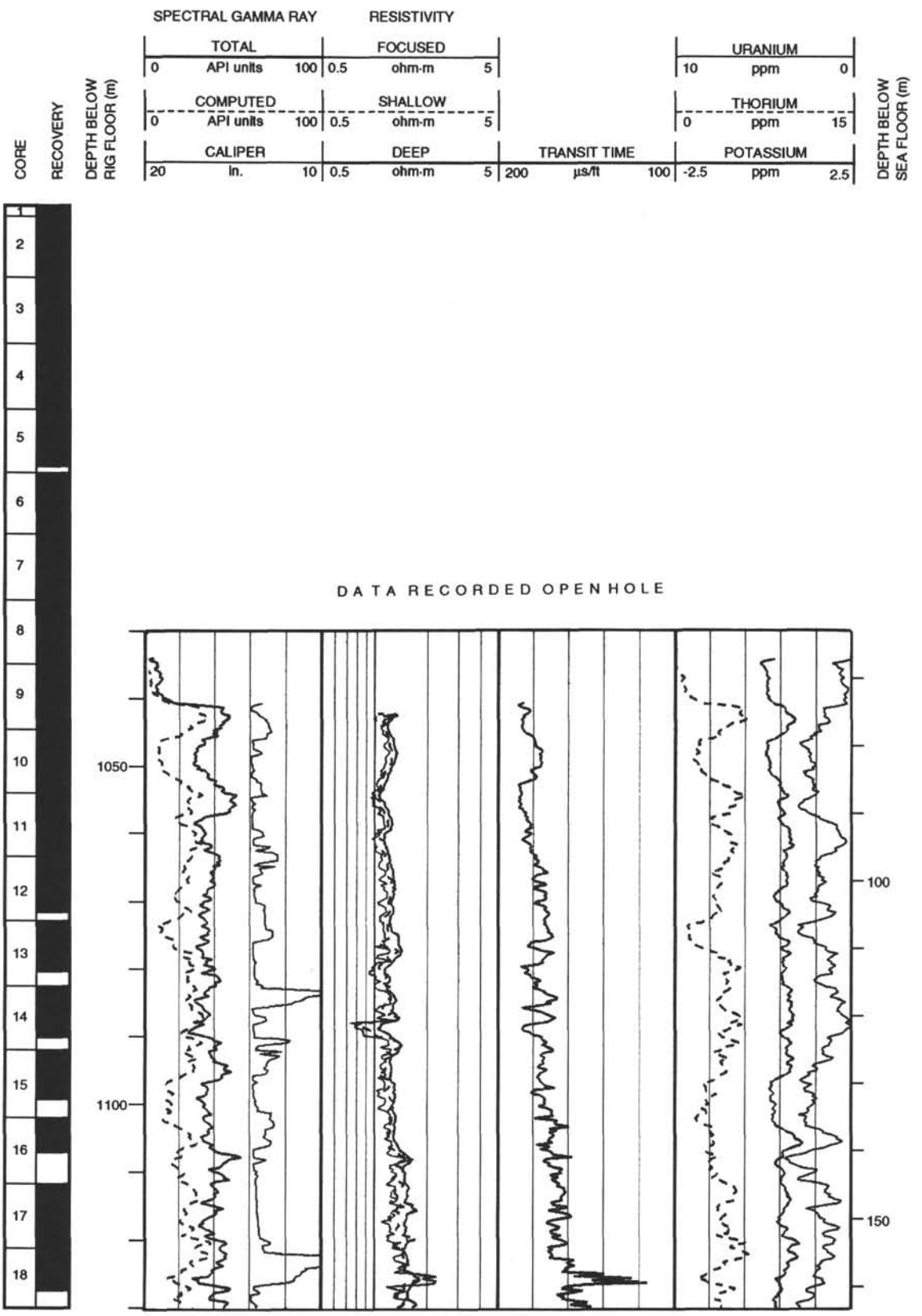

Hole 822A: Resistivity-Sonic-Natural Gamma Ray Log Summary (continued)

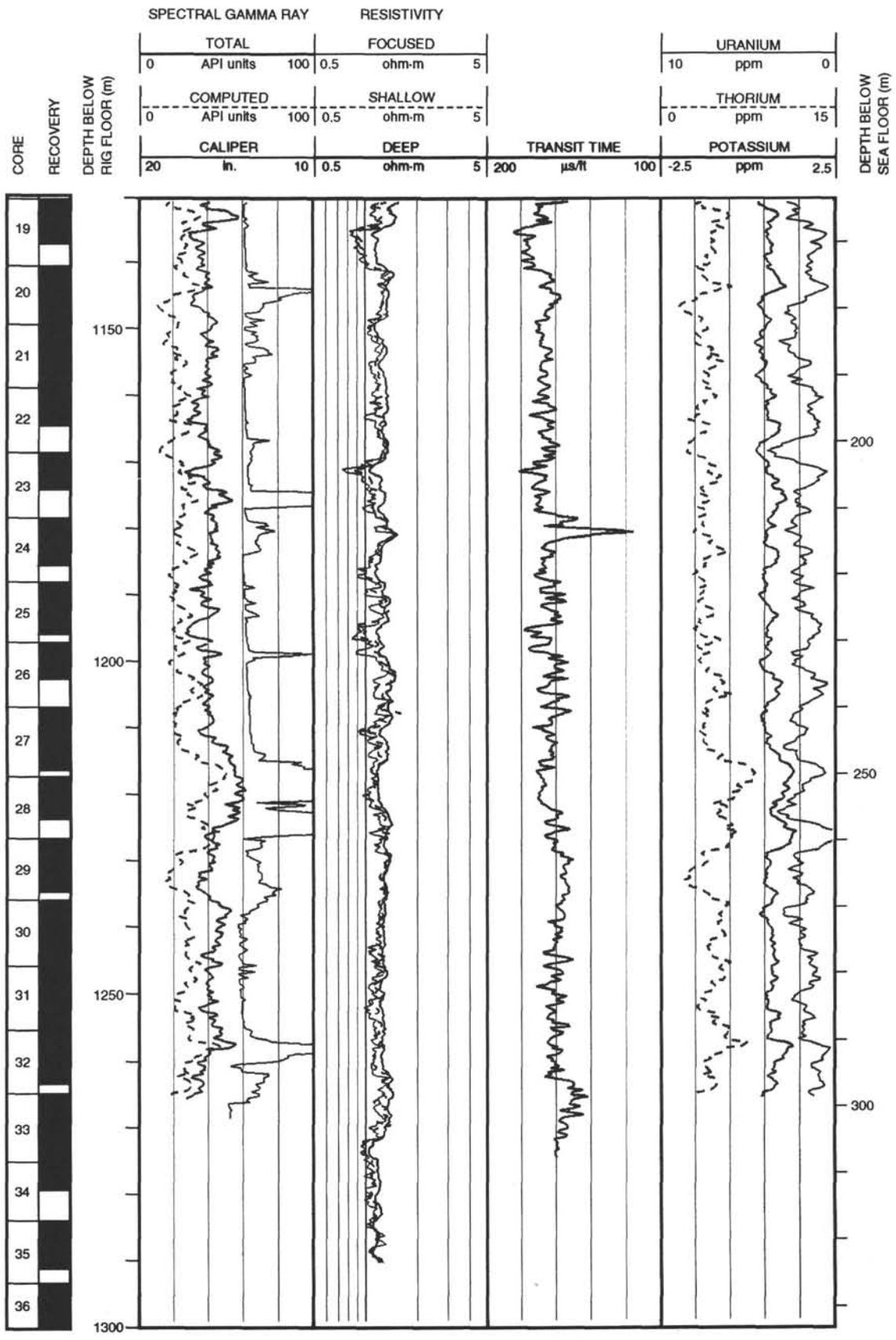

Hole 822A: Density-Natural Gamma Ray Log Summary

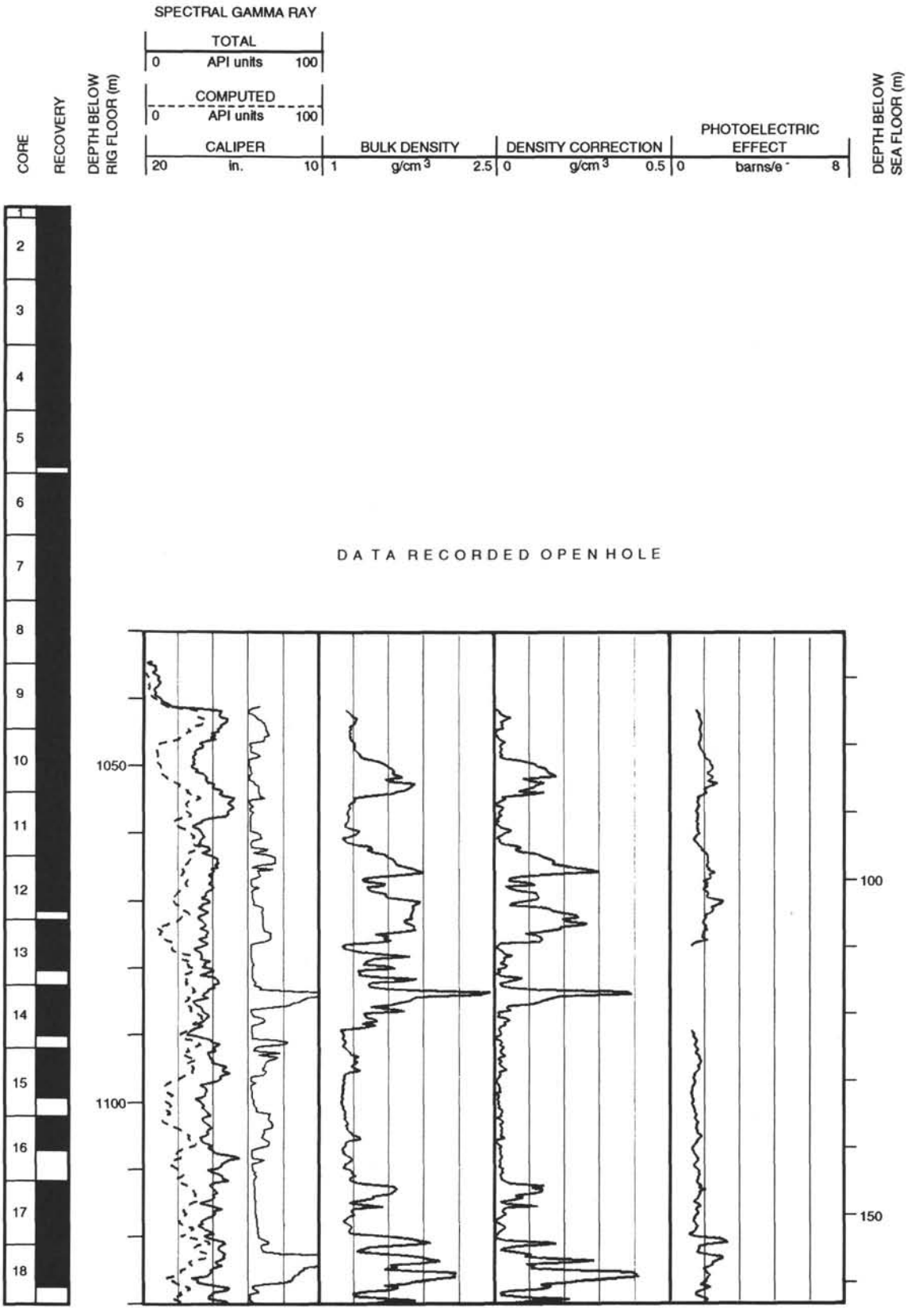

Hole 822A: Density-Natural Gamma Ray Log Summary (continued)

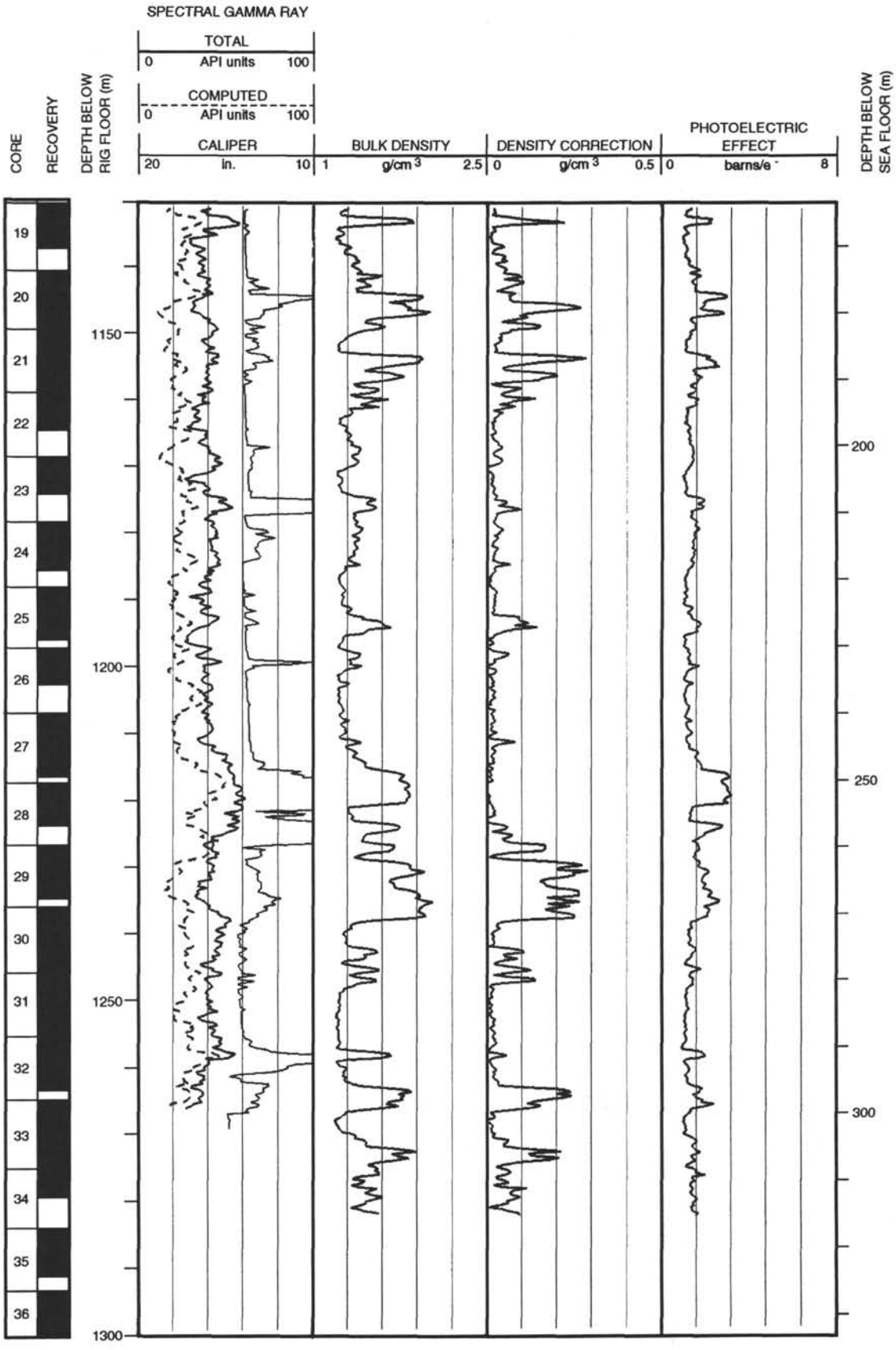

Hole 822A: Geochemical Log Summary

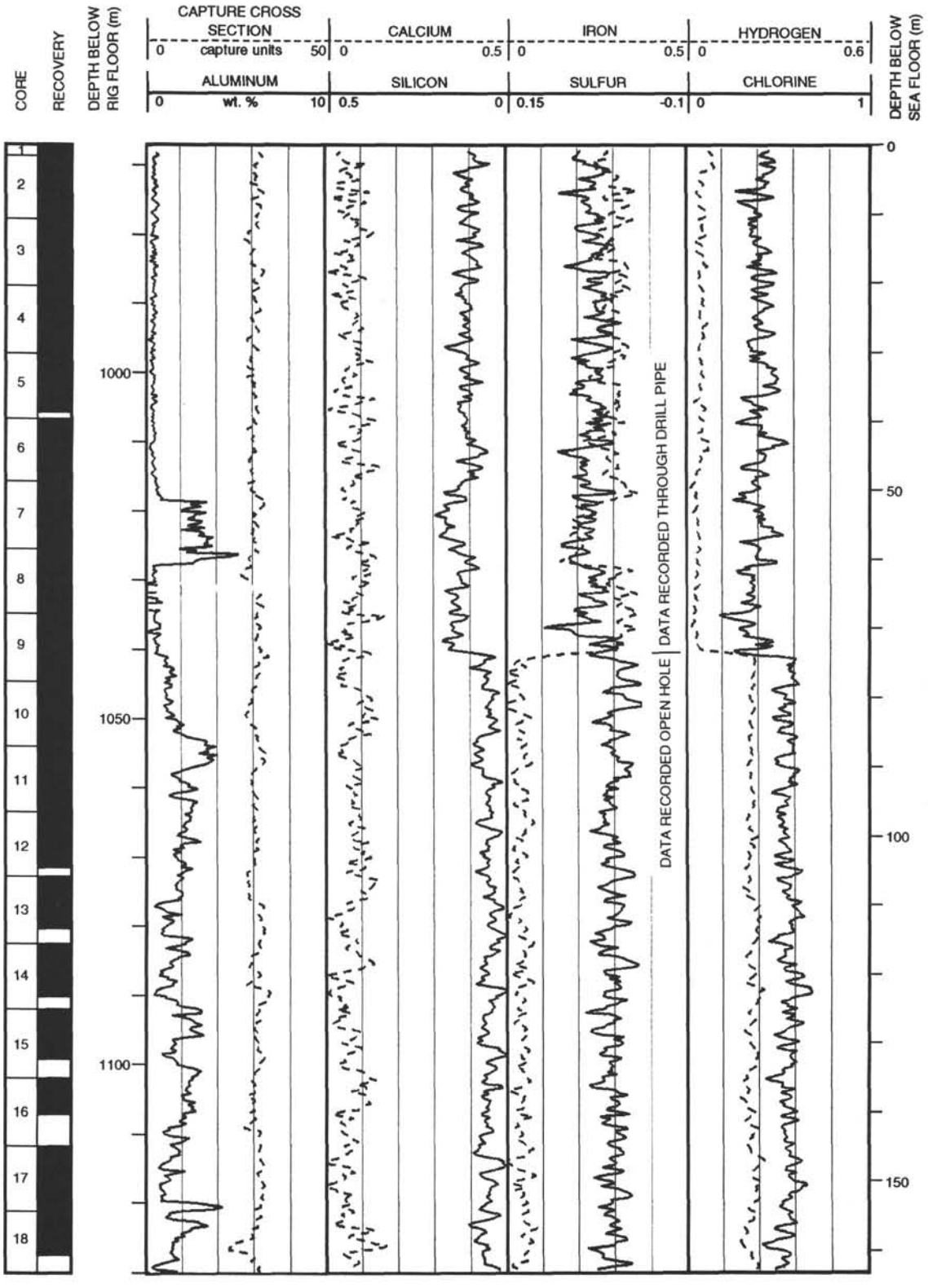

Hole 822A: Geochemical Log Summary (continued)